TÉCNICO LISBOA

Thermal and structural optimization of a small satellite using composite materials

Mariana Coelho dos Santos Moreira

Thesis to obtain the Master of Science Degree in

Aerospace Engineering

Supervisor(s): Prof. Filipa Andreia de Matos Moleiro
Dr. Miguel Sousa Machado

Examination Committee

Chairperson: Prof. José Fernando Alves da Silva
Supervisor: Prof. Filipa Andreia de Matos Moleiro
Member of the Committee: Dr. Frederico José Prata Rente Reis Afonso

December 2019

To my mother.

To Felismina.

And to my grandfather, Alberto.

Acknowledgments

First of all, I would like to thank my supervisor, Prof. Filipa Moleiro, for the continuous help and advises throughout the development of this work.

I would like to thank my supervisor at CEiiA, Eng. Miguel Machado, for the constant availability and readiness to help me with anything required for the development of this work. To CEiiA for the enriching opportunity and to CEiiA's team, specially Eng. Paulo Figueiredo, Eng. Inês Martins and Eng. André Guerra, for all the dedicated time and advises given during this path.

To Daniel, José, André and Sofia, that like me, adventured in this journey of making the master thesis in CEiiA. Thank you for the support and companionship.

To all my friends for making this journey a fun ride. Specially to my old time friends, Jerry and Antero, that accompanied me almost since kindergarden to university, for always being there and making this journey a one of a kind.

To the two amazing persons that Técnico allowed into my life, Augusto and Catarina, I am sure these years would not have been the same without you. You truly are extraordinary friends.

I could not forget, Maria Rubina, for the endless chats and for the vivacious person you are. Thank you for being so interested in any and all things of life.

To Pedro Luís, thank you for always helping me out whenever I needed. You are a dear friend and your wisdom, although you may denied it, always surprises me.

To my Love, Ricardo Jorge, for the endless support and motivation. I cannot express the gratitude and how lucky I am for having you in my life. You that support all my anxiety and self-doubt over and over again, always with a soothing and motivating word. Thank you for being the amazing person you are and for allowing me to be in this journey with you.

Lastly, I would like to conclude by thanking to all my family, my father and brothers, João Joaquim e Tomás Duarte, for always being there when I needed and for giving me this comfort felling called home. Most specially, to my mother, that despite the hard life challenges, teached me what strength really means.

Resumo

O desenvolvimento de CubeSats equipados com novos materiais estruturais mais leve e capazes de fornecer o desempenho estrutural e térmico requerido, durante a vida útil do satélite, viria possibilitar o aumento de carga útil.

Esta tese descreve a análise de materiais compósitos laminados viáveis para serem usados como alternativa ao alumínio tradicional nos painéis laterais da estrutura de um CubeSat 3U do CEiiA.

Dezoito laminados são criados com diferentes esquemas de empilhamento, feitos de polímero reforçado com fibra de carbono (CFRP) ou fibra de vidro (GFRP) combinados com lâminas de alumínio, grafite pirolítica ou malha de cobre. Uma matriz de decisão é criada onde os compósitos mais leves, com boas propriedades mecânicas e alta condutividade térmica são preferíveis. São selecionados três laminados, formados por CFRP com um núcleo de alumínio, CFRP com núcleo de grafite pirolítica e GFRP com núcleo de grafite pirolítica.

Para avaliar o comportamento estrutural e térmico do satélite com os painéis laterais de laminado, análises FEM estruturais estáticas, modais e térmicas foram executadas. Se o comportamento do satélite não igualar o comportamento do mesmo com os painéis de alumínio, procede-se a um ciclo de otimização.

A investigação demonstrou que os laminados híbridos conseguem providenciar o desempenho estrutural e térmico requerido com uma massa menor do que a de alumínio. Uma redução de massa de 58.1% é atingida para cada painel com o compósito laminado final otimizado, formado por uma lâmina de CFRP com um núcleo de grafite pirolítica de 0.4 mm e uma espessura total de 1.6 mm.

Palavras-chave: CubeSats, materiais compósitos laminados, laminados híbridos, análise estrutural de elementos finitos, análise térmica de elementos finitos, ambiente espacial.

Abstract

The development of CubeSats equipped with new structural materials suggests a new alternative to the use of the conventional aluminium. A lighter structure capable of providing the structural and thermal performance required during the satellite's lifetime, would enable the increase of mass budget used in other subsystems.

This thesis describes the assessment of viable laminated composite materials as an alternative to the typical aluminium used in the side panels structure of a CEiiA's 3U CubeSat.

Eighteen laminates are designed with distinct stacking sequences made of Carbon Fibre Reinforced Polymer (CFRP) or Glass Fibre Reinforced Polymer (GFRP) combined with laminae of aluminium, pyrolytic graphite or copper mesh. A decision matrix is devised in which composites with lightweight, good mechanical properties and high thermal conductivity are preferred. Three laminates are selected, which are formed by CFRP with an aluminium core, CFRP with pyrolytic core and GFRP with pyrolytic core.

To evaluate the structural and thermal behaviour of the satellite with the laminate side panels, linear static, normal modes and static thermal FEM analyses are performed. If the satellite behaviour is not similar to the one with the aluminium panels, an optimization design cycle is performed.

The investigation revealed that hybrid laminates provide the structural and thermal performance required with a lower weight than the aluminium design. A 58.1% structural mass reduction for each panel is attained for the final optimized composite laminate, formed by laminae of CFRP with a pyrolytic graphite core of 0.4 mm thickness and total thickness of 1.6 mm.

Keywords: CubeSats, laminated composite materials, hybrid laminates, structural finite element analyses, thermal finite element analyses, space environment.

Contents

Acknowledgments v
Resumo vii
Abstract ix
List of Tables xiii
List of Figures xv
Nomenclature xvii
Glossary xxi

1 Introduction **1**
1.1 General Context 2
1.1.1 Satellite's Environments 3
1.1.2 Satellite's Subsystem 5
1.2 State of the Art 6
1.2.1 Composites for Aerospace Applications 6
1.3 CEiiA's CubeSat Design 8
1.3.1 Design Requirements 9
1.3.2 Structure Subsystem 9
1.3.3 Electronic Subsystem and Payload 9
1.4 Thesis' Contribution and Objectives 11
1.5 Thesis Outline 12

2 Composite Materials **15**
2.1 Theoretical Background 15
2.1.1 Generalized Hooke's Law 15
2.1.2 Laminated Composite Materials 18
2.2 Design Methodology 25
2.2.1 Preliminary Selection Approach 26

3 Structural Analysis **33**
3.1 Theoretical Background 33
3.1.1 Structural Requirements 34
3.1.2 Finite Element Method 36
3.1.3 Failure Theories 38

3.2 Finite Element Model . . . 40
3.2.1 Part Idealization . . . 40
3.2.2 Element Properties . . . 41
3.2.3 Boundary Conditions . . . 42
3.2.4 Mesh Refinement . . . 43
3.3 Structural Optimization Design Process . . . 46
3.3.1 Linear Static Analysis Results . . . 47
3.3.2 Normal Mode Analysis Results . . . 50

4 Thermal Analysis **55**
4.1 Theoretical Background . . . 55
4.1.1 Space Thermal Environment . . . 55
4.1.2 Thermal Requirements . . . 57
4.1.3 Static Thermal Analysis . . . 58
4.2 Finite Element Model . . . 58
4.2.1 Part Idealization . . . 58
4.2.2 Element Properties . . . 59
4.2.3 Boundary Conditions . . . 61
4.2.4 Mesh Refinement . . . 63
4.3 Thermal Optimization Design Process . . . 63

5 Thermo-Structural Analysis, Results and Discussion **73**
5.1 Thermo-Structural Optimization Final Design . . . 73

6 Conclusions and Future Work **79**
6.1 Conclusions . . . 79
6.2 Future Work . . . 80

Bibliography **81**

A 3U CubeSat Configuration **A.89**

B Materials' Properties **B.91**

C FEM Models Supplemental Information **C.93**

D Thermal Finite Element Analysis Results **D.95**

List of Tables

1.1 Electronic subsystems and payload general properties. . . . 11

2.1 Laminates' identification by numerical correspondence. . . . 28
2.2 Mechanical and thermal properties of the materials used for the side panels. . . . 29
2.3 Laminated composite materials' weighting factors. . . . 30
2.4 Decision matrix. . . . 31

3.1 Linear static case analyses. . . . 35
3.2 FOS for verification by analysis only regarding metallic and FRP satellite's structural parts. . . . 35
3.3 Static and modal FEM model mesh properties. . . . 42
3.4 Structural mass reduction for each side panel. . . . 47
3.5 Maximum displacement, strain, stress and MOS of the linear static cases analyses for aluminium side panels. . . . 48
3.6 Critical components MOS. . . . 48
3.7 Maximum failure index of the satellite's side panels. . . . 49
3.8 Minimum bolts' MOS of the linear static analysis. . . . 50
3.9 First natural frequencies of the normal mode analysis. . . . 50
3.10 First natural frequencies of the structural optimized laminates. . . . 51
3.11 Structural optimized laminates' mass reduction for each side panel. . . . 51

4.1 Thermal FEM model mesh properties. . . . 60
4.2 Materials' thermal properties. . . . 61
4.3 Hot and cold case orbit and flux characteristics. . . . 62
4.4 Component's internal heat dissipation. . . . 62
4.5 Laminates' equivalent thermal conductivity and respective side panel (ID1) thermal gradient for the hot and cold cases. . . . 69
4.6 Thermal optimized laminates' structural mass reduction for each side panel. . . . 70

5.1 Updated critical components' MOS. . . . 74
5.2 Updated maximum failure index of the satellite's side panels. . . . 74
5.3 Updated minimum bolts' MOS of the linear static analysis. . . . 75
5.4 First natural frequencies of the thermal optimized laminates. . . . 75

B.1 Laminated composite materials' properties. . . . B.92

C.1 Electronic subsystems and payload centres of gravity and mass moments of inertia. C.93
C.2 Hot and cold case thermal loads applied to each surface material. C.94

D.1 Operating ranges, minimum and maximum temperatures and temperature variation in each component for the aluminium design. D.95
D.2 Operating ranges, minimum and maximum temperatures and temperature variation in each component for the laminate design nº 3.1) ($\alpha = 0.14$). D.96
D.3 Operating ranges, minimum and maximum temperatures and temperature variation in each component for the laminate design nº 7.1) ($\alpha = 0.14$). D.96
D.4 Operating ranges, minimum and maximum temperatures and temperature variation in each component for the laminate design nº 16.1) ($\alpha = 0.14$). D.97
D.5 Operating ranges, minimum and maximum temperatures and temperature variation in each component for the laminate design nº 3.1) ($\alpha = 0.8$). D.97
D.6 Operating ranges, minimum and maximum temperatures and temperature variation in each component for the laminate design nº 7.1) ($\alpha = 0.8$). D.98
D.7 Operating ranges, minimum and maximum temperatures and temperature variation in each component for the laminate design nº 16.1) ($\alpha = 0.3$). D.98
D.8 Operating ranges, minimum and maximum temperatures and temperature variation in each component for the laminate design nº 7.3) ($\alpha = 0.8$). D.99
D.9 Operating ranges, minimum and maximum temperatures and temperature variation in each component for the laminate design nº 16.3) ($\alpha = 0.3$). D.99

List of Figures

1.1 Historic and predicted satellite launches by type [6]. 2
1.2 Schematic overview of the supported CubeSat formats and sizes (units in millimeters) [11]. 3
1.3 Static and dynamic launch environment overview (typical frequency ranges) [18]. 4
1.4 Radiation sources for an Earth-orbiting satellite. 4
1.5 Composite fibre reinforced polymer CubeSats' primary structures. 8
1.6 3U CubeSat's structure subsystem. 10
1.7 3U CubeSat's electronic subsystem and payload. 11

2.1 Laminated composite material's stacking sequence. 19
2.2 Material (lamina) coordinate system (x_1, x_2, x_3) and global coordinate system (x, y, z). 19
2.3 Laminate ply numbering. 24
2.4 Laminated composite materials' design methodology. 26

3.1 Linear static analysis loads (free body diagram). 34
3.2 External, internal and assembly views of the structural FEM model. 43
3.3 Boundary conditions scheme for each linear static load case. 44
3.4 Linear static analysis mesh convergence results. 45
3.5 Displacement, stress, strain linear static analysis results and MOS computed for the aluminium design load case B. 46
3.6 Normal mode analysis mesh convergence results. 46
3.7 First four vibration modes of the converged normal mode FEM aluminium model. 47
3.8 MOS and failure indexes results of laminate n^o 3) design for load case B. 52
3.9 MOS and failure indexes results of laminate n^o 7) design for load case B. 52
3.10 MOS and failure indexes results of laminate n^o 16) design for load case B. 52
3.11 First four vibration modes of laminate n^o 3.1) design. 53
3.12 First four vibration modes of laminate n^o 7.1) design. 53
3.13 First four vibration modes of laminate n^o 16.1) design. 53

4.1 Sensitivity study comparing temperature results for 2D and 3D structures with small thickness (units in Kelvin). 59
4.2 External, internal and assembly views of the thermal FEM model. 61
4.3 Power boards' extreme temperatures in function of the power dissipated by the boards' heaters. . . 62
4.4 Hot and cold case configurations. 63

4.5 Thermal static analysis mesh convergence results. 64
4.6 Hot and cold case temperature static thermal analysis results for the aluminium design (units in Kelvin). 64
4.7 Operating ranges, minimum and maximum temperatures and temperature variation in each component for the aluminium design. 65
4.8 Operating ranges, minimum and maximum temperatures and temperature variation in each component for the laminate design nº 3.1), 7.1) and 16.1) ($\alpha = 0.14$). 66
4.9 Operating ranges, minimum and maximum temperatures and temperature variation in each component for the laminate design nº 3.1), 7.1) and 16.1), with the respective FRP absorptivity. . . . 67
4.10 Maximum and minimum temperatures in function of the panels' absorptivity for laminate nº 3.1) design. 68
4.11 Maximum and minimum temperatures in function of the panels' absorptivity for laminate nº 7.1) design. 68
4.12 Maximum and minimum temperatures in function of the panels' absorptivity for laminate nº 16.1) design. 69
4.13 Thermal gradients of updated composite laminate designs. 70
4.14 Maximum and minimum temperatures in function of the panels' thermal conductivity for laminates with CFRP and pyrolytic graphite core design. 71
4.15 Maximum and minimum temperatures in function of the panels' thermal conductivity for laminates with GFRP and pyrolytic graphite core design. 71
4.16 Operating ranges, minimum and maximum temperatures and temperature variation in each component for the thermal optimized laminate designs nº 7.3) and 16.3). 72

5.1 MOS and failure index FEM results of laminate nº 7.3) design for load case B. 77
5.2 First four vibration modes of laminate nº 7.3) design. 77
5.3 Hot and cold case temperature thermal analysis results for laminate nº 7.3) design (units in Kelvin). 77

A.1 3U CubeSat design specification drawing [9]. A.90

C.1 Surfaces' identification number (ID). C.94

Nomenclature

Greek Symbols

α	Absorptivity
ε	Infinitesimal strain component / Emissivity
θ	Lamination angle
θ_E	Angle between Earth's center and surface normal
θ_S	Angle between incident solar radiation and surface normal
ν	Poisson's ratio
ρ	Density
σ	Stress component
σ_0	Stephan-Boltzmann constant
τ	Shear stress component
υ	Volume fraction
ϕ	Mode shape vector
ω	Angular frequency

Roman Symbols

a	Albedo
A	Extensional stiffness / Tensile area
B	Bending-extensional stiffness
C	Stiffness components
d	Nominal major diameter
D	Extensional stiffness / Wire diameter
e	Orbit eccentricity
E	Young's modulus
$\mathbf{E}$	Green-Lagrange strain tensor
f	Natural frequency
F	Force vector / Thermal loading vector / View factor
g	Earth's gravitational acceleration

G	Shear modulus
G_S	Solar flux constant
h	Orbit altitude
H	Boundary convection matrix
I	Moment of inertia
J	Torsional constant
k	Thermal conductivity
K	Laminate thermal conductivity
m	Mass
M	Moment
N	In-plane force
p	Screws pitch
P	Material's proof strength
q	Heat flux
Q	Plane stress-reduced stiffness / Heat power
S	Material's shear strength
t	Thickness
T	Transformation matrix / Temperature
u	Displacement
V	Volume
W	Nominal aperture
X	Material's strength in $x-$direction
Y	Material's strength in $y-$direction
(x,y,z)	Global (laminate) cartesian coordinate system
(x_1,x_2,x_3)	Material (lamina) cartesian coordinate system

Subscripts

1,2,3	Material cartesian components
3U	Referent to a 3U CubeSat
A	Referent to axial force / Referent to albedo
A,B	Referent to principal stresses
C	Referent to conduction
Cu	Referent to copper
E	Referent to Earth
f	Referent to fibre
g	Referent to global (laminate) coordinate system
H	Referent to convection

i, j	Referent to components / Computational indexes
I	Referent to interaction / Referent to internal heat generation
in, out	Referent to input and output
IR	Referent to infra-red
m	Referent to matrix / Referent to material (lamina) coordinate system
rad	Referent to radiation
S	Referent to shear force / Referent to solar
t	Referent to bolt threads
U	Referent to ultimate
x,y,z	Global reference frame components
Y	Referent to yield

Supercripts

’	Referent to von Mises theory
$\|\|$	Referent to longitudinal direction
$\perp$	Referent to transverse direction
$-$	Referent to global (laminate) coordinate system
0	Referent to a initial state / Referent to membrane
1	Referent to bending
C	Referent to compression state
T	Transpose / Referent to tensile state

Glossary

1D	One Dimensional
1U	One CubeSat Unit
2D	Two Dimensional
3D	Three Dimensional
3U	Triple-CubeSat
AOCS	Attitude and Orbit Control Subsystem
APG	Annealed Pyrolytic Graphite
ARALL	Aramid Fibre Reinforced Aluminium Laminate
CAD	Computer Aided Design
CARALL	Carbon Fibre Reinforced Aluminium Laminate
CDH	Command and Data Handling Subsystem
CFRP	Carbon Fibre Reinforced Polymer
CG	Centre of Gravity
CLPT	Classical Laminate Plate Theory
COTS	Commercial of-the-shelf
DOF	Degree of Freedom
ECSS	European Cooperation for Space Standardization
EPS	Electrical Power Subsystem
ESL	Equivalent Single-Layer
FEA	Finite Element Analysis
FEM	Finite Element Method
FML	Fibre Metal Laminates
FOS	Factor of Safety
FOSU	Ultimate Factor of Safety
FOSY	Yield's Factor of Safety
FRP	Fibre Reinforced Polymer
FSDT	First-order Shear Deformation Theory
GFRP	Glass Fibre Reinforced Polymer
GLARE	Glass Fibre Reinforced Aluminium Laminate
GRAV	Gravity Load

IR	Infra-red
MOS	Margin of Safety
OBC	On Board Computer
PCB	Printed Circuit Board
PMC	Polymer Matrix Composites
P-POD	Poly-Picosatellite Orbital Deployer
RBE	Rigid Body Element
SPC	Single Point Constraint
SSO	Sun Synchronous Orbit
TCS	Thermal Control Subsystem
TTC	Telemetry, Tracing and Control Subsystem

Chapter 1

Introduction

The space sector plays a crucial role in our society. Apart from scientific research and an improved understanding of our planet, solar system and universe, satellites provide economic, social infrastructures and effective security and military operations [1]. Media broadcasting, mobile networks, forecasting, disaster monitoring, and aeronautical communications are some examples of services provided by satellites [2]. As evidenced, modern society is highly dependent on space and considering that today's economy relies on the capacity of nations to develop knowledge, innovation and technology are a priority on nations agendas [3].

Traditionally, the access to space was limited to governmental institutions due to the high costs associated with the development of large and sophisticated spacecrafts [4]. However, in the last decade, space industry set a trend to develop and launch smaller satellites (satellites with a deployable mass inferior to 500 kg [5]), given their lower production costs and development time, allowing private companies to enter the space market as well [4]. This growth of smaller missions was also driven by the advancements of miniaturized technology, which foster the development of increasingly sophisticated missions without the loss of performance, and the creation of CubeSat concept [4]. Fig. 1.1 represents the number of small satellite launches of the last two decades. According to this figure, it becomes evident that the bulk of the small satellites launched are CubeSats [6]. The advancements of technology and optimization of CubeSats are, therefore, a first concern of the space industry, providing small satellites with higher potential value in terms of scientific return and commercial revenue [4].

CEiiA is a Centre of Engineering and Product Development, based in Portugal, that designs, develops and operates products in the Automotive, Aeronautics, Ocean and Space sectors, and recently, has increased its activity in space projects, aiming to develop technology and innovative solutions for small satellites. That being said, the motivation of this thesis is the study of a possible structural and thermal optimization of a CEiiA's putative CubeSat.

CubeSats have size and mass constraints, and a compromise between the structure and other subsystems and payloads is required to reach a cost effective design that will not jeopardize the satellite's mission. Composites materials may present a solution which with lightweight and customized properties could optimize this compromise and decrease the structure weight, while providing structural and thermal support required.

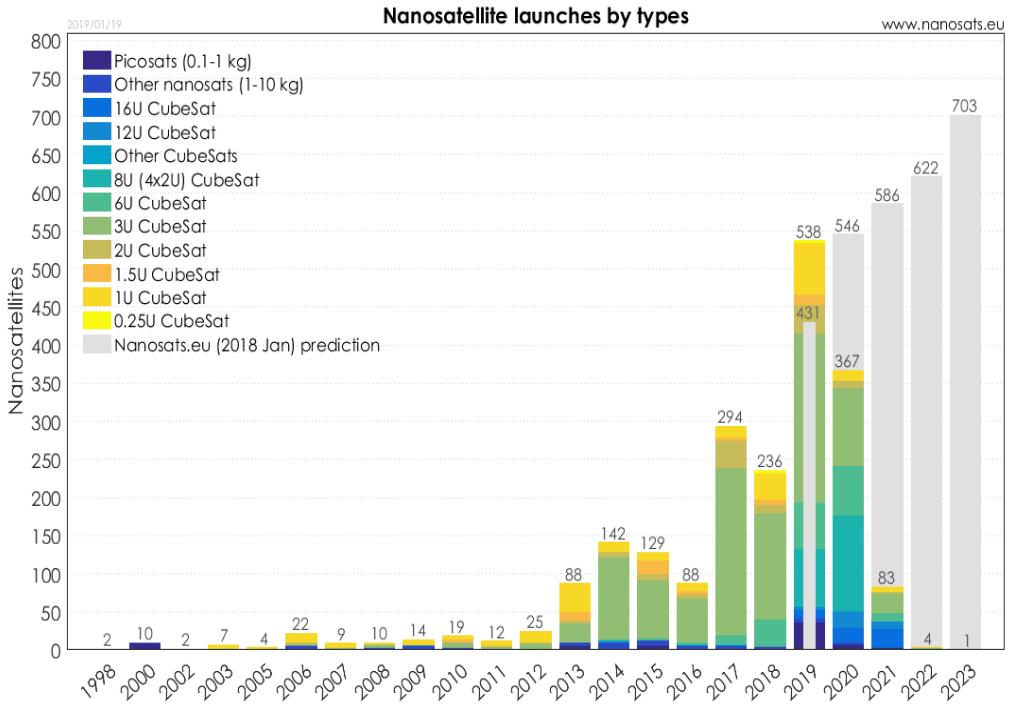

Figure 1.1: Historic and predicted satellite launches by type [6].

1.1 General Context

First developed by Dr. Jordi Puig-Suari in 1999 for educational purposes [7], CubeSats are today a standard platform for technology demonstration and scientific instrumentation capable of conducting real scientific missions as well as high value commercial missions at a fraction of the cost of traditional spacecrafts. From the study of the space environment to telecommunications analysis, the type of missions that can be performed by CubeSats are vast [8] [4].

CubeSats are a class of small satellites, that use a standard cube-shaped element, know as "one unit" (1U) with 10 cm $\times$ 10 cm $\times$ 10 cm and 1.33 kg [9]. 1U can be a satellite itself or several 1Us can build a larger spacecraft - 1.5U, 2U, 3U up to 16U, as depicted in Fig. 1.2. The standardized size allows CubeSat instruments and structure to be either based on COTS (commercial of-the-shelf) components, which main advantages are their simplicity and flight heritage, or on newly developed technology. Furthermore, the possibility to launch several CubeSats with a single rocket or as piggybacks on other launch missions, as secondary payloads, leads to low cost launches and increases the opportunities to launch [8] [10]. Hence, one can understand the increasingly interest of universities, companies and entities to develop and launch CubeSats.

Nevertheless, CubeSats brought new challenges to the design of its' subsystems. Along with size and mass constraints, CubeSats should meet additional requirements stated in the CubeSat Design Specifications, which determine their design and minimum testing prerequisites [9]. Moreover, satellites are subjected to harsh environments, that expose the satellite to structural and thermal loads. Once all the satellite's constraints, specifications and environments are defined, the critical requirements and risks can be identified and the satellite's subsystems can be designed to meet them and successfully operate [12]. In order to identify those requirements a general

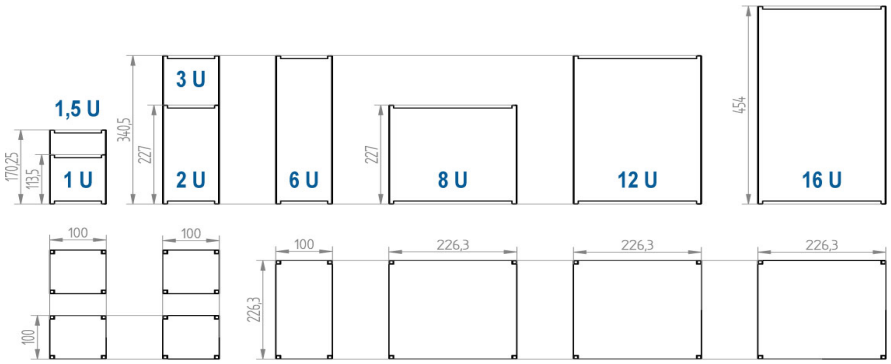

Figure 1.2: Schematic overview of the supported CubeSat formats and sizes (units in millimeters) [11].

understanding of the satellite's environments and subsystems must be attained.

1.1.1 Satellite's Environments

On-ground (manufacturing, testing and transportation), launch and in-orbit operations are the three main stages of a satellite's lifetime and in each of them the satellite is exposed to different environments [13]. Identifying, in each stage, the maximum and minimum loads that must be endured without failure or loss of performance by the satellite is crucial for the satellite's design [14]. In regard to structural and thermal loads, launch generates the highest structural loads for most satellites' structures, but the most demanding thermal environment occurs during in-orbit operations [15].

Structural Loads

Regarding the structural loads, in orbit, satellites are prone to vibrations due to several sources, however these are micro-vibrations with low amplitudes and high frequencies, up to 1 kHz. During launch, the launch vehicle will also induce vibrations on the satellite. The thrust of the engines, wind gusts and stage separation are some of the events that cause vibrations during lift-off [13]. When compared with the on-orbit vibrations, these have much higher amplitudes and lower frequencies, being structurally more demanding.

Fig. 1.3 shows the types of loads expected during launch by frequency range. As can be observed, launch loads are classified in quasi-static and dynamic loads, subdivided in sine vibrations (frequency range between 0 and 100 Hz), acoustic loads ($50 - 2000$ Hz), shock loads ($100 - 10000$ Hz) and random vibrations (acting upon all the frequency spectrum, random vibrations with frequencies under 100 Hz are covered by the sine environment and above 100 Hz covered by the acoustic loads) [14] [16].

On one hand, quasi-static loads are generated by a constant force or slowly changing with time, so that the dynamic response can be neglected [14]. On the other hand, dynamic loads vary with time. During launch, dynamic loads are a result of unsteady combustion of the engines, the turbulent flows along the rocket, the noise of the exhaust and the pyrotechnic devices used for the separation of the rocket's stages, along with several other factors [17].

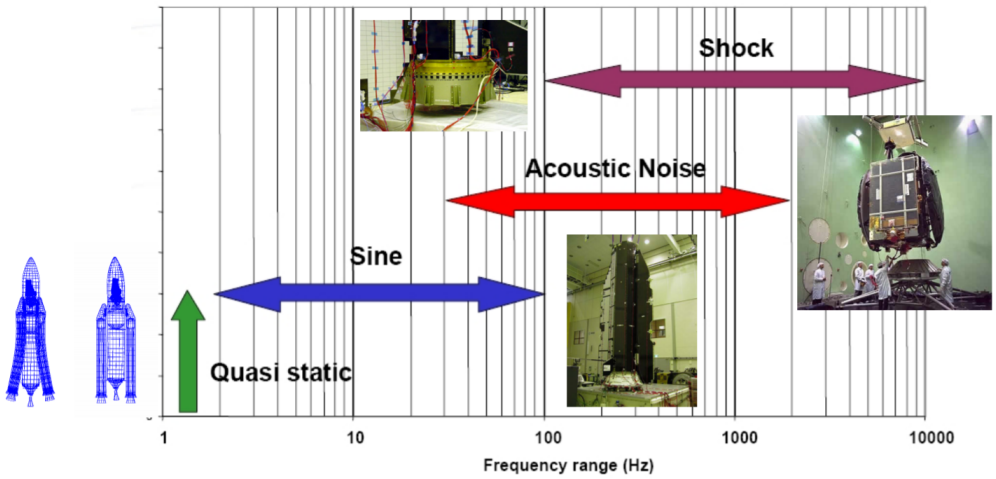

Figure 1.3: Static and dynamic launch environment overview (typical frequency ranges) [18].

Thermal Loads

Apart from structural loads, satellites are exposed to demanding thermal loads and, therefore, an understanding of the satellite thermal behaviour is not possible without the knowledge of heat transfer modes and the analysis of the boundary conditions and thermal sources involved in the satellite's orbit [19].

There are three heat transfer modes - convection, conduction and radiation. However, in space environment, due to the rarefaction of air with altitude, convection can be neglected. Consequently, satellites can only exchange thermal energy with the space environment through radiation [19].

For a satellite in Earth's orbit there are three main sources of radiation - solar radiation, Earth's albedo and Earth's infrared radiation (IR) (see Fig. 1.4). The radiation lost to space and from the surrounding components and the internal heat generated by the satellite's electrical components must be accounted as well [19].

Although radiation is the main heat transfer mode in outer space, conduction has an important role in spacecrafts, allowing thermal energy to be conducted between components and structures from heat sources to heat sinks [20].

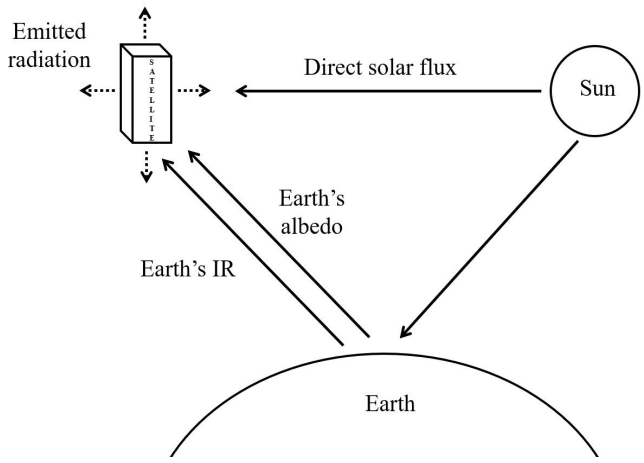

Figure 1.4: Radiation sources for an Earth-orbiting satellite.

In a typical orbital period the satellite experiences extreme cyclic temperature fluctuations and two main factors

are responsible for the cycling thermal environment.

The first reason for these fluctuations is the satellite's orbit parameters and the orbit's orientation with regard to the Sun. During its orbit, the satellite will experience in a cyclical way different solar fluxes and eclipse conditions [21], causing the satellite's temperatures to range approximately from $+100^{o}$C, when in the Sun, to -100^{o}C, during an eclipse [12]. In addition to that, the view factor of the different satellite's faces changes along the orbit, i.e. different portions of those faces will be exposed to the incoming radiation.

A second reason arises due to variations of the incoming solar flux. Energy emitted by the Sun varies with an 11 year solar cycle and, because of the eccentricity of Earth's orbit, the distance between the Earth and the Sun varies throughout the year. Therefore, annual solar flux values can range from approximately 1321.6 Wm^{-2} during the aphelion (June solistice) to 1412.9 Wm^{-2} at perihelion (December solstice) [21].

Once the structural and thermal environments are identified, the satellite's subsystems can be designed to endure them.

1.1.2 Satellite's Subsystem

Satellites can be divided into two main modules - payload and the service module. The payload is the mission's specific equipment and the service module consists on all the subsystems that allow the proper functioning of the payload. Among these subsystems there are the structure and the thermal control subsystem (TCS) [15].

Satellite's structure consists on the hardware that supports all the spacecraft components and payloads throughout the launch and provides a stable platform for on-orbit operations [15]. Hence, the structures' material selection is a vital step in satellite's design. In the case of small satellites it has an even greater importance, since small changes in the structure can result in mass savings that can be used for other subsystems or components [17]. Material selection is based on specific mass, strength and stiffness, corrosion, fracture and fatigue resistance, thermal expansion and thermal conductivity, machinability and cost. For CubeSats structures, lightweight materials with high strength and stiffness are preferred. In addition to those characteristics, aluminium alloys are easy to manufacture and thus widely used for CubeSats structures [22].

Regarding the TCS, it ensures that the temperature of different components is within their operational range. There is one clear division in the type of TCSs available - active and passive. Active TCSs require an input power to function. These subsystems are applied to sensitive equipment, providing high thermal stability, tailored to the exact temperature range required. Distinctly, passive TCSs are based on the selection of surface properties, the control of the conduction paths and the material's thermal properties, as capacity and conductivity. Thermal surfaces, thermal insulators, radiators, heat pipes and mechanical interfaces are some of the passive TCSs developed. Once installed, they do not require further spacecraft resources, like power and data handling [23]. Moreover, lightweight and high reliability make passive TCSs suitable for space applications. As such, one can understand the prevailing use of passive systems for CubeSats [24]. Coats, paints and finishings are typical passive systems added to CubeSats structures [25] [26], allowing to modify the emittance and/or absorptance of the spacecraft, thus controlling the heat flux in and out of the structure. As a matter of fact, this addition allows structures to offer both structural support and thermal control. Ergo, lightweight materials that not only have the desired thermal properties, but also good mechanical characteristics may be the key for efficient and effective structures in CubeSats and, as stated before, composite materials may be the solution sought.

1.2 State of the Art

Composite materials are defined as a combination of two or more materials, different in their properties - a continuous phase, known as matrix, and a dispersed phase, the filler/reinforcement material(s). From the mixture of those materials, composites can offer a combination of properties that cannot be achieved by each on their own [27]. The possibility to customize the material's properties with different combinations of matrix and fillers, makes composite materials extremely useful for several applications [28].

Classified according to their type of matrix, composites can be classified as polymer, metal and ceramic composites. With good mechanical properties and lightweight [29] [30], polymer matrix composites (PMCs) first emerged in 1960's for structural purposes in the aeronautic industry to compete with conventional metals [31]. Currently they are the most commonly used composites in aerospace applications [17] [30].

Regarding the reinforcements, they can be described as fibrous or particulate. Fibre reinforced composites are particularly interesting in several applications due to the enhance properties in the fibre direction, though transverse properties are usually weak. In applications where the loads state is well defined laminates can be fabricated from unidirectional fibres and its properties matched to the designs needs. However, unidirectional composites may not be suitable for applications were the loads state is not known or is approximately equal in all directions. Hence, solutions to fabricate fibre reinforced composites with fibres aligned in several direction are required [32]. In Chap. 2 composite materials are discussed in further detail.

Developments and applications of composite materials and their use for structural purposes have been very prominent in the last decades [32]. The growth in aerospace and other industries as wind energy, automotive, sports equipment and industrial machinery has increased ever since.

As can be concluded, there are different composite materials with diverse properties and vast applications and, therefore, in order to propose a structure made of composite material, it is important to understand the background and fundamental milestones of the use of composites for structural and thermal purposes in space applications, as well as in other fields of engineering, as aeronautical.

1.2.1 Composites for Aerospace Applications

As far back as the beginning of space exploration, lightweight structures have been identified as a critical need and efforts to attain the minimum mass possible made ever since [33] [12].

Although polymer composite materials started being used in 1960's for aeronautic applications, it was not until 1980's that they started to appear in the space sector [31]. In 1986, a feasibility study was conducted for the use of graphite epoxy composites on the POLAR BEAR satellite's centre support structure [34], the main conclusions were related with weight: it was estimated that the new material could reduce the structure weight by 50%, when compared with its metallic counterpart. Several authors reported similar conclusions [35] [36].

Thereafter, for lightness, high stiffness and low coefficient of thermal expansion, antenna reflectors, solar arrays, optical benches and truss elements have been made of CFRP (carbon fibre reinforced polymer composites) [31] [30] [37]. The main cargo doors and the arm manipulator of the Space Shuttle were famous employments of such materials. The CFRP cargo doors allowed a mass reduction of 23% over that of aluminium [38].

Besides providing structural support, composite materials are also used for thermal control in space systems and

several spacecraft applications can be identified accordingly, such as thermal doublers, heat sinks, space mirrors and non-structural thermal radiators, in which high specific conductivity materials are desirable [39] [40]. Specific conductivity can be defined as the thermal conductivity per unit mass and is a extremely useful unit measure for satellite systems where both high conductivity and low mass are desired properties [21].

Among several projects, Calder and Silverman [41] produced an aluminium clad CFRP thermal doubler. The design had approximately 20% lower mass and 3 times higher thermal conductivity than the baseline aluminium doubler of equivalent thickness. Another project displayed similar conclusions, a CFRP thermal doubler was incorporated in the gain antenna structure assembly of the Mars Reconnaissance Orbiter and showed thermal conductivities higher than the required minimum [42].

In 2005, Marcos et al. [43] proposed a support panel for the electronic equipments of PROTEUS satellite, acting as both thermal doubler and support. The panel consisted of a sandwich structure with two face sheets of CFRP plies bonded to an aluminium honeycomb. CFRP face sheets were built by alternating layers of high stiffness and high conductivity carbon fibres. The panel provided a mass saving of 15 % with regard to a similar aluminium plate and an increase in the homogenization of the structure's temperature.

Similar conclusions were obtained by Teti et al. [44], the authors developed a radiator panel that supported the power supply electronics of EO-1 satellite. Instead of using a polymer matrix, a carbon-carbon composite was used presenting a higher thermal conductivity in the through-the-thickness plane. However epoxy coats had to be added to provide additional strength to the panel.

Another emerging hybrid solution is high thermal conductive cores inserted within high strength structural shells, as CFRP or aluminium [45]. APG (annealed pyrolytic graphite) is a unique graphite form with a high in-plane thermal conductivity. However, APG presents poor mechanical properties, therefore encapsulating it within a structural shell addresses this limitation. In fact, when encapsulated in CFRP the resulting specific conductivity of the overall composite increased significantly. Thermal doublers, radiators and electronic packaging were developed and the main conclusion was similar for all applications: a mass reduction of approximately 40% and a decrease in thermal gradients of at least 1/3, when compared with previous materials [45].

Along with thermal doublers and radiators, due to its low mass and high thermal conductivity, other forms of pyrolytic graphite are also used for thermal control purposes [21] [46].

As can be concluded from the studies presented previously, composite materials are widely used in space applications and the insertion of high thermal conductive materials within fibre reinforced polymer (FRP) laminae is an efficient solution, when both structural and thermal performance are required.

However, a review of previous academic research into composite materials structures for CubeSats showed that the majority of CubeSats use COTS structures. Readily available, already space qualified and with flight heritage [4], one can understand COTS prevailing use over newly developed composite structures.

Nonetheless, NUTS project, based at the Norwegian University of Science and Technology, and UPSat project, from University of Patras, tested a hybrid approach of both aluminium alloy frames and CFRP panels for their primary structures to replace the typical aluminium structure [47] [48] (Fig. 1.5). In UPSat's case, the new structure was approximately 35% lighter than the aluminium one and all the structural requirements were met [49]. However, both projects only considered the use of FRP composites and did not envision the integration of other laminae to improve the thermal performance of the satellite.

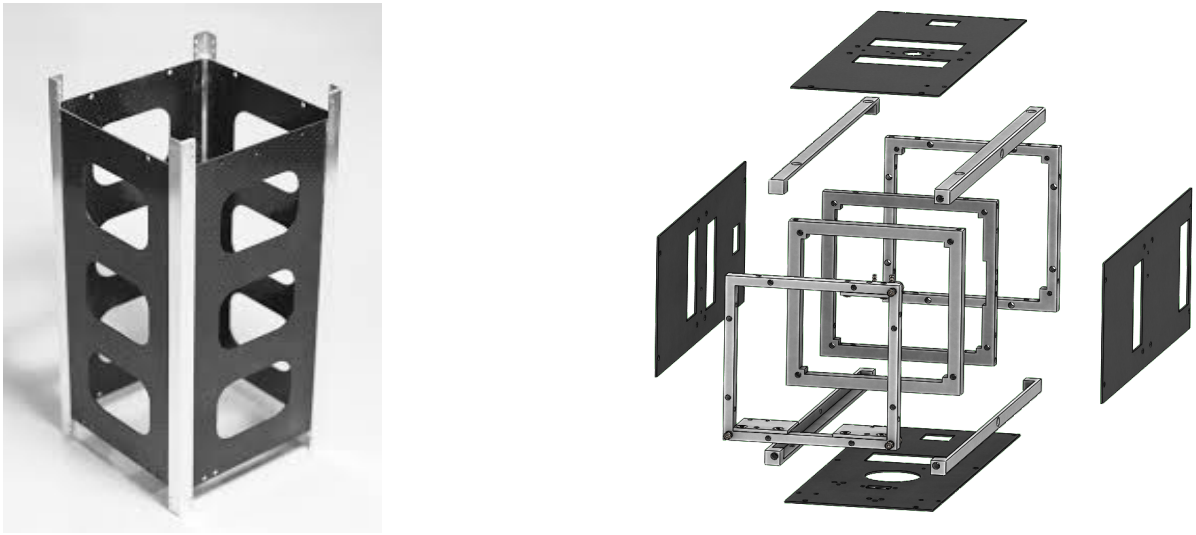

(a) NUTS structure [47]. (b) UPSat structure [48].

Figure 1.5: Composite fibre reinforced polymer CubeSats' primary structures.

Regarding the aeronautical industry, the most common material used was aluminium, due to its high stiffness, low density and corrosion resistance. However, the increasing demand in aircraft industry for high-performance and lightweight structures stimulated the development of composite materials and they started to gradually replace aluminium [50].

In 1978, with the purpose of reducing operation costs, researchers at National Aerospace Laboratory and Delft University of Technology developed fibre metal laminates (FMLs) for skins and load-carrying structures [51]. FMLs are a hybrid composite material built by alternate stacking of thin metal sheets with plies of FRP composites. Taking advantage of the hybrid nature of FMLs, these composites offer several advantages: the FRPs provide high specific strength and stiffness, and fatigue resistance, while metals offer high bearing strength, impact resistance and are easier to repair [52]. The most commercially available FMLs are ARALL (aramid fibre reinforced aluminium laminate), GLARE (GFRP aluminium laminates) and CARALL (CFRP aluminium laminates) [50].

Currently, composites, along side FMLs, are a major constituent of aircraft structures. As a matter of fact, in 2009, Boeing developed a new aircraft, Boeing 787 Dreamliner, made of approximately 50% composites [53], by comparison, Boeing previous model, Boeing 777, was made of merely 12% composites. Boeing 787 Dreamliner proved that by using composites, reductions of the aircraft weight could be attained (around 20% in global weight). [53].

Once more, it can be concluded that hybrid structures, composed of FRP with laminae of another material, as aluminium, can provide a great compromise between structural and mass requirements.

1.3 CEiiA's CubeSat Design

This section introduces the configuration and design of the structure, electronic components and payload of the 3U CubeSat to be analysed in this thesis. The design described in this chapter was provided by CEiiA. However, some design properties and features had not been previously defined, thus several assumptions and decisions had to be made by the author.

1.3.1 Design Requirements

CubeSats were first developed with the purpose of standardizing the design of satellites in order to reduce costs and development times, thus increasing the access to space. Therefore, several standards and design requirements were established that must be taken into account in the satellites being developed. These constraints are specified in the CubeSat Design Specification [9], where all the details can be consulted. The most relevant requirements for this work, in terms of configuration and material properties, are summarized here:

1. The 3U CubeSat configuration and physical dimensions shall be defined as in appendix A, with 100 mm $\times$ 100 mm $\times$ 340.5 mm as the external dimensions;
2. No components on the identified green and yellow sides of Fig. A.1 shall exceed 6.5 mm normal to the surface;
3. Rails must have a minimum width of 8.5 mm and a minimum surface area of 6.5 mm $\times$ 6.5 mm;
4. Aluminium 7075, 6061, 5005 and/or 5052 must be used for the main CubeSat structure and rails;
5. The CubeSat rails which contact with the Poly-Picosatellite Orbital Deployer (P-POD) rails shall be hard anodized to prevent cold welding;
6. The maximum allowed mass of a 3U CubeSat is 4 kg.

Furthermore, structural and thermal requirements, as the ones to be presented in Secs. 3.1.1 and 4.1.2, must be met by the CubeSat. However, only through analysis is it possible to access if these requirements are satisfied and decide if the design needs to be revised.

1.3.2 Structure Subsystem

As defined by the European Cooperation for Space Standardization (ECSS) [54], a satellite structure is a ”set of mechanical components or assemblies designed to sustain loads or pressures, provide stiffness or stability, or provide support or containment”. Hence, one can say that the general function of a satellite structure is to provide support to the subsystems and payloads to correctly operate and perform its mission under certain environments.

The satellite’s structure can be divided into external and internal. In Figs. 1.6 (a) and (b) both 3U CubeSat’s structures can be found. The different parts of the structure are identified in the respective figures, namely the rails, the systems supports, the payload supports and the side panels. All are initially made of hard anodized aluminium 6061 T6.

1.3.3 Electronic Subsystem and Payload

Satellites have several electronic subsystems that guarantee the correct operation of its payload during its mission. Fig. 1.7 depicts the CubeSat subsystems configuration. Essentially, an electronic stack is mounted on the higher section of the satellite. This stack consists of six printed circuit boards (PCB) each with an average thickness of 1.6 mm. The material used in this boards is a layered laminate of FR-4 (composite material of woven

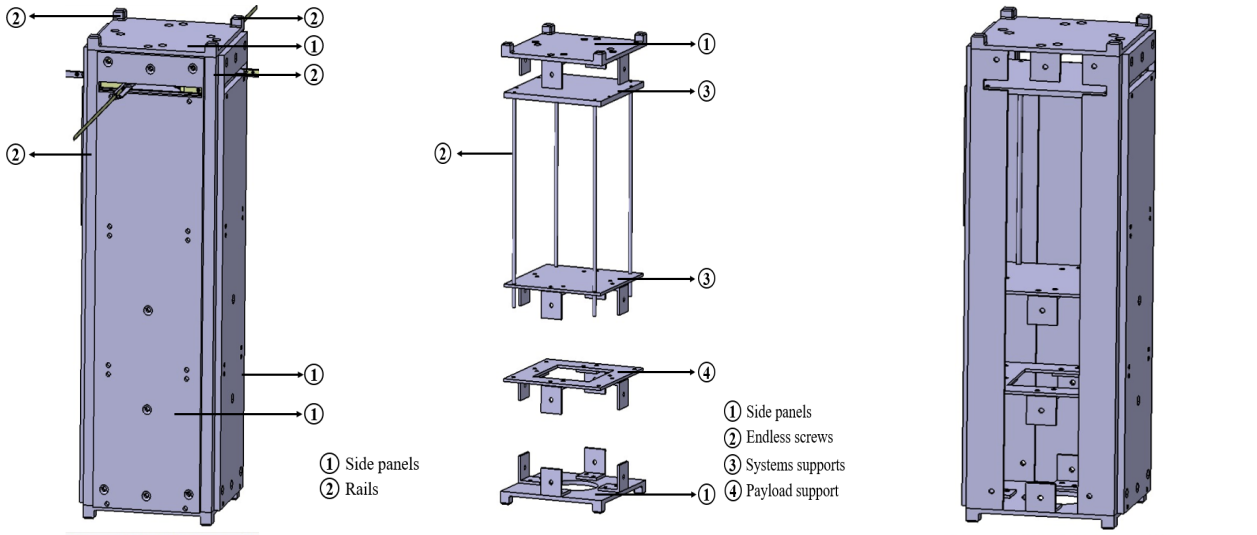

(a) External structure. (b) Internal structure. (c) External and internal structure assembly.

Figure 1.6: 3U CubeSat's structure subsystem.

glass reinforced epoxy resin) and copper. The number of copper layers can vary typically from 2 to 8. Each subsystem is composed by a PCB plus the specific devices.

The satellite's subsystems and payload can be summarized as follows:

1. Telemetry, Tracking and Control Subsystem (TTC): Two components from ISIS to support all the electronics necessary to transmit and receive information from the satellite to a ground station are mounted on the CubeSat:

   (a) Antenna [55];

   (b) Transceiver [56].

2. Electrical Power Subsystem (EPS):

   (a) Power boards: Two GomSpace NanoPower BP4 batteries [57] store the power generated by the solar panels. Each board has four lithium ion cells [58] and a heater that can dissipate up to 7 W to ensure the temperature of the battery cells remains within its operational range;

   (b) Power control board: One GomSpace NanoPower P31uX power management board [59] regulate and distribute the power to all the subsystems that require electric energy;

   (c) Solar panels: To generate electric power a total of nine EnduroSat solar panels [60] are fixed to three satellite's lateral faces. Each solar panel has two solar cells, i.e total of eighteen solar cells are mounted on the satellite.

3. Command and Data Handling Subsystem (CDH): On Board Computer (OBC) module from Pumpkin Space Systems [61] is used, providing the satellite with all the processing capabilities it requires;

4. Attitude and Orbit Control Subsystem (AOCS): A ISIS Magnetorquers board [62] is responsible for determining the satellite orientation and position, assuring the desirable orientation;

5. Payload: A GomSpace NanoCam C1U [63] is the nanocamera included in this CubeSat.

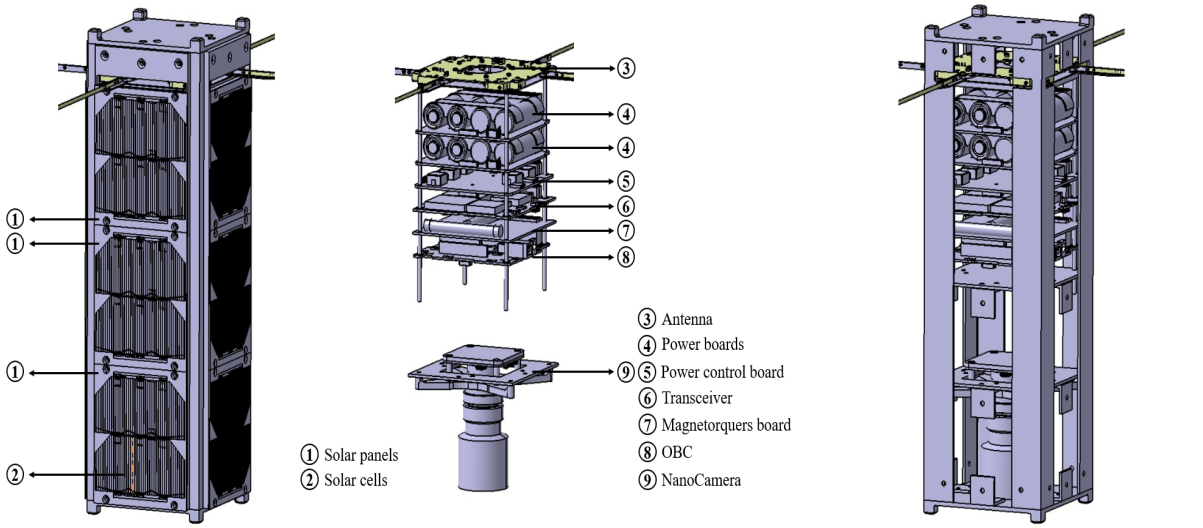

(a) Eletronic subsystems and payload configuration.

(b) Electronic subsystem and payload assembly.

Figure 1.7: 3U CubeSat's electronic subsystem and payload.

In Tab. 1.1 some properties of each component are presented, namely their quantity, mass and corresponding operational temperature ranges.

Table 1.1: Electronic subsystems and payload general properties.

Subsystem	Component	Quantity	Mass [g]	Operational temperature range [^{o}C]
TTC	Antenna [55]	1	85	-20 to 60
	Transceiver [56]	1	75	-20 to 60
EPS	Power board [57] [58]	2	258	0 to 45
	Power control board [59]	1	100	-40 to 85
	Solar Panels [60]	9	44	-55 to 150
CDH	OBC [61] [64]	1	76.5	-40 to 85
AOCS	Magnetorquers board [62]	1	196	-40 to 70
Payload	NanoCamera [63]	1	277	0 to 60

1.4 Thesis' Contribution and Objectives

The main purpose of this work is to reduce the structural mass of CEiiA's putative satellite without compromising its structural and thermal integrity. Therefore, the challenge is to develop a solution that has a lower weight than the conventional aluminium alloy CubeSat's structures by replacing the satellites side panels with laminated composite materials. In order to assess safety and integrity the satellite structural and thermal behaviour must be analysed.

Engineering problems can be solved by means of three methods: classical, numerical and experimental [65].

Classical methods attempt to solve different problems directly by forming governing equations based on fundamental physic principles, allowing a high degree of understanding about the problem under analysis. However, it is not possible to compute exact solutions for complex geometries, loading and boundary conditions. Hence, this methods bear little resemblance to most practical engineering problems [65].

In order to address a broader range of problems, numerical methods are implemented. The Finite Element Method (FEM) is one of the most commonly used numerical techniques. This method allows the idealization of a physical problem in to a mathematical one [65].

Experimental methods attempt to solve the physical problems by experimenting on a prototype [65].

In the case of a satellite, experimental methods are required on the final stages of development. However, in preliminary stages or whenever new designs need to be tested, numerical methods are performed prior to experimental ones, since they can give the insights required to understand if the changes made to the model are effective or attain the objectives sought. Given that, in this thesis, a preliminary study on the use of composite materials for structural and thermal purposes in a satellite is performed and numerical methods are used, more precisely the FEM.

Three different analyses are performed: linear statics, normal modes and static thermal analysis. If the obtained results do not comply with the requirements defined, the laminated composite materials must be optimized and an optimization cycle is then carried out until the requirements are met.

The laminated composite materials to be analysed in this thesis are either made of unidirectional CFRP or GFRP composites, with aluminium, copper mesh or pyrolytic graphite laminae to meet the thermal requirements. The selection of these type of materials resulted from the material's availability on the CEiiA's testing laboratory and from the state of the art studies previously presented.

By the end of this work, an optimized structure that can be further developed, experimentally tested and used as a standard material not only for this CubeSats mission but also for others satellite missions.

1.5 Thesis Outline

This thesis is organized in five chapters as follows.

Chapter 1 provides a general context on satellites. An overview of the structural and thermal loads that must be withstood by satellites during their lifetime and the satellite's subsystems, with focus on structure and thermal control system, are presented. An overall description of the growing use of composite materials in aerospace applications is presented.

Chapter 2 is devoted to a theoretical overview of composite materials. The equations of anisotropic elasticity and the mechanical behaviour of a lamina as an orthotropic material are detailed. Then, laminated composites, more specifically fibre reinforced ones, are addressed. The definition of the equivalent single-layer structural and thermal properties of laminated composite materials and hybrid structures are presented. Moreover, the design process and optimization cycle implemented in this dissertation is described. The possible solutions using laminated composite materials to be implemented as the satellite's side panels are identified and their equivalent single-layer properties computed.

Chapter 3 presents the theoretical background that supports the structural FEM analyses. The structural envi-

ronment is presented and the satellite structural requirements are defined. The theory related to the linear static and normal mode analysis to be developed is provided and the failure criteria used presented. The development of the structural FEM models (linear static and normal mode) and the simulations results for the structural optimization of the composite laminates are also presented.

Chapter 4 presents an overview on the space thermal environment and the satellite's thermal requirements are defined. The theory overview related to the static thermal analysis to be developed is provided. The development of the thermal FEM model and the simulations results for the laminates thermal optimizations performed are presented.

In chapter 5 the final thermo-structural simulations' results are presented for the optimized composite laminates. The discussion of the results obtained is provided.

Chapter 6 provides the thesis findings and conclusions. Future work and recommendations are given.

Chapter 2

Composite Materials

The purpose of this chapter is to present an overview on the theoretical background required for the analysis of composite materials, with particular focus on unidirectional fibre reinforced composites.

First the basic equations that govern the motion of linear elastic bodies are reviewed, namely the constitutive equations for anisotropic and orthotropic materials, the plane stress-reduced and the strain-reduced constitutive equations.

Then a brief introduction to composite materials is provided, in which the lamina and laminate concepts are exposed. The mechanical behaviour of a lamina is presented and the stress and strain transformation relations derived. Finally, the governing equations of a laminated composite are obtained.

Note that an extensive review is not made, only the most important topics to understand the current work are discussed. A complete review of these topics is available in literature, such as in the books by Reddy [66], Kaw [67] and Altenbach et al. [32].

Once the theoretical overview is complete, the methodology to design and select the laminated composite materials to be studied is presented, as well as the materials' mechanical and thermal properties.

2.1 Theoretical Background

2.1.1 Generalized Hooke's Law

Constitutive equations are those which characterize the material and state how it reacts to applied loads. Concerning linear elastic materials, the constitutive equations are a function of the current state of deformation. The state of deformation is then described by a linear relation between the states of stress and strain [66].

There are several ways to measure the deformation of a body, the most common in solid mechanic is the Green-Lagrange strain tensor $\mathbf{E}$, usually expressed in terms of the displacement $\mathbf{u}$ (u, v, w) [66]. When the displacement gradients are small ($\|\Delta\mathbf{u}\| << 1$) the Green-Lagrange tensor $\mathbf{E}$ reduces to the infinitesimal strain tensor ε. For a detailed explanation consult reference [66]. In the present work, the assumption of infinitesimal deformations is used. The infinitesimal strains ε are from now on simply refereed to as strains.

The linear constitutive relations are then defined according to the generalized Hooke's law, for infinitesimal

deformation, as

$$\sigma_{ij} = C_{ij}\varepsilon_{ij} + \sigma^0_{ij}, \tag{2.1}$$

where C_{ij} is the material's stiffness tensor and σ^0_{ij} the initial state of stress of the material. In the present work the reference configuration is considered stress free, i.e. $\sigma^0_{ij} = 0$. A single subscription notation for the stresses and strains is from this point on employed as follows:

$$\sigma_1 = \sigma_{11}, \sigma_2 = \sigma_{22}, \sigma_3 = \sigma_{33}, \sigma_4 = \sigma_{23}, \sigma_5 = \sigma_{13}, \sigma_6 = \sigma_{12}, \tag{2.2a}$$

$$\varepsilon_1 = \varepsilon_{11}, \varepsilon_2 = \varepsilon_{22}, \varepsilon_3 = \varepsilon_{33}, \varepsilon_4 = \varepsilon_{23}, \varepsilon_5 = \varepsilon_{13}, \varepsilon_6 = \varepsilon_{12}. \tag{2.2b}$$

Accordingly, the Hooke's law takes the form:

$$\sigma_i = C_{ij}\varepsilon_j, \tag{2.3}$$

or, in matrix form,

$$\begin{Bmatrix} \sigma_1 \\ \sigma_2 \\ \sigma_3 \\ \sigma_4 \\ \sigma_5 \\ \sigma_6 \end{Bmatrix} = \begin{bmatrix} C_{11} & C_{12} & C_{13} & C_{14} & C_{15} & C_{16} \\ C_{12} & C_{22} & C_{23} & C_{24} & C_{25} & C_{26} \\ C_{13} & C_{23} & C_{33} & C_{34} & C_{35} & C_{36} \\ C_{14} & C_{24} & C_{34} & C_{44} & C_{45} & C_{46} \\ C_{15} & C_{25} & C_{35} & C_{45} & C_{55} & C_{56} \\ C_{16} & C_{26} & C_{36} & C_{46} & C_{56} & C_{66} \end{bmatrix} \begin{Bmatrix} \varepsilon_1 \\ \varepsilon_2 \\ \varepsilon_3 \\ \varepsilon_4 \\ \varepsilon_5 \\ \varepsilon_6 \end{Bmatrix}. \tag{2.4}$$

The stiffness coefficients C_{ij} are related to the materials properties E_i, G_{ij} and ν_{ij}. E_i is the Young's modulus in the x_i- direction, G_{ij} the shear modulus in the $x_i x_j-$ plane and ν_{ij} the Poisson's ratio. As can be concluded from Eq. 2.4, there are 21 independent stiffness coefficients for anisotropic elastic materials. An anisotropic material is that which have directionally dependent properties. However, there are materials that present plates of symmetry which reduce the number of independent coefficients. Orthotropic materials have three mutually orthogonal planes of symmetry, which lead to the reduction of independent coefficients to 9. The Hooke's law for orthotropic materials is given by,

$$\begin{Bmatrix} \sigma_1 \\ \sigma_2 \\ \sigma_3 \\ \sigma_4 \\ \sigma_5 \\ \sigma_6 \end{Bmatrix} = \begin{bmatrix} C_{11} & C_{12} & C_{13} & 0 & 0 & 0 \\ C_{12} & C_{22} & C_{23} & 0 & 0 & 0 \\ C_{13} & C_{23} & C_{33} & 0 & 0 & 0 \\ 0 & 0 & 0 & C_{44} & 0 & 0 \\ 0 & 0 & 0 & 0 & C_{55} & 0 \\ 0 & 0 & 0 & 0 & 0 & C_{66} \end{bmatrix} \begin{Bmatrix} \varepsilon_1 \\ \varepsilon_2 \\ \varepsilon_3 \\ \varepsilon_4 \\ \varepsilon_5 \\ \varepsilon_6 \end{Bmatrix}. \tag{2.5}$$

From Eq. 2.5, one can observe that for orthotropic materials, normal strains cause only normal stresses and shear strains cause only shear stresses.

Note that generally temperature can influence the stress results in two ways: first, stiffness coefficients can be temperature dependent and, secondly, stresses may be added to the material due to the their thermal expansion, the so-called thermal stresses. However, in this study it is assumed that those coefficients are constant with temperature

and thermal stresses will only be discussed later on.

Plane Stress and Plane Shear Constitutive Relations

There are situations in which the body is considered to be in plane stress and/or plane shear. In such cases the stress-strain relation previously presented in Eqs. 2.4 and 2.5 needs to be revised.

A state of generalized stress is one in which

$$\sigma_{\alpha\beta} = \sigma_{\alpha\beta}(x_1,x_2), \tag{2.6a}$$

$$\sigma_{\alpha 3} = \sigma_{\alpha 3}(x_1,x_2), \tag{2.6b}$$

$$\sigma_{33} = 0, \tag{2.6c}$$

where α and β take the values 1 and 2. Usually bodies with their thickness much smaller than the other two dimensions are considered to be in a state of plane stress.

As for a state of generalized plane shear the following expressions hold,

$$\varepsilon_{\alpha 3} = 0, \tag{2.7a}$$

$$\varepsilon_{33} = 0, \tag{2.7b}$$

where $\alpha = 1,2$.

Hence, the constitutive equations of an orthotropic body in a state of plane stress and plane shear can be simply written as

$$\begin{Bmatrix} \sigma_1 \\ \sigma_2 \\ \sigma_6 \end{Bmatrix} = \begin{bmatrix} Q_{11} & Q_{12} & 0 \\ Q_{12} & Q_{22} & 0 \\ 0 & 0 & Q_{66} \end{bmatrix} \begin{Bmatrix} \varepsilon_1 \\ \varepsilon_2 \\ \varepsilon_6 \end{Bmatrix}, \tag{2.8}$$

where Q_{ij} are called the plane stress-reduced stiffnesses. The reduced stiffnesses coefficients are given in function of the engineering constants through the following equations,

$$Q_{11} = \frac{E_1}{1-\nu_{12}\nu_{21}}, \tag{2.9a}$$

$$Q_{12} = \frac{\nu_{12}E_2}{1-\nu_{12}\nu_{21}}, \tag{2.9b}$$

$$Q_{22} = \frac{E_2}{1-\nu_{12}\nu_{21}}, \tag{2.9c}$$

$$Q_{66} = G_{12}, \tag{2.9d}$$

where

$$\nu_{21} = \nu_{12}\frac{E_2}{E_1}. \tag{2.10}$$

Note that only four independent material constants are involved for orthotropic materials in plane stress and shear.

2.1.2 Laminated Composite Materials

Composite materials are those made of two or more materials. The main objective of the usage of composite materials is the possibility to incorporate different components with distinct properties within one structure, achieving a final material with combined properties that cannot be attained with any of the original components. Some of the material properties that can be improved by forming a composite are stiffness, strength, weight reduction, thermal conductivity, fatigue life and corrosion resistance [66]. In order to better understand how these improvements can be accomplished, it is crucial to grasp the basics of composite materials theory.

A typical sheet of composite material is known as a lamina or ply, which is the fundamental "building block" of composite materials. Laminae can either be particulate or fibrous. Particulate composite materials are composed of macro size particles of one material in a matrix of another. Whereas, fibre reinforced lamina consist of fibres of one material embedded in a matrix of another. The fibres can be continuous or discontinuous, distributed in an unidirectional, bidirectional, random way or in a woven pattern. According to the required behaviour, the different fibre distributions are applied and the behaviour of the lamina can range between anisotropy to quasi-isotropy [32]. In the present work only fibre reinforced laminae with an unidirectional distribution will be analysed.

In a fibre reinforced lamina, the matrix materials preserve their bulk-form properties and keep the fibres together protecting them from the environment, while the fibres exhibit directionally dependent properties that determine the mechanical and thermal properties of the composite [66].

Once the plys are defined, laminated composite materials can be produced. The properties of each lamina, as the type of fibre and matrix, and the fibre volume ratio, determine the laminate properties, as well as their stacking sequence (also called lamination scheme) and orientation with regard to each other. It is exactly this possibility to alter the laminae sequence and orientations that provide designers flexibility to tailor the properties of the laminate to match the design requirements [66].

Fig. 2.1 shows a laminate made of unidirectional fibre reinforced laminae with different fibre orientations, represented by θ (lamination angle), in degrees. To introduce the notation of the stacking sequence of laminates, the laminate in Fig. 2.1 is used as an example. Its lamination scheme is $(0/+\theta/-\theta/90/-\theta/+\theta/0)$, where 0 is the orientation of the first ply, $+\theta$ of the second ply, and so on. The plys are counted in the positive z-direction. Unless stated otherwise, this notation implies that all layers have the same thickness and material. This specific lamination scheme is symmetric, since symmetry of the lamination scheme in respect to the laminate's midplane is observed.

Composite materials present several advantages, however some issues due to the mismatch of material properties between the layers, the matrix and the fibres can arise. Also, manufacturing problems may introduce several defects to the laminate.

One of the failure mechanisms is called delamination, and consists in the separation of layers from one another. The variation of stresses through-the-thickness is the main responsible of delamination, even if a laminate is loaded by uniform in-plane loads [32]. In the present work these issues are not taken into account, except in the thermal analysis, where small thermal gradients within the laminate structure are sought to decrease thermal stresses.

In order to assess the effect of different laminae and stacking sequence in the global behaviour of a laminate, analytical models to compute the laminate properties are used and a three step method is typically implemented.

The first step consists in determining the constitutive equations of the laminae. The transverse and longitudinal effective elastic moduli and thermal conductivity constants must be previously computed.

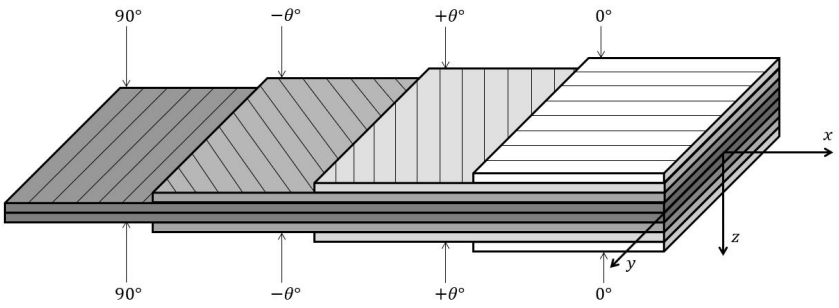

Figure 2.1: Laminated composite material's stacking sequence.

Secondly, since stacking sequence may presuppose different fibre orientations, hence different material coordinate systems, it is essential to establish transformation relations among stresses, strains and thermal properties to switch from a material (lamina) coordinate system (x_1, x_2, x_3) to a global (laminate) coordinate system (x, y, z). In Fig. 2.2, both material and global coordinate systems are depicted. The author simply states the transformation relations mentioned above, since the derivation of these transformation relations can be consulted in literature, for example in Reddy [66].

In the third and final step, the laminate constitutive equations and the computation of the structural and thermal properties of the laminate are obtained. In order to model composite laminates, different approaches and theories have been developed and applied for several decades. The analysis of laminates can be divided into three main groups: three-dimensional elasticity theories, equivalent single-layer theories (ESL) and multiple model methods [66]. A comprehensive review on the three different modelling approaches is available in literature [66] [68]. In the present work, the equivalent single-layer theories are used, more specifically the classical laminated plate theory (CLPT).

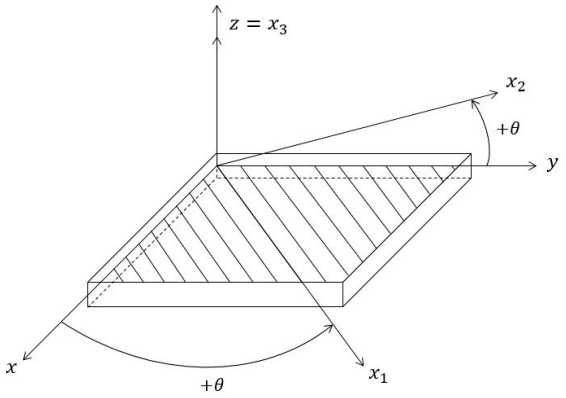

Figure 2.2: Material (lamina) coordinate system (x_1, x_2, x_3) and global coordinate system (x, y, z).

Constitutive Equations of a Lamina

The mechanical behaviour of unidirectional fibre reinforced lamina is described in accordance with two assumptions [66]:

1. A lamina is a continuum, which means that there are no empty space or gaps within the lamina;

2. A lamina is a linear elastic material, which implies that the material obeys to the generalized Hooke's law.

Additionally, unidirectional fibre reinforced laminae can be treated as orthotropic materials with symmetry planes parallel and transverse to the fibre direction [66]. In Fig. 2.2 the material coordinate system (x_1, x_2, x_3) of this kind of lamina is represented. As can be depicted the x_1-axis is oriented along the fibre direction and x_2-axis is transverse to it, both axes are in the plane of the lamina. The third axis, x_3-axis, is transverse to the plane of the lamina and oriented along the thickness direction.

In order to determine the engineering constants of unidirectional fibre reinforced laminae, a micromechanical approach is used and the following assumptions made [66]:

1. It is considered that perfect bonding between fibres and matrix exists;
2. Fibres are parallel to each other and uniformly distributed throughout the matrix;
3. The matrix does not present microcracks or voids and is initially in a stress-free state;
4. Hooke's law is obeyed by the fibres and matrix, and both are considered isotropic;
5. The applied decomposed loads are either perpendicular or parallel to the fibre direction.

Regarding structural properties, the parallel model, better known as rule of mixture, is used to compute the lamina's elastic constants in the longitudinal direction. As for the transverse direction, the Reuss estimate, also known as the inverse rule of mixtures, is widely used [32]. The rule of mixtures states that the composite properties are equal to the sum of each constituent's properties multiplied by their volume fractions [66].

The lamina's volume fraction dictates the behaviour of composites. It expresses the proportion of matrix and fibres within the material. For a fibre reinforced material, the matrix and fibre volume fractions are, respectively, defined as

$$\upsilon_m = \frac{V_m}{V}, \tag{2.11a}$$

$$\upsilon_f = \frac{V_f}{V}, \tag{2.11b}$$

where V_m is the matrix volume, V_f the fibre volume and V the total volume of the composite. In a two phase composite $V = V_f + V_m$ and, consequently, $\upsilon_f + \upsilon_m = 1$ [32].

For unidirectional fibre reinforced composites, the longitudinal and transverse Young's modulus, E_1 and E_2, the shear modulus G_{12} and the Poisson's ratio ν_{12} of a lamina can be given by Eqs. 2.12, 2.13, 2.14 and 2.15, respectively,

$$E_1 = E_f \cdot \upsilon_f + E_m \cdot \upsilon_m, \tag{2.12}$$

$$E_2 = \frac{E_f \cdot E_m}{E_f \cdot \upsilon_f + E_m \cdot \upsilon_m}, \tag{2.13}$$

$$G_{12} = \frac{G_f \cdot G_m}{G_f \cdot \upsilon_f + G_m \cdot \upsilon_m}, \tag{2.14}$$

$$\nu_{12} = \nu_f \cdot \upsilon_f + \nu_m \cdot \upsilon_m, \tag{2.15}$$

where E_f and E_m are the Young's moduli of the fibres and matrix, G_f and G_m the shear moduli of the fibres and matrix, ν_f is the fibre Poisson's ratio and ν_m the matrix Poisson's ratio. Since, fibres and matrix are assumed to be isotropic their shear moduli, G_f and G_m, can be determined as follows [66]

$$G_f = \frac{E_f}{2(1+\nu_f)}, \tag{2.16a}$$

$$G_m = \frac{E_m}{2(1+\nu_m)}. \tag{2.16b}$$

As for the composite thermal properties, several authors agree that the rule of mixtures is the most suitable model for the longitudinal thermal conductivity k_1 [69] [70] [71]. However, for the transverse thermal conductivities, k_2 and k_3, the Charles & Wilson model [72] is considered by several authors as a suitable model that provides satisfactory results for unidirectional fibre reinforced lamina [73] [74]. The effective longitudinal and transverse thermal conductivities of a lamina are then given by

$$k_{11} = k_f^{||} \cdot \upsilon_f + k_m \cdot \upsilon_m, \tag{2.17a}$$

$$k_{22} = k_f^{\perp} \frac{k_f^{\perp}(1+\upsilon_f) + k_m(1-\upsilon_m)}{k_f^{\perp}(1-\upsilon_f) + k_m(1+\upsilon_m)}, \tag{2.17b}$$

$$k_{33} = k_{22}, \tag{2.17c}$$

where $k_f^{||}$ and $k_f^{\perp}$ are the longitudinal and transverse thermal conductivities of the fibres and k_m is the matrix thermal conductivity. In a matrix form the effective thermal conductivity tensor, for an unidirectional fibre reinforced lamina, is the following:

$$k_{ij} = \begin{bmatrix} k_{11} & 0 & 0 \\ 0 & k_{22} & 0 \\ 0 & 0 & k_{33}. \end{bmatrix} \tag{2.18}$$

Coordinate Transformations

The constitutive equations of a lamina and the effective thermal conductivity tensor are usually written in terms of stress, strain and thermal conductivity components that are referred to the material coordinate system. However, laminated composite materials are built by stacking several layers of laminae with their x_1x_2-planes parallel to each other and with the ply's x_3-axis coincident with the z-axis of the global coordinate system (see Fig. 2.2). Therefore, the distinct laminae are able to have different orientations. Hence, it is essential to establish a transformation relation between the lamina coordinate system and a global coordinate system. The coordinate transformation for each layer is then an in-plane rotation of the lamination angle θ.

These relations are used to transform the constitutive Eqs. 2.8 and the effective thermal conductivity tensor 2.18 from the lamina coordinate system (x_1, x_2, x_3) to the laminate coordinate system (x, y, z) (see Fig. 2.2). The transformation matrix (T) that relates both systems is defined as follows [66]

$$\begin{Bmatrix} x \\ y \\ z \end{Bmatrix} = \begin{bmatrix} \cos\theta & -\sin\theta & 0 \\ \sin\theta & \cos\theta & 0 \\ 0 & 0 & 1 \end{bmatrix} \begin{Bmatrix} x_1 \\ x_2 \\ x_3 \end{Bmatrix} = \left[T\right] \begin{Bmatrix} x_1 \\ x_2 \\ x_3 \end{Bmatrix}. \tag{2.19}$$

Consequently, the stress equation in the global coordinate system is computed as

$$\left[\sigma\right]_g = \left[T\right]\left[\sigma\right]_m\left[T\right]^T, \tag{2.20}$$

where the subscripts g and m denote the global and the material coordinate systems. An equivalent transformation can be obtained for the strain tensor ε_{ij}.

$$\left[\varepsilon\right]_g = \left[T\right]\left[\varepsilon\right]_m\left[T\right]^T. \tag{2.21}$$

Since constitutive equations are usually written in terms of the single subscripts stress and strain components (as presented in Eq. 2.5), the transformation matrix must be rearranged, taking the following form:

$$\left\{L\right\} = \begin{bmatrix} \cos^2\theta & \sin^2\theta & 0 & 0 & 0 & -\sin 2\theta \\ \sin^2\theta & \cos^2\theta & 0 & 0 & 0 & \sin 2\theta \\ 0 & 0 & 1 & 0 & 0 & 0 \\ 0 & 0 & 0 & \cos\theta & \sin\theta & 0 \\ 0 & 0 & 0 & -\sin\theta & \cos\theta & 0 \\ \sin\theta\cos\theta & -\sin\theta\cos\theta & 0 & 0 & 0 & \cos^2\theta - \sin^2\theta \end{bmatrix}. \tag{2.22}$$

The transformed stiffness matrix is then given for orthotropic materials by

$$\left[C\right]_g = \left[L\right]\left[C\right]_m\left[L\right]^T = \left[\overline{C}\right]. \tag{2.23}$$

and the Hooke's law in the global coordinate system as

$$\left\{\sigma_i\right\}_g = \left[\overline{C}_{ij}\right]\left\{\varepsilon_j\right\}_g. \tag{2.24}$$

Concerning the effective thermal conductivity tensor k_{ij}, its components are transformed identically to stress. Hence, the effective thermal conductivity tensor is given, in the global coordinate system, by

$$\left[k\right]_g = \left[T\right]\left[k\right]_m\left[T\right]^T. \tag{2.25}$$

After the laminae's properties are defined in the global coordinate system, the laminate constitutive equations and equivalent single-layer properties can be computed.

Constitutive Equations of a Laminate

Laminated composite materials usually have their planar dimensions much larger than their transverse one (i.e. at least one order larger than their thickness). Hence laminates are often treated as plate elements and modelled according to plate theories. Equivalent single layer (ESL) laminated plate theories allow an heterogeneous laminated plate to be treated as a statically equivalent single layer material with a complex constitutive behaviour. The constitutive behaviour of such plates is, then, a sum of through-the-thickness integrated contributions of each ply. Furthermore, ESL theories enable the reduction of three dimensional problems to two-dimensional ones.

The most common ESL are the classical laminated plate theory (CLPT) and the first-order shear deformation

theory (FSDT). Further information on CLPT and FSDT can be found in literature, as the book by Reddy [66]. In the present work, the constitutive equations formulation act in accordance to CLPT.

Classical laminated plate theory is an extension of the classical or Kirchhoff plate theory (for further information on the Kirchhoff theory consult references Ugural [75] and Szilard [76]) and is based on the following Kirchhoff hypothesis [66]:

1. Straight lines perpendicular to the midsurface, i.e. transverse normals, before deformation remain straight after deformation;

2. Transverse normals do not experience elongation, i.e. they are inextensible;

3. Transverse normals rotate such that they remain perpendicular to the midsurface after deformation.

The previous assumptions imply that the transverse displacement is independent of the thickness, $z-$coordinate, and that the transverse normal strain ε_{zz} is zero. Furthermore, from the hypothesis also follow that the transverse shear strains are null - $\varepsilon_{xz}=0$, $\varepsilon_{yz}=0$. Note that typically, the plate is considered to be in a state of plane stress and, thus, in the CLPT, both plane stress and strain are assumed. Therefore, the relations presented in Eq. 2.8 are used to define the mechanical behaviour of each ply.

According to CLPT, the equations that relate the in-plane force resultants (N_{xx},N_{yy},N_{xy}) and moment resultants (M_{xx},M_{yy},M_{xy}) to the strains of a laminate are, respectively, given by Eqs. 2.26 and 2.27,

$$\begin{Bmatrix} N_{xx} \\ N_{yy} \\ N_{xy} \end{Bmatrix} = \begin{bmatrix} A_{11} & A_{12} & A_{16} \\ A_{12} & A_{22} & A_{26} \\ A_{16} & A_{26} & A_{66} \end{bmatrix} \begin{Bmatrix} \varepsilon_{xx}^{(0)} \\ \varepsilon_{yy}^{(0)} \\ \gamma_{xy}^{(0)} \end{Bmatrix} + \begin{bmatrix} B_{11} & B_{12} & B_{16} \\ B_{12} & B_{22} & B_{26} \\ B_{16} & B_{26} & B_{66} \end{bmatrix} \begin{Bmatrix} \varepsilon_{xx}^{(1)} \\ \varepsilon_{yy}^{(1)} \\ \gamma_{xy}^{(1)} \end{Bmatrix}, \tag{2.26}$$

$$\begin{Bmatrix} M_{xx} \\ M_{yy} \\ M_{xy} \end{Bmatrix} = \begin{bmatrix} B_{11} & B_{12} & B_{16} \\ B_{12} & B_{22} & B_{26} \\ B_{16} & B_{26} & B_{66} \end{bmatrix} \begin{Bmatrix} \varepsilon_{xx}^{(0)} \\ \varepsilon_{yy}^{(0)} \\ \gamma_{xy}^{(0)} \end{Bmatrix} + \begin{bmatrix} D_{11} & D_{12} & D_{16} \\ D_{12} & D_{22} & D_{26} \\ D_{16} & D_{26} & D_{66} \end{bmatrix} \begin{Bmatrix} \varepsilon_{xx}^{(1)} \\ \varepsilon_{yy}^{(1)} \\ \gamma_{xy}^{(1)} \end{Bmatrix}, \tag{2.27}$$

where $(\varepsilon_{xx}^{(0)},\varepsilon_{yy}^{(0)},\gamma_{xy}^{(0)})$ are the membrane strains and $(\varepsilon_{xx}^{(1)},\varepsilon_{yy}^{(1)},\gamma_{xy}^{(1)})$ are the bending strains. The extensional stiffnesses A_{ij}, the bending-extensional coupling stiffnesses B_{ij} and the bending stiffnesses D_{ij} are defined in terms of the $k-$th lamina stiffness matrix $\overline{Q}^{(k)}$ (Eq. 2.23), as follows,

$$A_{ij} = \sum_{k=1}^{N} \overline{Q}_{ij}^{(k)} (h_k - h_{k-1}), \tag{2.28a}$$

$$B_{ij} = \frac{1}{2} \sum_{k=1}^{N} \overline{Q}_{ij}^{(k)} (h_k^2 - h_{k-1}^2), \tag{2.28b}$$

$$D_{ij} = \frac{1}{3} \sum_{k=1}^{N} \overline{Q}_{ij}^{(k)} (h_k^3 - h_{k-1}^3), \tag{2.28c}$$

with the $k-$th lamina oriented at an angle θ_k to the laminate coordinate x and located between the points h_{k-1} and h_{k+1}, N denotes to the total number of laminae in the laminate (see Fig. 2.3).

Once established the constitutive equations of the laminate, the laminate equivalent single layer properties can be computed. Treating laminates as equivalent single layer materials may prove to be very valuable for the design

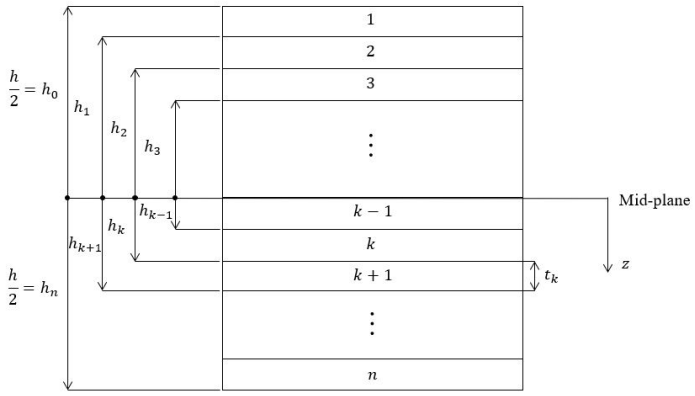

Figure 2.3: Laminate ply numbering.

of composite laminates, since it allows a direct comparison of different materials. From Eqs. 2.28, the membrane and bending properties of the laminate can be derived:

$$E_{xx}^{(m)} = \frac{A_{11} \cdot A_{22} - A_{12}^2}{t \cdot A_{22}}, \tag{2.29a}$$

$$E_{yy}^{(m)} = \frac{A_{11} \cdot A_{22} - A_{12}^2}{t \cdot A_{11}}, \tag{2.29b}$$

$$G_{xy}^{(m)} = \frac{A_{66}}{t}, \tag{2.29c}$$

$$\nu_{xy}^{(m)} = -\frac{A_{12}}{A_{22}}, \tag{2.29d}$$

$$\nu_{yx}^{(m)} = -\frac{A_{12}}{A_{11}}, \tag{2.29e}$$

$$E_{xx}^{(b)} = 12\frac{D_{11} \cdot D_{22} - D_{12}^2}{t^3 \cdot D_{22}}, \tag{2.30a}$$

$$E_{yy}^{(b)} = 12\frac{D_{11} \cdot D_{22} - D_{12}^2}{t^3 \cdot D_{11}}, \tag{2.30b}$$

$$G_{xy}^{(b)} = 12\frac{D_{66}}{t^3}, \tag{2.30c}$$

$$\nu_{xy}^{(b)} = -\frac{D_{12}}{D_{22}}, \tag{2.30d}$$

$$\nu_{yx}^{(b)} = -\frac{D_{12}}{D_{11}}, \tag{2.30e}$$

where m and b refer to the membrane and bending properties and t to the total laminate thickness.

With respect to the equivalent single layer thermal conductivity properties, an electrical analogy is performed. The laminate thermal conductivity tensor components may be obtained by applying a model of parallel and serial

thermal resistances to the in-plane and transverse thermal conductivities [74], as follows

$$K_{xx} = \frac{1}{\sum_{i=1}^{N} t_i} \sum_{i=1}^{N} (k_{xx} \cdot t)_i, \tag{2.31a}$$

$$K_{yy} = \frac{1}{\sum_{i=1}^{N} t_i} \sum_{i=1}^{N} (k_{yy} \cdot t)_i, \tag{2.31b}$$

$$K_{zz} = \frac{\sum_{i=1}^{N} t_i}{\sum_{i=1}^{N} \frac{t_i}{(k_{zz} \cdot t)_i}}, \tag{2.31c}$$

where the subscript i denotes to each lamina and t_i to the $i-$th lamina thickness.

In engineering structures it is usual to incorporate other materials, like metals, within the laminates thus creating hybrid composite laminates. Sheets, meshes and honeycomb cores are some of the possibilities when it comes to adding non-composite layers to a composite, in order to obtain the final properties sought.

Regarding the constitutive equations and equivalent single layer properties for hybrid laminates, the same procedures previously described are followed by adding a new layer with the non-composite material properties.

2.2 Design Methodology

This section is devoted to presenting the methodology used to design and select the laminated composite materials to be analysed. As stated in Sec. 1.4, an objective of this master thesis is to understand whether an optimized structural and thermal solution using composite materials can be auspicious. Therefore, an iterative process, in which each optimization step is characterized by a change in one of the parameters influencing the structural and/or thermal performance of the composite laminate is required. This process will be followed throughout this thesis and it can be subdivided into two main parts: the preliminary selection approach and the optimization cycle.

Fig. 2.4 (a) shows the preliminary selection approach process, which main goal is to select the most promising laminated composite materials among several stacking schemes and lamina materials, thus narrowing the number of laminates to be optimized. The starting point of this process is two unidirectional fibre reinforced polymer composites, CFRP composite and GFRP composite. For each composite material a $n-$th composite laminate is built, in which laminae of aluminium, copper mesh or pyrolytic graphite are added to increase thermal conductivity of the laminate. Once defined the n laminated composite materials, a decision matrix to select the three most suitable laminates is evaluated. Finally, structural, modal and thermal analyses are performed in each of the selected laminates and the optimization cycle is carried out. These analyses are performed using a Finite Element Method (FEM), further explored in chapters 3 and 4. In Sec. 2.2.1 a thorough explanation on the preliminary selection approach process is exposed.

The optimization cycle, presented in Fig. 2.4 (b), consists of an assessment of the resulting design performance, via linear static, modal and static thermal analysis: if judged accurate, the optimization cycle is dismissed, otherwise the material configuration and design are revised (in Fig. 2.4 (b) the sequential requirement assessments are represented by D1, D2 and D3). Chaps. 3 and 4 are dedicated to the structural and thermal optimization design cycle.

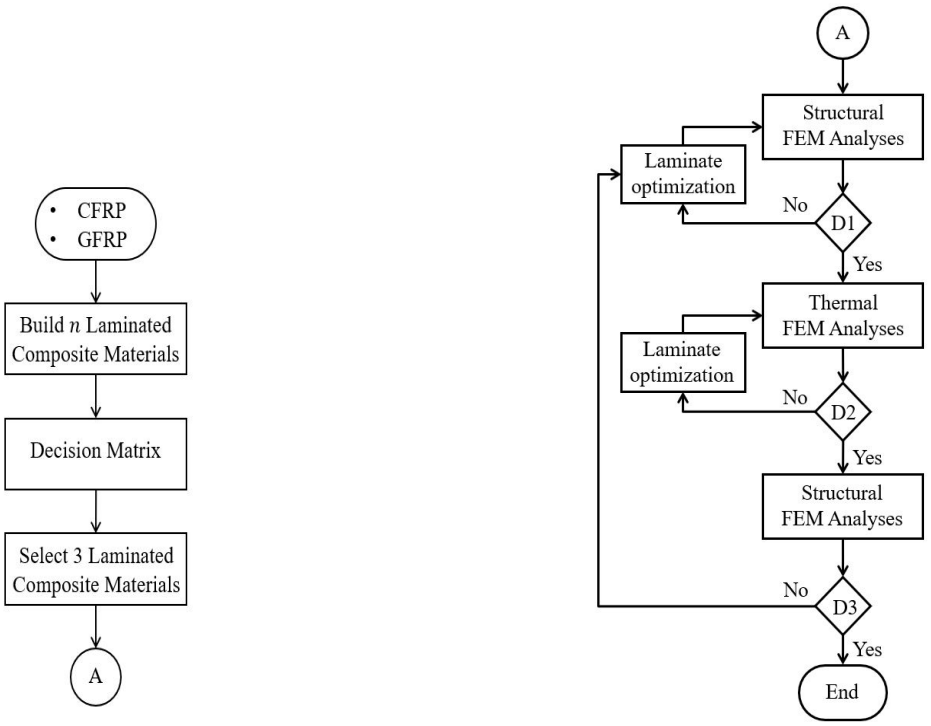

(a) Preliminary selection approach.

(b) Optimization design cycle.

Figure 2.4: Laminated composite materials' design methodology.

2.2.1 Preliminary Selection Approach

The preliminary selection approach begins with the requirements definition. These requirements must be clearly defined, as well as the method of validation, since they lead and narrow down the choices made along the design path, and, ultimately, the validation defines the best candidate selection.

In the present work there are three main requirements, translated in corresponding categories: mass, structural and thermal.

The mass requirement was an obvious demand, given the main objective of this thesis is to assess the possibility of using composite materials to decrease the structural mass of a 3U CubeSat. The reduction of such mass allows to increase the mass budget to be used in other parts of the satellite, enabling the possibility to select different components and/or add additional payloads to the satellite. Furthermore, mass requirements are always a concern when dealing with satellites, as it directly defines the launch costs.

Additionally, the structural and thermal requirements are essential to any satellite. Hence, simulations to emulate the launch and orbit environments, presented in Sec. 1.1.1, must be performed. These simulations allow the validation of the materials being analysed. In Chaps. 3 and 4, the structural and thermal requirements definition and the simulations performed are presented. Since composite materials may present delamination issues that need to be prevented, as explained in Sec. 2.1.2, high thermal conductivity laminates are a requisite as well.

As intended in this work, the rectangular multi-layered plates designed to compare with an aluminium 6061-T6 isotropic plate of 2 mm thickness are here presented. A set of results considering composite laminates, hybrid laminates and fibre metal laminates with different side-to-thickness ratios were considered. Each of the stacking

sequences studied are made of either unidirectional orthotropic CFRP or GFRP composites. Therefore, for each of the stacking sequences presented next, two plates are designed. The plates dimensions are $b \times h \times t = 83 \times 314.51 \times t$, where b, h and t are the plate width, length and thickness, respectively. Namely, 18 distinct plates are studied, which are made of orthotropic and/or isotropic layers, as follows:

A. Symmetric composite laminates - Four-layer composite laminates made of orthotropic fibre reinforced polymer (FRP) composites with a symmetric lamination scheme ($0^o/90^o/90^o/0^o$) of equal thickness layers. Total thickness of 2 mm;

B. Symmetric hybrid laminates - Five-layer composite laminates made of four orthotropic FRP layers with equal thickness along with a core of another material. The hybrid composite laminates lamination scheme is then ($0^o/90^o$/Core/$90^o/0^o$). The core materials utilized were:

   B1. Isotropic aluminium layer with 0.15 mm thickness;

   B2. Copper mesh with 0.25 mm thickness,

   B3. Pyrolytic graphite with 0.1 mm thickness;

   each with:

   a) Total thickness of 2 mm;

   b) Total thickness of 0.75 mm, 0.85 mm and 0.7 mm, respectively, i.e each FRP 0.15 mm thick.

C. Symmetric fibre metal laminates - Multilayer laminate made of isotropic aluminium layers together with orthotropic FRP composite layers. The FML consists of three layer of aluminium, each with 0.15 mm, and bonded in-between each two, two layers of FRP, with 0.15 mm thickness. The lamination scheme and total thickness is then (Al/$0^o/90^o$/Al/$90^o/0^o$/Al) and 1.05 mm, respectively;

D. Symmetric fibre metal laminates without central layer - Six-layer composite laminates made of four orthotropic FRP layers with 0.15 mm thickness each along with two sheets of aluminium as the top and bottom layers with 0.15 mm. The lamination scheme and total thickness is then (Al/$0^o/90^o/90^o/0^o$/Al) and 0.9 mm, respectively.

In order to simplify the different stacks identification, a number was assigned to each of the plates design according to Tab. 2.1.

Note that for an entirely CFRP or GFRP composite plates to have an identical thermal conductivity as the one of aluminium, the total thickness of the composite had to be equal to 16 mm or 448 mm. In the case of a CubeSat, it would be impossible to even consider their use, since the maximum thickness allowed for its side plates is 6.5 mm, according to the CubeSat Design Specifications [77]. As mentioned in Sec. 2.1.2, low thermal gradients are sought to avoid delamination issues. Therefore, hybrid composite laminates were considered for the present work, in an attempt to increase the thermal conductivity of such laminates.

Tab. 2.2 outlines the mechanical and thermal properties considered for each material. Typical values were adopted for all material properties, however, due to the impossibility to determine some of the properties, the following assumptions and computations had to be made.

Table 2.1: Laminates' identification by numerical correspondence.

Laminate #	Case	Main material	Total thickness [mm]	Lamination scheme	Core material
Aluminium design	[-]	Aluminium 6061 T6	2.00	[-]	[-]
1	A.		2.00	(0º/90º/90º/0º)	[-]
2	B1.a)		2.00	(0º/90º/Core/90º/0º)	Aluminium ($t = 0.15$ mm)
3	B1.b)		0.75	(0º/90º/Core/90º/0º)	Aluminium ($t = 0.15$ mm)
4	B2.a)		2.00	(0º/90º/Core/90º/0º)	Copper mesh ($t = 0.25$ mm)
5	B2.b)	CFRP	0.85	(0º/90º/Core/90º/0º)	Copper mesh ($t = 0.25$ mm)
6	B3.a)		2.00	(0º/90º/Core/90º/0º)	Pyrolytic graphite ($t = 0.10$ mm)
7	B3.b)		0.70	(0º/90º/Core/90º/0º)	Pyrolytic graphite ($t = 0.10$ mm)
8	C.		1.05	(Al/0º/90º/Al/90º/0º/Al)	[-]
9	D.		0.90	(Al/0º/90º/90º/0º/Al)	[-]
10	A.		2.00	(0º/90º/90º/0º)	[-]
11	B1.a)		2.00	(0º/90º/Core/90º/0º)	Aluminium ($t = 0.15$ mm)
12	B1.b)		0.75	(0º/90º/Core/90º/0º)	Aluminium ($t = 0.15$ mm)
13	B2.a)		2.00	(0º/90º/Core/90º/0º)	Copper mesh ($t = 0.25$ mm)
14	B2.b)	GFRP	0.85	(0º/90º/Core/90º/0º)	Copper mesh ($t = 0.25$ mm)
15	B3.a)		2.00	(0º/90º/Core/90º/0º)	Pyrolytic graphite ($t = 0.10$ mm)
16	B3.b)		0.70	(0º/90º/Core/90º/0º)	Pyrolytic graphite ($t = 0.10$ mm)
17	C.		1.05	(Al/0º/90º/Al/90º/0º/Al)	[-]
18	D.		0.90	(Al/0º/90º/90º/0º/Al)	[-]

Regarding the copper mesh, based on a market study, a nominal aperture (space between adjacent parallel wires) of 0.14 mm and a total thickness of 0.25 mm was considered. The mass per unit area of a wire mesh is computed, according to the international standard for industrial woven wire meshes, ISO 9044 [78], by

$$m_A = \frac{D^2 \rho}{618.1 \cdot (W + D)}, \tag{2.32}$$

where D is the wire diameter in millimetres, ρ the density of the wire material in $\mathrm{kg} \cdot \mathrm{m}^{-3}$ and W the mesh nominal aperture in mm. Then, mass density can be simply found by $\rho_{mesh} = m_A / t_{mesh}$, where t_{mesh} is the mesh's thickness.

The effective thermal conductivity of wire meshes is strongly influenced by the contact conditions between the wires, the individual layers and by the mesh's geometric parameters, as the wire diameter. Several analytical models were developed throughout the years, which can be categorized in two main groups: high effective thermal conductivity predictions and low effective thermal conductivity predictions. In the present work a conservative approach was selected and, therefore, low effective thermal conductivity models were chosen. Detailed explanations on the thermal models can be found in references [79], [80] and [81].

Moreover, the Young modulus of the copper mesh and pyrolytic graphite were assumed to be negligible when compared with the FRP composite materials.

In order to select the three most promising materials among the 18 plates described previously, a decision matrix was devised. Decision matrices are a common approach when a number of alternative options, with multiple factors, have to be taken into consideration. Typically, different weights are attached to each decision factor (or criteria) and then, by adding the weighted scores, an overall score is obtained. However, a normalization step must be performed prior to the aggregation, since different criteria can have distinct units. Therefore, to select the most suitable options among the several laminated composite materials created, it was decided to use the following procedure:

1. Define the decision factors;

2. Compute the equivalent single layer structural and thermal properties of each laminated composite material;

Table 2.2: Mechanical and thermal properties of the materials used for the side panels.

Property	Units	CFRP [82] [83]	GFRP [82] [83]	Aluminium 6061 T6 [84] [20]	Copper Mesh [85]	Pyrolytic Graphite [86]
E_1	[GPa]	175.0	48.9	68.9	[-]	[-]
E_2=E_3	[GPa]	7.0	5.5	68.9	[-]	[-]
$G_{12} = G_{13}$	[GPa]	3.5	2.5	26	[-]	[-]
G_{23}	[GPa]	1.4	2.0	26	[-]	[-]
$\nu_{12} = \nu_{13}$	[-]	0.25	0.33	0.33	[-]	[-]
ν_{23}	[-]	0.25	0.33	0.33	[-]	[-]
X_T	[MPa]	760	1020	289.6	[-]	20
X_C	[MPa]	690	620	289.6	[-]	20
Y_T	[MPa]	28	40	289.6	[-]	20
Y_C	[MPa]	170	140	289.6	[-]	20
S	[MPa]	70	70	207	[-]	20
k_{11}	[W/(mK)]	40.0	0.929	167	68.18	700
k_{22}	[W/(mK)]	0.70	0.544	167	68.18	700
k_{33}	[W/(mK)]	0.70	0.544	167	16.8	80
α	[-]	0.8 [87]	0.3 [88]	0.14 [89]	[-]	[-]
ε	[-]	0.7 [90]	0.85 [88]	0.84 [89]	[-]	[-]
ρ	[kg/m^3]	1600	1900	2700	3007	850

3. Compute the equivalent single layer properties taking into account the materials' thickness;

4. Normalize the composite laminate properties;

5. Compute the weighting average for each material by assigning to each one of the decision factors a weight that reflects their importance;

6. Select the highest results as the finest solutions.

As an implication of the requirements specified in the beginning of the present section, the composite laminate should be lightweight, have good mechanical properties and high thermal conductivity. The resulting decision factors are:

1. Specific mass ρ;

2. Mechanical properties:

   (a) Engineering constants: Equivalent single layer stiffness properties $E_{xx}^{(b)}$, $E_{yy}^{(b)}$ and $G_{xy}^{(b)}$;

   (b) Material's strengths: Shear S and ultimate strength X_T, X_C, Y_T and Y_C of the composite material, where X represents the ultimate strength of the material in the $x-$direction and Y in the $y-$direction, with T and C referring to tensile and compression states, respectively;

3. Thermal Properties: Equivalent single layer thermal conductivity tensor K_{xx}, K_{yy} and K_{zz}.

Note that the membrane properties were not taken into account as a decision factor, since it was assumed laminates behave as plates due to their thickness to length ratio, and considered that the bending forces would have a bigger influence and lead the laminate to failure prior to membrane ones.

In order to make it possible to compare different stacking sequences, the properties have to take the laminates' thickness into account. Therefore, the mass per unit area m_A is used instead of the specific mass and the flexural moments (EI) and torsional stiffness (GJ) instead of the bending properties. I is the moment of inertia of the laminates z-axis and J is the torsional constant of a plate with a rectangular closed section $b \times t$, respectively, given

by [91]

$$I = \frac{bt^3}{12}, \tag{2.33a}$$

$$J = bt^3 \left(\frac{1}{3} - 0.21 \frac{t}{b} \left[1 - \frac{1}{12} \left(\frac{t}{b} \right)^4 \right] \right). \tag{2.33b}$$

The tensile strength, shear strength and thermal conductivities are multiplied by the laminate total thickness t.

Once computed the plates' properties, the normalization has to be performed. There are several normalization methods which can be consulted in reference [92]. In the present work the method chosen was to divide each factor by the correspondent value of a reference material. This causes the reference material values, on each criteria, to equal unity and all others to represent a fraction of those values. This approach was chosen given the core of the present work, being henceforth the 2 mm aluminium plate as the reference material.

Following the normalization of the evaluation criteria, weighting factors have to be assigned. Note that for the decision matrix to be viable, weighting factors must be assigned as objectively as possible to reflect the priority among the different criteria.

In Tab. 2.3, the weight factors assigned are summarized. A $0-1$ system for the weighting factors was established and a two step weight factor assignment adopted.

First, a rate for each individual property within the three categories previously presented - mass, mechanical properties and thermal properties - was defined. A weight factor of 1 was assigned to the mass category, because it is the only criteria in this category. As for the engineering constants and thermal properties a weight factor of $1/3$ was fixed for each criteria and 0.2 assigned for each material strength, given that all the constants were considered to have an identical role in the definition of the mechanical and thermal behaviour of the material.

The second step consists in the assignment of a weight factor for each category. Weights of 0.4, 0.3 (0.15 for engineering constants and 0.15 for the material's strengths), and 0.3 were established for the specific mass, mechanical properties and thermal conductivity, respectively. Since the main objective of this project is to decrease the structural mass, materials with the lowest specific mass are preferred and, therefore, a higher weight was established for this parameter. As for the mechanical and thermal categories, given that the final material desired must endure the mechanical and thermal environments an equal factor of 0.3 was fixed for both.

Table 2.3: Laminated composite materials' weighting factors.

Category		Criteria	Criteria rating	Category weight
Mass		m_A	1	0.40
Mechanical properties	Engineering constants	$E_{xx}I$	1/3	0.15
		$E_{yy}I$	1/3	
		$G_{xy}J$	1/3	
	Material's strengths	X_Tt	0.2	0.15
		X_Ct	0.20	
		Y_Tt	0.20	
		Y_Ct	0.20	
		St	0.20	
Thermal properties		$K_{xx}t$	1/3	0.3
		K_{yy}t	1/3	
		K_{zz}t	1/3	

Subsequently, the decision matrix is computed. In Tab. 2.4, the matrix is presented, in which the normalization values for each laminate can be found. As can be seen, the materials with the three highest scores (by descending order) are the following composite laminates:

1. Number 7: CFRP with pyrolytic graphite core and total thickness of 0.7 mm;
2. Number 16: GFRP with pyrolytic graphite core and total thickness of 0.7 mm;
3. Number 3: CFRP with aluminium core and total thickness of 0.75 mm;

These hybrid laminates are the ones selected to enter the structural optimization cycle, which results are presented in Sec. 3.

In Appendix B in Tab. 2.2, the mechanical and thermal properties of each plate computed using the equations presented in Sec. 2.1.2 can be found.

Table 2.4: Decision matrix.

Laminate #	Mass	Structural properties			Material strength					Thermal properties			
	m_A	$E_{xx}I$	$E_{yy}I$	$G_{xy}J$	$X_T t$	$X_C t$	$Y_T t$	$Y_C t$	St	$K_{xx}t$	$K_{yy}t$	$K_{zz}t$	Total
Aluminium design	1.000	1.000	1.000	1.000	1.000	1.000	1.000	1.000	1.000	1.000	1.000	1.000	1.000
1	1.688	2.239	0.407	0.135	2.624	2.383	0.097	0.587	0.338	0.122	0.122	0.004	1.020
2	1.605	2.166	0.481	0.135	1.000	1.000	0.097	0.587	0.338	0.188	0.188	0.005	0.910
3	3.956	0.107	0.033	0.008	0.375	0.375	0.036	0.220	0.127	0.112	0.112	0.002	1.646
4	1.520	2.110	0.532	0.134	2.624	2.383	0.097	0.587	0.338	0.158	0.158	0.005	0.960
5	3.155	0.144	0.054	0.010	1.115	1.013	0.041	0.249	0.144	0.088	0.088	0.002	1.367
6	1.728	2.191	0.455	0.135	0.069	0.069	0.069	0.069	0.097	0.325	0.325	0.004	0.907
7	5.167	0.090	0.024	0.006	0.024	0.024	0.024	0.024	0.034	0.246	0.246	0.002	2.126
8	2.483	0.201	0.130	0.100	0.525	0.525	0.051	0.308	0.178	0.262	0.262	0.004	1.115
9	3.051	0.125	0.078	0.068	0.450	0.450	0.044	0.264	0.152	0.187	0.187	0.003	1.312
10	1.421	0.634	0.159	0.096	3.522	2.141	0.138	0.483	0.338	0.004	0.004	0.003	0.813
11	1.378	0.616	0.179	0.097	1.000	1.000	0.138	0.483	0.338	0.079	0.079	0.004	0.701
12	3.495	0.031	0.012	0.006	0.375	0.375	0.052	0.181	0.127	0.076	0.076	0.002	1.449
13	1.325	0.601	0.192	0.096	3.522	2.141	0.138	0.483	0.338	0.055	0.055	0.004	0.784
14	2.854	0.042	0.018	0.007	1.497	0.910	0.059	0.205	0.144	0.052	0.052	0.002	1.240
15	1.461	0.622	0.172	0.096	0.069	0.069	0.069	0.069	0.097	0.214	0.214	0.003	0.683
16	4.408	0.026	0.008	0.004	0.024	0.024	0.024	0.024	0.034	0.211	0.211	0.001	1.811
17	2.293	0.123	0.105	0.098	0.525	0.525	0.073	0.254	0.178	0.226	0.226	0.003	1.026
18	2.769	0.081	0.070	0.067	0.450	0.450	0.062	0.218	0.152	0.151	0.151	0.002	1.189

Chapter 3

Structural Analysis

Following the establishment of the composite materials to be studied as an alternative for the aluminium side panels of a 3U CubeSat, the current chapter aims to present the structural analysis to be performed in a putative CEiiA's satellite. Linear static and normal mode analysis will be the focus of this chapter.

In Sec. 3.1, a brief overview of the theoretical background required to understand the analysis performed is presented. First, the structural requirements that must be fulfilled by the spacecraft are exposed and, then, the FEM is introduced, along with some of its concepts, such as elements and nodes. The hierarchic steps to perform any finite element analysis (FEA) are briefly described, namely the pre-processing, solution and post-processing. Finally, the failure criteria used in the present work for isotropic and composite materials are exposed: the von Mises theory and the Tsai-Hill failure criteria.

In order to perform the linear static and the modal analysis on the satellite, it is necessary to create the FEM model of the structure. Therefore, in Sec. 3.2, the FEM model creation is thoroughly explained, namely information about the structure's idealization, boundary conditions and loads applied to the model, and meshing process.

Sec. 3.3 presents the structural results obtained for the several designs under studied and the optimizations made to the laminated composite materials.

Since the structure to be analysed is a spacecraft intended to work in the space environment, the standards and handbooks developed by the ECSS were followed through this chapter. Among the several standards and handbooks consulted are references [14, 93, 94, 95].

This chapter is not meant to provide an exhaustive review on the analysis methods and finite element theory, and so only the fundamental topics to understand the numerical analysis performed in the current work are discussed. The books by Reddy [96], Hutton and Wu [97] and Heckbert [98] may be consulted for a complete review on these topics.

3.1 Theoretical Background

3.1.1 Structural Requirements

According to the ECSS, satellite structures shall be designed to withstand the worst conditions predicted without compromising their structural integrity, thus allowing the mission to which it was designed to be successfully conducted [14]. As seen in Sec. 1.1.1, the most structural demanding loads occur during launch in the life-cycle of satellites and therefore, the requirements are directly related to the environment which the satellite is subjected to while being transported into orbit inside the launch vehicle. Hence, the definition of the loads applied to the satellite are determined by the launch vehicle to be used, in the present work by the VEGA launcher.

Regarding the launch static loads, a simple free body diagram can be used to help understanding their distribution. However, first it is necessary to evaluate the typical CubeSat position within the VEGA launcher, since the loads are defined in each of the launcher's axes. According to reference [99], 3U CubeSats are usually laid down horizontally within VEGA and, therefore, the longitudinal loads are applied in the lateral direction of the satellite.

Once identified the axes, the maximum quasi-static accelerations can be applied to the structure as inertial forces, along the various launcher axes [99]:

1. Longitudinal direction: $-14.5g$ and $+10.5g$;
2. Lateral directions: $\pm 3g$,

where g is the Earth's gravitational acceleration.

In Fig. 3.1, the static loads free body diagram is shown. A correspondence between the launcher (VEGA) and the satellite's (3U) coordinate systems is also depicted.

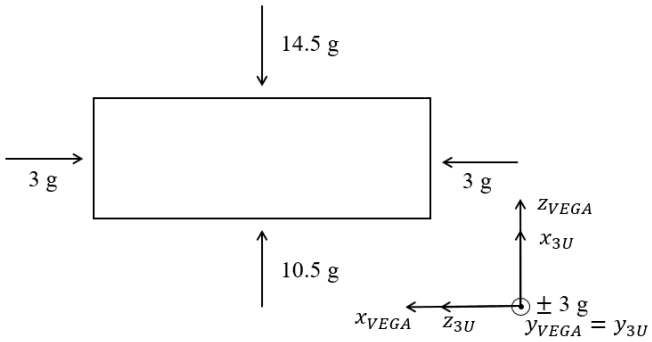

Figure 3.1: Linear static analysis loads (free body diagram).

Note that in linear static FEM analyses, which will be discussed in more detail in Sec. 3.1.2, each load will be evaluated individually to allow the assessment of the structure behaviour to each load. Therefore, six different case scenarios must be considered for analyses. To simplify the identification of each case, Tab. 3.1 was devised.

In linear static analyses, structures subjected to a certain load environment are designed to allow the maximum stress to be less than its materials strengths by a sufficient margin, known as the margin of safety (MOS), so that unexpected conditions other than those predicted for use in the analysis are accounted for [94]. MOS is also considered due to the assumptions and simplifications inherent to FEM models. Then, in the present work, a

Table 3.1: Linear static case analyses.

Cases	Launcher coordinate system	Satellite coordinate system	Load
A	$z-$direction	$x-$direction	$+10.5g$
B	$z-$direction	$x-$direction	$-14.5g$
C	$y-$direction	$y-$direction	$+3.00g$
D	$y-$direction	$y-$direction	$-3.00g$
E	$x-$direction	$z-$direction	$+3.00g$
F	$x-$direction	$z-$direction	$-3.00g$

structure is considered not to fail if its MOS is greater than zero [94]. For isotropic materials, the MOS can be computed as [95]

$$\text{MOS} = \frac{\sigma_{allowable}}{\sigma_{result} \times \text{FOS}} - 1, \tag{3.1}$$

where the $\sigma_{allowable}$ corresponds to the yield or ultimate strength of a given material, FOS is the factor of safety and σ_{result} corresponds to the analysis stresses obtained taking into account several design factors.

In the case of spaceflight hardware, standards as the ones created by ECSS state which values of design factors and FOS must be accounted for in the analysis and are applied to achieve the structures standard reliability objectives [94].

According to reference [94], the design factors to be taken into consideration for satellites are: the model factor, to account for uncertainties in the mathematical model (with a typical value of 1.2); the project factor, to reflect the maturity of the program and the confidence in the specifications given to the project (being 1 usually applied to final developing states); and the qualification factor, that is applied to the specified loads (a value of 1.25 is used for satellites on the basis of global flight loads).

Regarding the FOS, its value can correspond to a yield design factor of safety (FOSY) or to an ultimate design factor of safety (FOSU) value, depending if the yield or the ultimate strength of the material is taken as the $\sigma_{allowable}$. In Tab. 3.2, the FOSs considered regarding metallic and fibre reinforced polymer structures are presented [94].

Table 3.2: FOS for verification by analysis only regarding metallic and FRP satellite's structural parts.

Materials	FOSY	FOSU
Metals	1.25	2
FRP	[−]	2

Regarding the dynamic behaviour of space structures, to prevent structural damage or failure, the fundamental frequency of the structure must be higher than those induced by the launch, which are directly related to the launch vehicle fundamental frequency. This frequency is then defined as the modal requirement and is established by the launch vehicle supplier and encountered in the respective manual [14].

As stated before, the launch vehicle to be considered is VEGA, therefore, according to reference [99], 3U CubeSats must present a fundamental frequency higher than 115 Hz. Although this requirement can be relaxed to 90 Hz [99], a conservative approach is used in this work, so the 115 Hz requirement is maintained to prevent resonance.

To ensure that the satellite will meet all the structural requirements, its behaviour must the predicted, thus the

need to perform FEM analyses.

3.1.2 Finite Element Method

Essentially, the FEM seeks to approximate the behaviour of a structure under general loads and boundary conditions by means of a discretization process, i.e. with an assembly of simpler finite subdomains - the finite elements or simply called elements. Each element is connected to its neighbouring elements at the grid points (nodes). The group of elements and nodes is called the mesh.

The process of applying a FEM can be clearly divided into three stages [65]:

1. Pre-Processing - The problem definition is established and the FEM model created. The domain of the analysis is defined, the initial structures are simplified and the elements to be used are chosen. Then, the mesh can be created and the problem becomes discretized. The material properties are applied to each element and the loads and boundary conditions defined by the problem are applied to the FEM model.

2. Solution - The process that takes the formulation of the analysis' governing equations and leads to the definition of the element matrices. Based on these matrices, the collective behaviour of the structure's elements is defined and the global matrix equation can be found. Consequently, a particular solution for the primary variables is obtained;

3. Post-Processing - The results and outputs desired are computed at this stage. According to the analysis, the data is processed and the results presented in any number of forms, as graphics, images and charts.

Note that the finite element method will solve only the selected mathematical model (FEM model) and all its assumptions will be reflected in the solution. Thus, an insight on the problem being analysed is required and caution with the assumptions made is also essential.

Several types of analysis can be performed using FEM and the governing equations that hold for each specific analysis vary. The governing equations dictate the space and/or time and/or frequency dependent variation of a particular quantity, such as displacement, heat and electromagnetic fields. Additionally, the boundary conditions also differ, allowing the full definition of the problem to be studied and therefore, fully characterizing it [65]. Therefore, depending on the type of variation with time and/or frequency, analysis can be classified into [100]:

1. Static analysis: Predicts the distribution of loads resulting from applied loads, either structural or thermal, which do not vary (static loads) or slowly vary with time (quasi-static loads). Subjecting a structure to non-varying load causes changes that eventually converge and it is said that the structure reaches a steady state.

2. Dynamic analysis: Used to predict the response of a structure under time or frequency-varying loads, which responses will also be time or frequency dependent. Among the types of dynamic analysis that can be performed, there are the free vibrations (also known as normal mode analysis), the frequency response and the transient response analysis.

In the present work, only linear static analysis, normal mode analysis and static thermal analysis will be performed. The remaining analyses will not be further explored and additional information regarding them can be

found in references [65] and [101]. The general equations regarding the structural analysis (linear static analysis and normal mode analysis) conducted are succinctly presented next. Chapter 4 deals with the thermal analysis.

Linear Static Analysis

Several assumptions have to be made in order to perform a linear static analysis, which, when violated, can lead to results that appear credible but do not represent the structures' real behaviour. The linear static analysis assumptions are summarized as follows [100]:

1. Hooke's law is obeyed by the materials, i.e. all materials are considered to have a linear elastic behaviour;
2. Displacements are considered to be small;
3. Applied loads are either independent of time or vary slowly, which, as explained previously, do not induce dynamic behaviour.

The general equation to be solved in linear static analysis, which dictates the space variations of displacement in a structure under the influence of applied forces, is given by [100] [102]

$$\left[K\right]\left\{u\right\} = \left[F\right], \tag{3.2}$$

where K is the system stiffness matrix, u the grid point displacements and F the applied force vector.

Using Eq. 3.2, the displacements at the grid points can be discovered and, consequently, the desired outputs, as strains, stresses and forces, computed on an element-by-element basis.

Therefore, by performing a linear static analysis it is possible to identify the points in the structure subjected to loads that can lead to structure failure.

Normal Mode Analysis

Normal mode analysis is used to compute the natural undamped mode shapes and associated natural undamped frequencies of a structure.

The motion equations of a multi-degree of freedom system of a normal mode analysis can be represented in the matrix form as follows [103] [102],

$$\left[M\right]\left\{\ddot{u}\right\} + \left[K\right]\left\{u\right\} = 0, \tag{3.3}$$

where $[M]$ is the mass matrix, $[K]$ the stiffness matrix, u the grid point displacements and $\ddot{u}$ the grid point accelerations. To find the free vibration responses of a system, Eq. 3.3 is reduced to a eigenvalue problem [102], in which, for each degree of freedom i of a system, a non-trivial solution of the eigenvalue problem can be encountered:

$$\left(\left[K\right] - \omega_i^2\left[M\right]\right)\left\{\phi_i\right\} = 0, \tag{3.4}$$

where ω_i is the i-th natural frequency of the system and ϕ_i is its corresponding mode shape. The first of those frequencies is called fundamental frequency.

Modal analyses are essential in any preliminary design stages, since it enables the identification of the frequencies which the structure cannot function at, or else it can go into resonance condition, leading to failure.

Regarding the mode shapes it is important to note that they are intended to give information only about the shape of each natural frequency vibration mode and not about the amplitude of that vibration, which depends not only on the natural frequency but also on the applied loads. Hence, the results obtained from this analysis correspond only to a relative displacement, giving an idea of the shape that should be expected when a structure is vibrating in a specific natural frequency [102].

As a preliminary approach, Rayleigh equation is often used to predict the natural frequencies expected for a given structure. Assuming that the mass $[M]$ and stiffness $[K]$ matrices are symmetric and real, Rayleigh's equation can be obtained [102],

$$\omega_i^2 = \frac{{\phi_i}^T [K] \phi_i}{{\phi_i}^T [M] \phi_i}. \tag{3.5}$$

It can be directly concluded from Eq. 3.5 that the natural frequencies of a stiffer and lighter structure are expected to be higher than those of a less stiff and heavier equivalent structure.

As outlined, depending on the nature of the FEM analysis, different outputs are obtained. In the case of the normal mode analysis, the result obtained can be directly compared with the frequency requirement established. However, concerning the linear static analysis, to determine the stress resulting from the load environment failure theories must be considered.

3.1.3 Failure Theories

The failure theories predict when the structure will reach its elastic limit (yield point) or when it will fracture under a specific state of stress, either of which can define the structure failure. The magnitude of stress at which these events may occur are inherent properties of the material's yield and ultimate strength [104].

Note that the definition of failure can differ for different designs or analyses depending on the failure criteria chosen. There is no universal theory to predict these events for the general case of materials and stress state. Instead several theories have been formulated.

In the present work, the distortion-energy theory, better known as the von Mises theory, is used as the failure theory for isotropic structures and the Tsai-Hill theory used for composite materials. From state-of-the-art studies, these theories are among the most commonly used to asses the state of stress of structures. All other existing theories will not be presented in this thesis. For further information regarding failure theories the books by Shigley [105], Kaw [67] and Altenbach et al. [32] may be consulted.

Von Mises Theory

The von Mises theory states that a material is considered to fail if [105]

$$\sigma' = \left[\frac{(\sigma_1 - \sigma_2)^2 + (\sigma_2 - \sigma_3)^2 + (\sigma_3 - \sigma_1)^2}{2} \right]^{1/2} \geq \mathrm{T}_Y, \tag{3.6}$$

where σ' is the von Mises stress, σ_1, σ_2 and σ_3 are the stresses in the corresponding three dimensional axis and T_Y is the material's yield strength.

The von Mises stress can be thought of as an equivalent or effective stress for the entire general state of stress given by σ_1, σ_2 and σ_3. Therefore, when there are multiple components of stress that must be accounted for, von Mises theory becomes utterly useful, allowing the multiple stresses to be reduced to a single value that can be compared to the yield strength of a material through Eq. 3.6.

For plane stress, the von Mises criteria is usually represented in its principal directions, which are those that maximize the normal stresses and minimize the shear ones, σ_A and σ_B. These normal stresses are designed as the principal stresses, given by in a *xyz*-coordinate system as [106],

$$\left.\begin{matrix}\sigma_A \\ \sigma_B\end{matrix}\right\} = \frac{\sigma_x + \sigma_y}{2} \pm \sqrt{\left(\frac{\sigma_x - \sigma_y}{2}\right)^2 + \tau_{xy}^2} \tag{3.7}$$

For a thorough explanation on principal directions and stresses consult references [106] and [105].

From Eqs. 3.6 and 3.7, von Mises criteria can be simply given as [106]

$$\sigma' = \left[\sigma_x^2 - \sigma_x\sigma_y + \sigma_y^2 + 3\tau_{xy}^2\right]^{1/2} \geq T_Y. \tag{3.8}$$

One final note concerns the material's shear yield strength, that according to the von Mises theory can be computed as a function of the material strength T_y, as follows [105]

$$S_y = 0.577 T_Y. \tag{3.9}$$

Note that in linear static analysis the materials are assumed to be in the linear elastic region, obeying Hooke's law, as stated in Sec. 3.1.2. Therefore, it is industry practice to use von Mises criteria not only to compare the state of stress to the yield strength of a material, but also to its ultimate strength when static analyses are being performed.

Tsai-Hill Theory

The Tsai-Hill theory, like the von Mises criteria, considers the interactions among the different stress parameters, thus allowing for a single index to characterize the probability of a lamina to fail. However, in its basic form it does not distinguish between the compressive and tensile strengths in its equations, resulting in an underestimation of the maximum loads which can be applied to the composite when compared with other failure theories. Hence, a modification to account for corresponding tensile or compressive strengths is required. According to the modified Tsai-Hill failure theory, a laminated composite material is said to fail if [67]

$$\left(\frac{\sigma_1}{X_1}\right)^2 - \left(\frac{\sigma_1\sigma_2}{X_2^2}\right) + \left(\frac{\sigma_2}{Y}\right)^2 + \left(\frac{\tau_{12}}{S}\right)^2 \geq 1, \tag{3.10}$$

with

$$X_1 = \begin{cases} \sigma_1^{T_U} & \text{if } \sigma_1 > 0 \\ \sigma_1^{C_U} & \text{if } \sigma_1 < 0; \end{cases} \tag{3.11a}$$

$$X_2 = \begin{cases} \sigma_1^{T_U} & \text{if } \sigma_2 > 0 \\ \sigma_1^{C_U} & \text{if } \sigma_2 < 0; \end{cases} \tag{3.11b}$$

$$Y = \begin{cases} \sigma_2^{T_U} & \text{if } \sigma_2 > 0 \\ \sigma_2^{C_U} & \text{if } \sigma_2 < 0; \end{cases} \tag{3.11c}$$

$$S = \tau_{12}^{U}, \tag{3.11d}$$

where T and C correspond to the tensile and compression states, and U refers to ultimate strength values.

As can be concluded from Eq. 3.10, a lamina is said to fail if its failure index is equal or higher than one. As for the laminate, it may be considered to fail when the failure criteria of one of its laminae is reached, known as first-ply failure. Although the fracture of a single layer does not necessarily lead to a total failure of the composite.

Failure index can be seen as an analogous margin of safety for composite materials. In order to account for the factor of safety presented in Tab. 3.2 when using composite materials, the ultimate loads (loads $\times$ FOSU) are used as inputs for the analysis at stake.

3.2 Finite Element Model

As stated before the numerical method applied in this dissertation is the FEM, which follows three basic hierarchic steps: pre-processing, solution and post-processing. The software used in each of the steps are Altair HyperMesh, the finite element software MSC Nastran and the Altair HyperView as the post-processing one.

This section is devoted to the pre-processing stage, which deals with the creation of the mathematical model, known as the FEM model. The pre-processing step consists, also, on three hierarchic steps regardless of the analysis at hand: the part idealization, element properties definition and the boundary conditions and load application.

3.2.1 Part Idealization

To simplify the mesh generation process, some details in the satellite geometry can be removed. The structure simplification or idealization reduces the number of elements required to properly mesh small details and allows the creation of more uniform meshes. The simplifications made to the CubeSat CAD model, presented in Sec. 1.3, were:

1. All round edges, chamfers, fillets, holes and small design features were removed;
2. The electronic subsystems and the payload were replaced by each component's centre of gravity, which are then connected to the structure by rigid elements, discussed in more detail in Sec. 3.2.2. All components are assumed to be of uniform density, hence the centre of gravity is, also, the component's centroid;

3. All structures, with the exception of endless screws and bolts, were converted into two dimensional (2D) surfaces, represented by its mid-surfaces. This simplification is considered valid, due to the dimensions of the structures being handled which can be treated as thin plates. A thin plate is one where the thickness is much smaller than its other dimensions, more precisely, with a typical side-to-thickness ratio greater or equal than 100 [76].

4. The endless screws and bolts were converted into one dimensional (1D) structures.

3.2.2 Element Properties

The basic idea of FEM lays in the calculations of several differential equations at a finite number of points called nodes or grid points. These nodes form entities called elements, which in turn form the mesh (a group of elements). The motion associated with each element depends on the degrees of freedom (DOFs), i.e. the components of displacement, associated with each of its nodes. In the structural models there are six possible displacement components: three translations in the $x-$, $y-$ and $z-$direction and three rotations about the $x-$, $y-$ and $z-$axis [100]. Depending on the type of analysis to be performed and on the geometry, size and shape of the structure, several types of elements can be chosen [65]. Once the mesh is created, different features, as the material's mechanical and thermal properties, the structure cross-section or thickness, can be assigned to the elements through the property cards. It must be noted that property cards are an idea specific of the MCS Nastran software. The distinct element types and property cards can be consulted in the MCS Nastran Quick Reference Guide [107].

As explained in Sec. 3.2.1, the structure was simplified and the original CAD is now represented only by 2D, 1D and geometric centres. For each of these structures different types of elements are selected.

Regarding the 2D structures, the CQUAD4 two-dimension elements are used. These elements are planar, hence the software has the width and length data for each, however the third dimension, thickness, must be given by the user as input, through the PSHELL property card. In the case of the side panels, when composite materials are being studied, the PSHELL is replaced by the PCOMP card, since it allows to model n-ply composite laminates as 2D structures [107].

In FEM analysis, concentrated masses are modelled by CONM2 elements. The inputs given to each element correspond to the mass value and moments of inertia (I) of the respective component it represents. The components centroid and moments of inertia can be found in appendix C in Tab. C.1, both values were directly taken from the CAD software.

The concentrated masses are connected to the endless screws and bolts through rigid body elements (RBE2), which are 1D elements used to connect two or more nodes together. In the case of an RBE2, one node serves as the independent and the other(s) as the dependent(s). The connection is a rigid link that transfers motion from the independent node to the dependent(s). The motion that is transferred depends on the DOFs associated with each of those nodes [107].

The bolts and endless screws were modelled as CBAR and CBEAM elements. Since they are 1D elements, the cross-section area of each element must be provided by the user as an input to complete the three dimensions required. Cross-section is then provided through the property cards: PBAR and PBEAM.

Special attention must be given to the cross-section area considered, since bolt threads details are not modelled. According to reference [105], an unthreaded rod having a diameter equal to the mean of the pitch diameter and minor diameter of the threaded rod will have the same tensile strength as the threaded one. The area of the unthreaded rod is then called the tensile-stress area A_t of the threaded rod. The bolts used in the satellite are of type M2 with a nominal major diameter d of 2 mm and pitch p of 0.4 mm [105]. The value of the corresponded tensile-stress, for M type threads, can be computed as follows [95]:

$$A_t = 0.25\pi d_t, \tag{3.12}$$

where d_t is the diameter used for stress calculation given by

$$d_t = 0.5(d_2 + d_3), \tag{3.13}$$

with pitch diameter $d_2 = d - 0.64952p$ and minor diameter $d_3 = d - 1.22687p$ [95]. Therefore, the tensile-stress area for a M2 thread is equal to 2.07 mm^2, being this the input value used for the cross-section areas of the CBAR and CBEAM elements.

In Tab. 3.3, the structure simplifications made to each component, the type of elements used to create the mesh and the property cards and materials assigned to each element are summarized.

Table 3.3: Static and modal FEM model mesh properties.

Structure idealization	Component	Element type	Property card	Material
2D	Rails	CQUAD4	PSHELL	Aluminium 6061 T6
	System supports			Aluminium 6061 T6
	Payload support			Aluminium 6061 T6
	Side panels		PSHELL or PCOMP	Aluminium 6061 T6 or Laminated composite material
1D	Bolts	CBAR	PBAR	Stainless Steel 304
	Endless screws	CBEAM	PBEAM	Stainless Steel 304
	Connections	RBE2	[−]	[−]
Centre of gravity	Antenna Transceiver Power board Power control board Solar panels OBC Magnetorquers board NanoCamera	CONM2	[−]	[−]

Figs. 3.2 (a), (b) and (c) shows the structural FEM model created so far, due to legibility purposes not all elements are identified and three different views are presented.

3.2.3 Boundary Conditions

Hitherto, the FEM model created for the linear static analysis and for the normal mode analysis was the same. However, as explained in Secs. 3.1.2 and 3.1.2, the analysis governing equations are not the same, and therefore, the boundary conditions applied to each model differ.

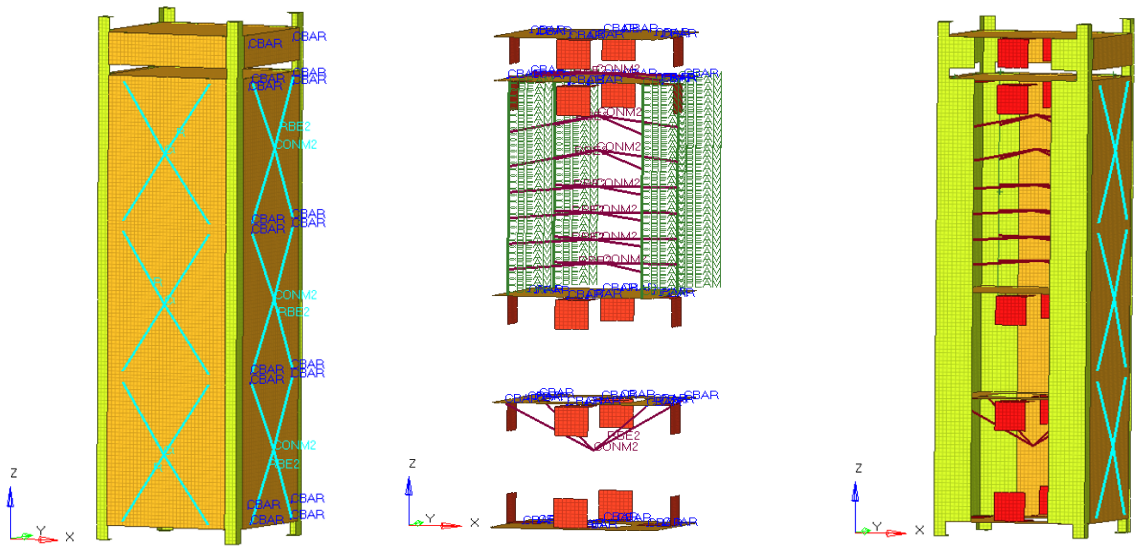

(a) External view. (b) Internal view. (c) External and internal assembly view.

Figure 3.2: External, internal and assembly views of the structural FEM model.

Regarding the linear static FEM model, the six case scenarios presented in Tab. 3.1 were considered and for each the loads were defined as acceleration vectors for gravity loads, using the Acceleration or Gravity loads card (GRAV), applied to each of the axes with the respective magnitude. The design factors were already an intrinsic value, and, therefore, it was not necessary to consider any additional safety factors [99]. Once applied the static loads, the movement constraints must be established. Typically, the satellite rails are the only structure of the satellite in contact with the deployer capsule, therefore the movement in each case was confined to the corresponding perpendicular axes [108] using Single Point Constraints (SPC). In Figs. 3.3 (a) and (b), the SPCs used when the gravitational load was applied in direction 1, which correspond to the $x-$ or $y-$axes of the 3U CubeSat, and direction 3 ($z-$axis of the satellite) are presented, respectively. The same scheme was used for the negative load cases.

As for the modal analysis case, the main objective is to find the natural frequencies and corresponding mode shapes of the satellite, and, therefore, no boundary conditions were applied to the model. Hence, one can say that free vibration conditions were modelled.

3.2.4 Mesh Refinement

In Sec. 3.2.2, the mesh was created, however the elements' size was not specified. Therefore, to determine the density of elements to be used for the final FEM models convergence studies must be performed, given that the quality of the mesh directly influences the results obtained from the analysis and can lead to inaccuracies. Apart from converged results, the computation time to perform each analysis must be evaluated as well, since time constraints are an aspect that ought to be deliberated in this kind of projects. Usually, elements with smaller sizes provide better results at a cost of increased computational times, thus simple FEM models are created and then

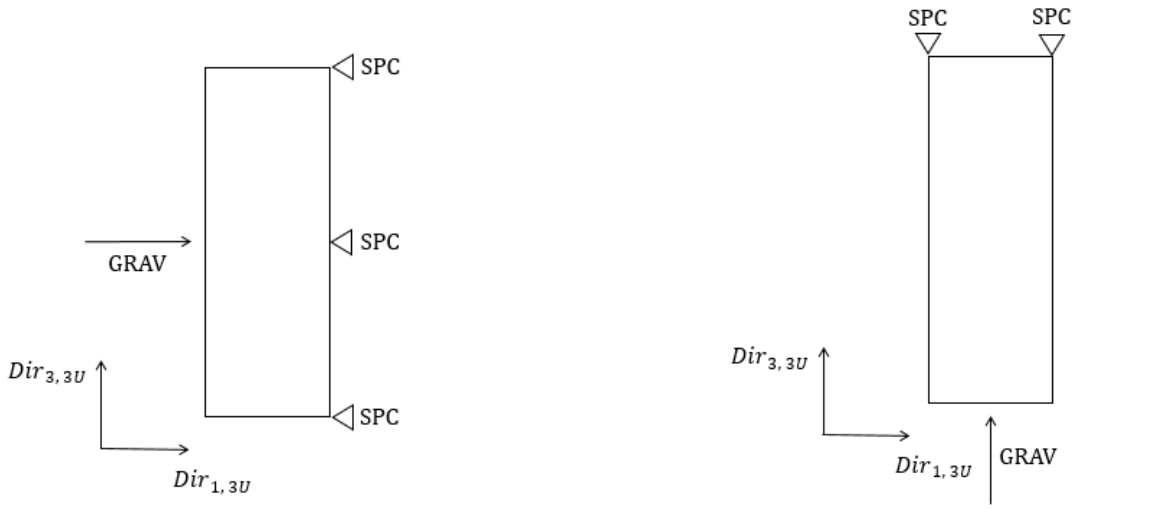

(a) Scheme for direction 1 ($x-$ or $y-$axis) load cases.

(b) Scheme for direction 3 ($z-$axis) load cases.

Figure 3.3: Boundary conditions scheme for each linear static load case.

refined until a converged result is achieved.

A mesh convergence study must be performed for each analysis. The starting point for the convergence studies were elements with 10 mm size, since it is the maximum size supported by several satellite structures. However, it must be noted that a 50 mm elements size was also included in the convergence graphics, so that a better perspective on the convergence tendency could be attained. The design used for these studies was the satellite with 2 mm thickness aluminium side panels.

Regarding the static analysis, the procedure applied can be outlined as follows:

1. Initial element size is set, applied to all surface elements and the total number of elements in the FEM model is registered;
2. Results from the analysis are obtained and the values of displacement, stress and strain for the element with maximum stress are registered;
3. The position of the previous element is taken as the reference value for the following iterations;
4. The number of elements is increased (elements size decreased) and the total number of elements in the FEM model is recorded;
5. Results from the analysis are obtained and the values of displacement, stress and strain for the element in the reference position (defined in step 3) are registered;
6. Steps 4 and 5 are repeated until the value of displacement, stress and strain are converged.

In Fig. 3.4 (a), (b) and (c) the converging values of displacement, stress and strain, respectively, and the corresponding computation time, for the static linear analysis of the 3U CubeSat can be observed.

As depicted, with the increase number of elements in the model the computation time also increases, however the computation times are small and, therefore, not a decision factor. The displacement, stress and strain conver-

gence begins to be attained for a number of 35514 elements in the model and, therefore, since time is not a concern, the following point was selected as the converged model - the FEM model with 57659 elements.

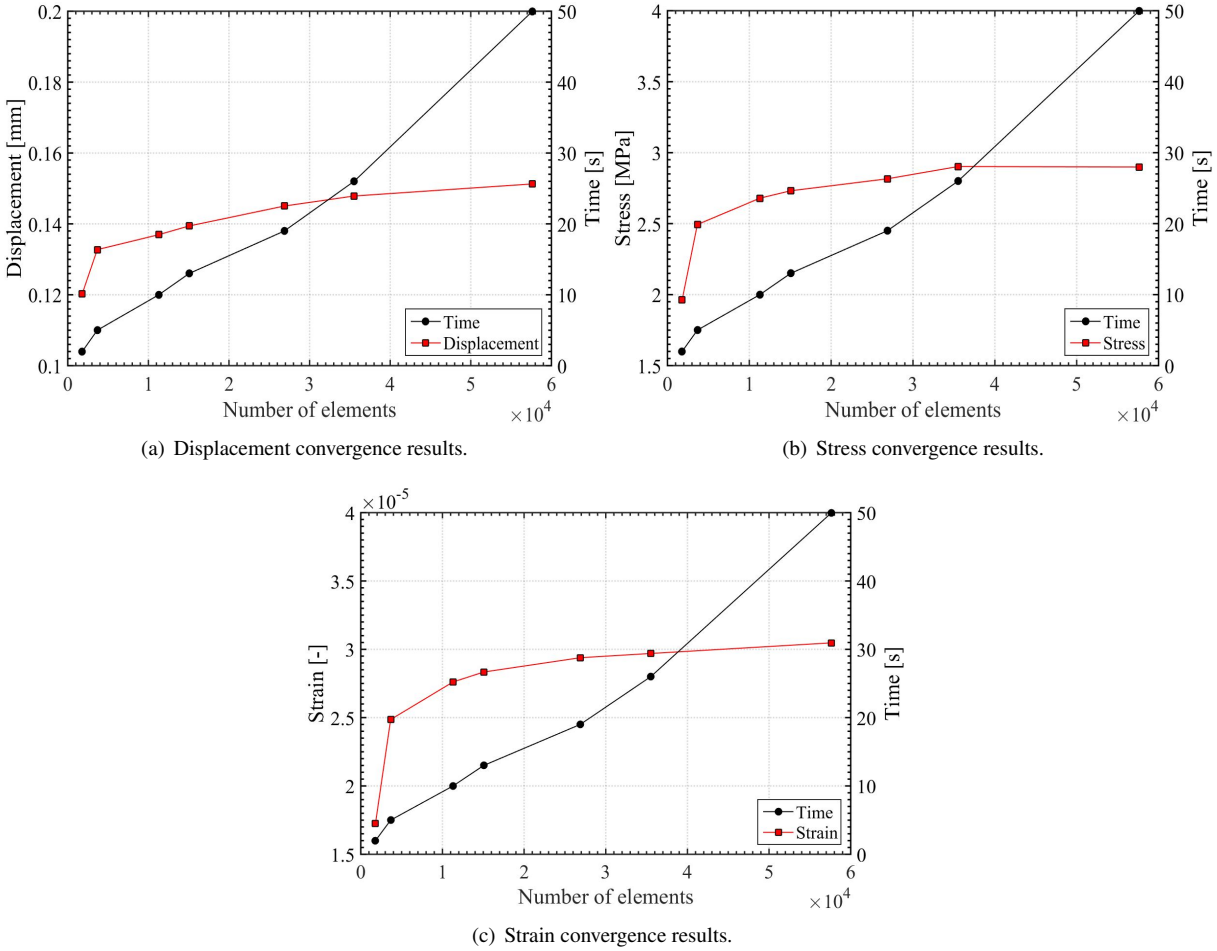

(a) Displacement convergence results.

(b) Stress convergence results.

(c) Strain convergence results.

Figure 3.4: Linear static analysis mesh convergence results.

Figs. 3.5 (a), (b) and (c) presents the displacement, stress and strain results for the converged linear static FEM aluminium model. The computed MOSs are depicted in Fig. 3.5 (d) (in Sec. 3.3.1 the MOS results are discussed in more detail). Note that in Fig. 3.5 the MOSs values greater than 6 were represented as equal to 6. To enable the visualization of the internal structures one of the side panels is presented as transparent. Only the load case B is presented, since it represents the highest load case.

A similar procedure as the one previously used was applied for the modal analysis convergence study. Comparing with the static analysis convergence, the modal analysis does not require the evaluation of secondary variables, since normal modes are directly obtained from the governing equations. Recall from Sec. 2.1.1, the displacement is a primary variable, directly obtained from the analysis, and stress and strain are derived from the former, thus known as secondary variables. Therefore, the variables selected to be monitored in the present convergence study are the natural frequencies associated with the first four modes of vibration.

In Fig. 3.6 the convergence obtained and the respective computation time for the modal analysis can be observed. Convergence starts to be attained for a number of 26868 elements in the model. The following point is selected as the converged model - the FEM model with 35514 elements. Note that for a model with 57659

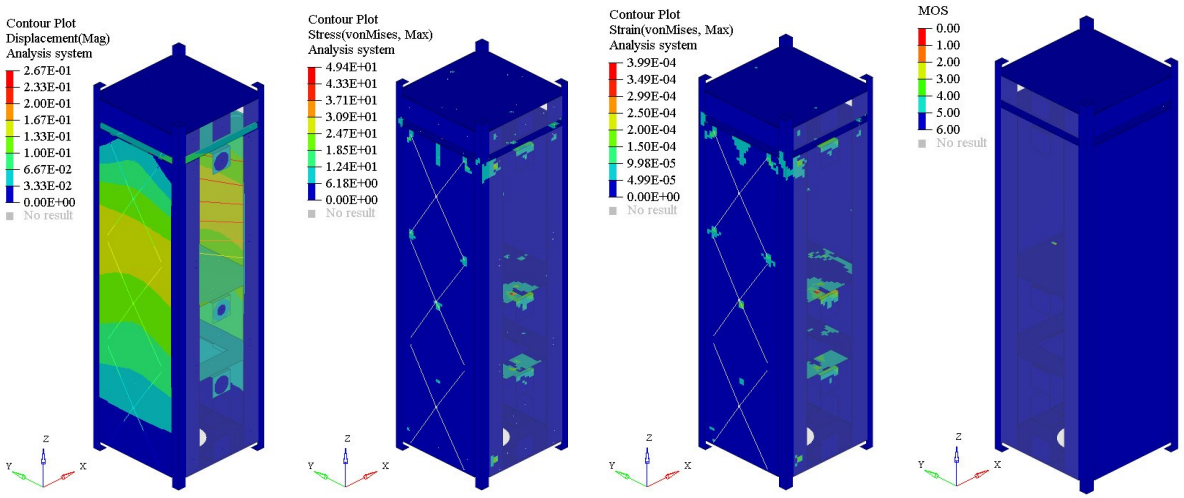

(a) Displacement results. (b) Stress results. (c) Strain results. (d) MOS computed.

Figure 3.5: Displacement, stress, strain linear static analysis results and MOS computed for the aluminium design load case B.

elements, the solution starts to diverge.

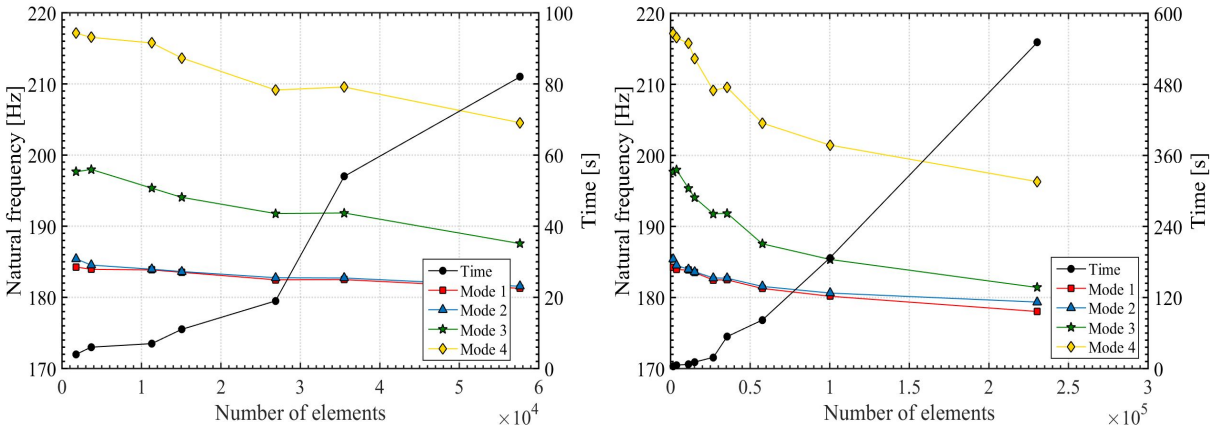

(a) Normal mode analysis mesh convergence close-up. (b) Normal mode analysis divergent results.

Figure 3.6: Normal mode analysis mesh convergence results.

Fig. 3.7 presents the first four modes of vibration of the converged normal mode FEM aluminium model. Note that the first six frequencies are neglected, since they are associated with the rigid body motion due to the unconstrained model. Hence, the first four modes of vibration correspond to mode 7, 8, 9 and 10, being the fundamental frequency f_7.

3.3 Structural Optimization Design Process

Once the structural FEM models are finished, the optimization design cycle previously presented in Sec. 2.2, in Fig. 2.4 (b), can be carried out.

It is important to remember that the main goal of this work is to assess the possibility of reducing the structural mass of a 3U CubeSat by replacing the 2 mm thickness aluminium side panels with a laminated composite material,

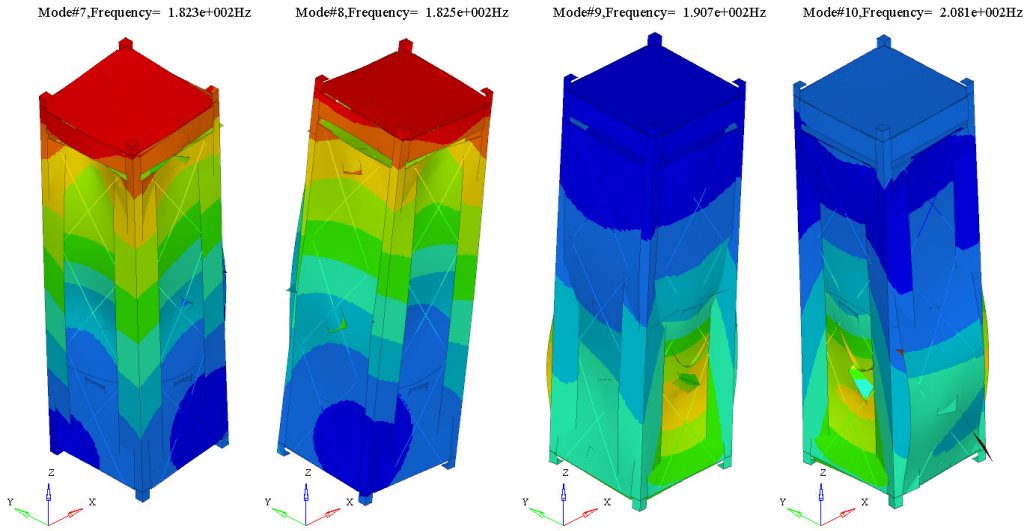

Figure 3.7: First four vibration modes of the converged normal mode FEM aluminium model.

without compromising the structural and thermal performance of the satellite. Hence, the satellite with laminated composite materials as its side panels must be lighter and present an identical behaviour on each of the analysis, as the aluminium one.

The laminated composite materials to be assessed via numerical analysis were already selected in Sec. 2.2.1. These materials are the starting point of the optimization cycle and each represent a different design. As stated the selected materials were:

- Number 3: CFRP with aluminium core and total thickness of 0.75 mm;
- Number 7: CFRP with pyrolytic graphite core and total thickness of 0.7 mm;
- Number 16: GFRP with pyrolytic graphite core and total thickness of 0.7 mm;

In Tab. 3.4, the percentage of structural mass reduction for each side panel of the previous designs comparing with the aluminium one is presented. All designs have a significant mass reduction, being laminate number 7 the more advantageous concerning the weight goal.

Table 3.4: Structural mass reduction for each side panel.

Designs	Structural mass reduction [%]
Laminate n^o 3	74.7
Laminate n^o 7	80.6
Laminate n^o 16	77.3

The optimization processes followed can be summarized as follows: the analysis results were obtained and if the satellite with the composite laminates present an identical structural response to the aluminium one, the analysis proceeds to the thermal analysis. If not the laminates are optimized until an identical response is obtained.

3.3.1 Linear Static Analysis Results

In the linear static analysis, three distinct assessments must be made:

1. The critical components, i.e. the components that present the lower MOS, in each design and load case must be identified;
2. The MOS and failure indexes of the satellite side panels for each design must be computed using the failure theories introduced in Sec. 3.1.3;
3. The bolts' behaviour shall be evaluated and its MOS computed.

Tab. 3.5 presents the maximum values of displacement, von Mises stress, strain and the respective MOS for each load case for the aluminium side panels of the satellite. As can be concluded, for all cases the structural requirement established in Sec. 3.1.1 is satisfied, i.e. MOS≥ 0 (Eq. 3.1). The minimum MOS is equal to 1.93 and is achieved in case B, which was expected since this case corresponds to the maximum load case conducted ($+14.5g$).

Table 3.5: Maximum displacement, strain, stress and MOS of the linear static cases analyses for aluminium side panels.

Cases	Max. displacement [mm]	Max. strain	Max. stress [MPa]	MOS
A	0.112	2.92E-04	35.8	3.0
B	0.156	3.99E-04	49.4	1.93
C	0.032	7.82E-05	9.54	14.19
D	0.032	7.85E-05	9.54	14.18
E	0.017	4.60E-05	4.80	29.18
F	0.017	4.62E-05	4.83	29.00

Concerning all the other satellite designs, Tab. 3.6 shows the critical MOS computed for each load case. As can be concluded, the critical components are the systems' supports. However, for all cases a MOS≥ 0 is attained and, therefore, the components do not fail, presenting a similar behaviour as the satellite with the aluminium panels. Once more the worst case scenario corresponds to the load case B, which presents the smallest MOS of all load cases.

Table 3.6: Critical components MOS.

Cases	Aluminium	Laminate nº 3	Laminate nº 7	Laminate nº 16
A	3.00	3.30	3.45	3.28
B	1.93	2.11	2.22	2.09
C	14.19	15.32	15.55	15.20
D	14.18	15.32	15.53	15.14
E	29.18	18.10	17.92	17.46
F	29.0	18.13	17.93	17.50
Component	System support			

Regarding the side panels, the maximum failure indexes computed for each of the different hybrid laminates are presented in Tab. 3.7. For all load cases, the laminated composite materials meet the requirements established, i.e failure index smaller than 1 (Eq. 3.10).

In Figs. 3.8, 3.9 and 3.10, the MOS and failure index obtained for each hybrid laminate design can be observed for the worst load case, i.e. case B. The structures that did not enter the MOS or the failure index computations are

Table 3.7: Maximum failure index of the satellite's side panels.

Cases	Failure index		
	Laminate n^o 3	Laminate n^o 7	Laminate n^o 16
A	0.333	0.353	0.410
B	0.459	0.487	0.778
C	0.096	0.102	0.081
D	0.096	0.102	0.081
E	0.032	0.029	0.011
F	0.032	0.029	0.011

presented as transparent in the correspondent figures. From the figures it can be easily seen that the system support presents the lower MOS in all designs, as in the aluminium design (see Fig. 3.5 (d)). Note that in the figures, for MOS values greater than 6, these values were represented as equal to 6.

Although, the side panels and all components meet the requirements, an analysis on the bolts must be performed, to ensure they will not fail. Therefore, the bolts' MOS for each load case must be computed as well.

Since all bolts were modelled as 1D elements, the axial and shear stresses had to be directly computed from the axial and shear forces obtained from the FEM analysis using the following equation,

$$\sigma_t = \frac{F}{A_t}, \tag{3.14}$$

where, F is the force applied to the bolts and A_t the tensile area of the bolts (Eq. 3.12). The force applied to the bolts is divided in two types: axial force and shear force. Hence, two stress are also computed: axial stress (σ) and shear stress (τ). For each of those stress a MOS is obtained, MOS_A and MOS_S. However, to account for the effect of the interaction between the two types of forces a final MOS needs to be estimated, MOS_I, which can be given by the following equation [109],

$$MOS_I = \frac{1}{\sqrt{R_A^2 + R_S^2}} - 1, \tag{3.15}$$

where

$$R_A = \frac{\sigma \times FOSU}{P}, \tag{3.16a}$$

$$R_S = \frac{\tau \times FOSU}{S}, \tag{3.16b}$$

with P equal to the proof strength of the bolts' materials and S to its shear strength. The bolts' material is stainless steel 304 with a proof strength equal to 600 MPa [105] and a shear strength equal to 346.4 MPa (Eq. 3.9). The proof strength is the maximum load a bolt can withstand without acquiring a permanent deformation [105]. In the case of bolts, the proof strength is used instead of the ultimate strength, since plastic deformation may lead to a loosen connection and the bolts are considered to fail. The FOSU can be found in Tab. 3.2.

Tab. 3.8 shows the bolts' minimum MOS_A, MOS_S and MOS_I computed for each load case and side panel material. As can be seen, the minimum MOS is equal to 2.64, which meet the requirements (MOS$\geq$ 0).

As all the different designs present a similar behaviour as the aluminium one, it is not necessary to optimize any of the proposed laminates and the normal mode analysis can be conducted.

Table 3.8: Minimum bolts' MOS of the linear static analysis.

Cases	MOS	Aluminium	Laminate n^o 3	Laminate n^o 7	Laminate n^o 16
A	MOS_A	21.40	17.06	16.36	17.62
	MOS_S	4.05	4.76	4.74	4.57
	MOS_I	4.05	4.76	4.74	4.57
B	MOS_A	15.10	12.31	11.86	12.73
	MOS_S	2.64	3.81	3.59	3.97
	MOS_I	2.64	3.52	3.32	3.67
C	MOS_A	85.47	67.05	64.91	67.40
	MOS_S	16.78	18.89	18.82	18.36
	MOS_I	16.78	18.89	18.81	18.36
D	MOS_A	85.17	68.41	66.34	68.72
	MOS_S	17.42	19.05	18.92	18.56
	MOS_I	17.42	19.05	18.92	18.56
E	MOS_A	103.11	90.79	90.64	90.92
	MOS_S	47.89	53.65	54.53	53.36
	MOS_I	47.71	53.62	54.52	53.33
F	MOS_A	103.28	91.01	90.95	91.15
	MOS_S	49.17	53.71	54.64	53.45
	MOS_I	48.40	53.69	54.64	53.41

3.3.2 Normal Mode Analysis Results

Using the FEM model created in Sec. 3.2, the normal mode analysis was performed for each of the previous four designs (aluminium and laminates n^o 3, 7 and 16). In Tab. 3.9, the natural frequencies associated with the first ten modes of vibration of each design are presented. As explained in Sec. 3.2.4, the first six frequencies, associated with the rigid body motion, are neglected.

Table 3.9: First natural frequencies of the normal mode analysis.

Mode	Natural frequency [Hz]	Aluminium	Laminate n^o 3	Laminate n^o 7	Laminate n^o 16
1	f_1	9.24E-04	6.71E-04	9.29E-04	8.58E-04
2	f_2	7.35E-04	2.78E-04	3.80E-04	6.05E-04
3	f_3	5.22E-04	1.67E-04	4.44E-04	3.65E-04
4	f_4	3.96E-04	2.16E-04	6.14E-04	3.09E-04
5	f_5	1.85E-04	8.43E-04	9.86E-04	7.00E-04
6	f_6	5.65E-04	8.94E-04	1.04E-03	7.61E-04
7	f_7	182.28	75.90	67.04	40.90
8	f_8	182.47	76.98	67.97	41.51
9	f_9	190.71	78.09	68.95	42.17
10	f_{10}	208.11	131.22	132.63	78.87

As can be seen, the fundamental frequency of the satellite with 2 mm aluminium thickness plates is equal to 182.38 Hz, which meets the requirement of having a fundamental frequency higher than 115 Hz (Sec. 3.1.1). However, none of the other laminate plates meets this requirement and, therefore, their design needs to be revised. Hence, the thickness of the fibre reinforced polymer (CFRP and GFRP) layers of each laminate were gradually increased, until they meet the 115 Hz frequency goal. The laminates which meet the requirement are the following hybrid structures:

- Number 3.1): CFRP with aluminium core and total thickness of 1.15 mm, each FRP lamina with 0.25 mm;
- Number 7.1): CFRP with pyrolytic graphite core and total thickness of 1.3 mm, each FRP lamina with 0.3 mm;
- Number 16.1): GFRP with pyrolytic graphite core and total thickness of 1.7 mm, each FRP lamina with 0.4 mm.

Tab. 3.10 shows the updated laminates fundamental frequencies, and, as can be seen, all designs meet the 115 Hz goal.

Table 3.10: First natural frequencies of the structural optimized laminates.

Mode	Natural frequency [Hz]	Aluminium	Laminate n^o 3.1)	Laminate n^o 7.1)	Laminate n^o 16.1)
1	f_1	9.24E-04	9.19E-04	1.26E-03	8.96E-04
2	f_2	7.35E-04	7.31E-04	9.19E-04	7.68E-04
3	f_3	5.22E-04	4.64E-04	4.47E-04	6.43E-04
4	f_4	3.96E-04	2.00E-04	3.90E-04	5.93E-04
5	f_5	1.85E-04	4.71E-04	4.26E-04	4.95E-04
6	f_6	5.65E-04	6.29E-04	7.43E-04	3.00E-04
7	f_7	182.28	122.69	137.26	118.70
8	f_8	182.47	124.69	139.72	120.79
9	f_9	190.71	125.80	140.41	121.98
10	f_{10}	208.11	178.53	180.34	163.57

In Figs. 3.11, 3.12 and 3.13, the first four modes of vibration, neglecting the rigid body modes, of each design can be observed. The vibration modes of the aluminium design were previously presented in Fig. 3.7.

Despite of the increase in thickness and, consequently, in mass of the updated laminates, the new designs continue to present a lower structural mass than the aluminium design and, therefore, are still valid candidates to be analysed. Tab. 3.11 shows the updated designs' structural mass reduction.

Table 3.11: Structural optimized laminates' mass reduction for each side panel.

Designs	Structural mass reduction [%]
Laminate n^o 3.1)	62.9
Laminate n^o 7.1)	62.9
Laminate n^o 16.1)	42.1

Following these laminate optimizations, the thermal static analysis can be performed with the new materials suggested. To achieve this, a new FEM model that can reliably model the thermal behaviour of the satellite must be created. In Chap. 4, the thermal FEM model and the thermal optimization design process are presented.

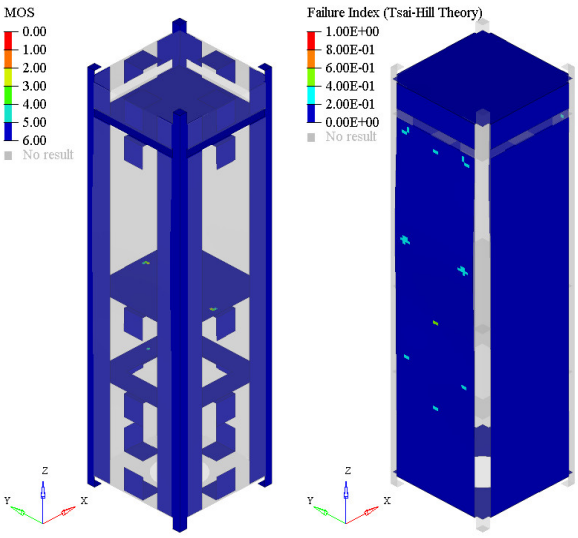

Figure 3.8: MOS and failure indexes results of laminate n^{o} 3) design for load case B.

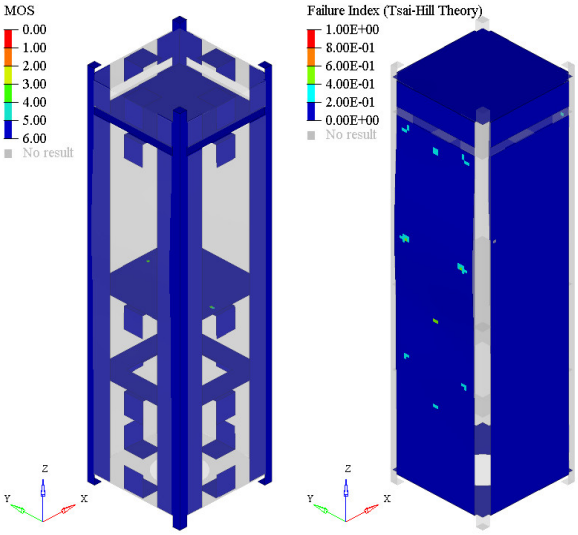

Figure 3.9: MOS and failure indexes results of laminate n^{o} 7) design for load case B.

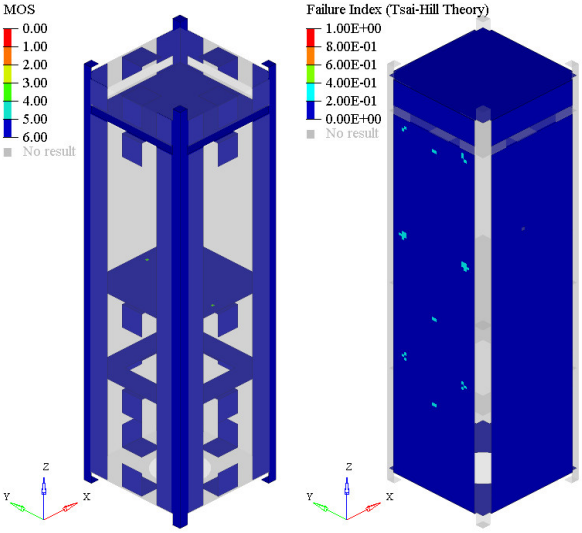

Figure 3.10: MOS and failure indexes results of laminate n^{o} 16) design for load case B.

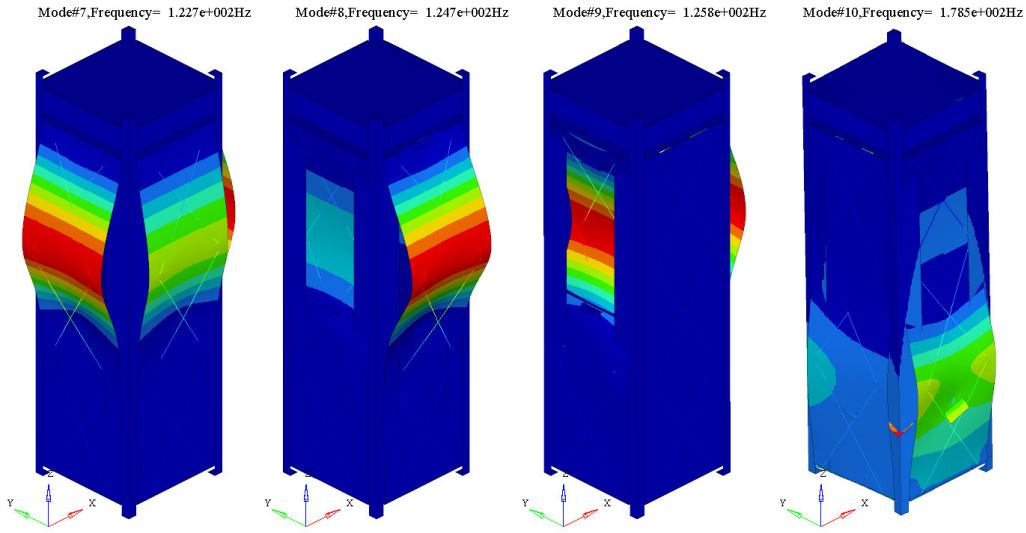

Figure 3.11: First four vibration modes of laminate nº 3.1) design.

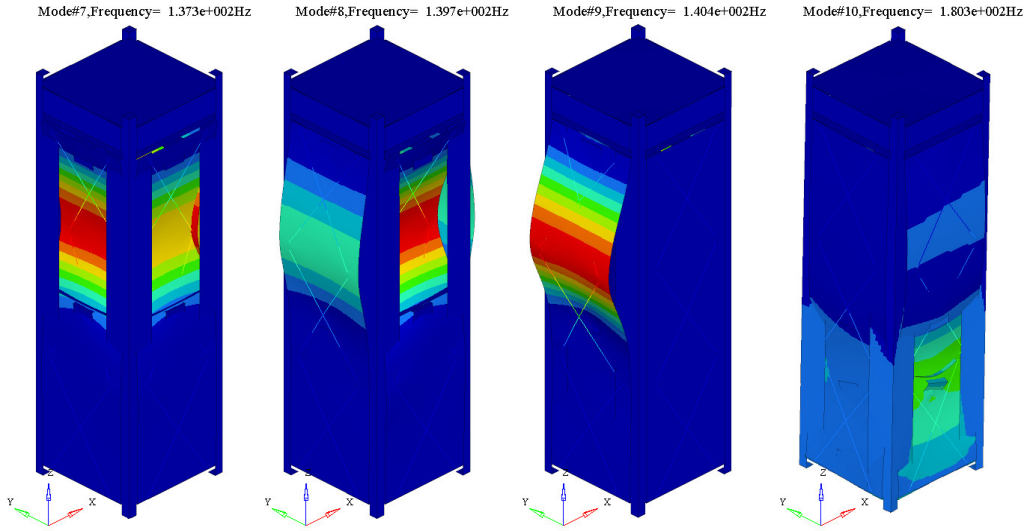

Figure 3.12: First four vibration modes of laminate nº 7.1) design.

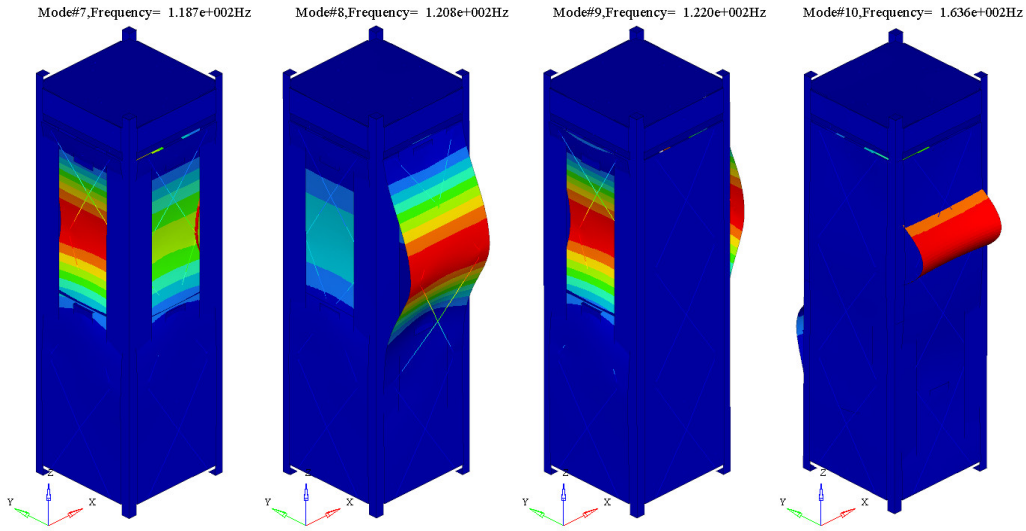

Figure 3.13: First four vibration modes of laminate nº 16.1) design.

Chapter 4

Thermal Analysis

The current chapter aims to provide a thermal analysis analogous to the one put forth regarding the structural nature on Chap. 3.

In Sec. 4.1, the theoretical background that supports the understanding of the following thermal analysis to be performed is presented, namely the space thermal environment, the thermal requirements that must be fulfilled by orbiting satellites and the static thermal governing equations.

The satellite under analysis is the one introduced in Sec. 1.3. Sec. 4.2 presents all the required data and reasoning behind the creation of its thermal FEM model. Since, this model presents a much higher degree of complexity and, additionally, the nature of the problem is so distinct from the previous static and modal analysis, it was decided to dedicate an entire chapter to it.

Sec. 4.3 presents the thermal results obtained for the laminates being analysed and the optimizations performed.

As in the structural analysis, the equivalent documentation regarding the thermal standards and handbooks developed by ECSS were consulted, as the references [93] and [110].

It should be noted that this chapter is not meant to provide an exhaustive review on the FEM thermal analysis, and so, only the fundamental topics to understand the numerical analysis performed in the current work are discussed. References [111] and [65] are some of the available literature that can be consulted to obtain a complementary review on these topics.

4.1 Theoretical Background

4.1.1 Space Thermal Environment

As explained in Sec. 1.1.1, orbiting spacecrafts are subjected to very harsh environments due to the extreme temperatures they experience when exposed to the Sun and when in total darkness (eclipse conditions). Since convection can be negligible in space, the two main methods of heat transfer are conduction and radiation [19].

Heat transfer by radiation is governed by the Stefan-Boltzmann's law, that relates the total emissive power of a body with its temperature, which represents the total heat flux emitted by a black body. However, this law is idealized for black bodies, characterised by absorbing all incident electromagnetic radiation, which is not true for a real (grey) body. For those, the material's emissivity, ε, must be taken into account, and, therefore, the Stefan-Boltzmann law is modified as follows [20]:

$$q_{rad} = \varepsilon \sigma_0 T^4, \tag{4.1}$$

where q_{rad} is the radiation flux emitted by a body, σ_0 is the Stephan-Boltzmann constant equal to $5.669 \times 10^{-8}\,\mathrm{W/(m^2K^4)}$ and T the body's temperature in Kelvin. To obtain the total energy Q_{rad}, the flux q_{rad} is multiplied by the radiating surface area A_{rad}.

Typically, satellites reach a thermal equilibrium while in orbit, having their temperatures fluctuating between a maximum and a minimum. Hence, temperature can be determined by an energy balance between the energy received q_{in} from the environment; the internal heat generated by the electronic components q_d; and the lost thermal radiation q_{out} to the environment, related with the grey body emissions of the satellite to space (Eq. 4.1) which, according to reference [93], is assumed to be at 3 K. The energy balance can be written as $q_{in} + q_d - q_{out} = 0$.

In Earth's orbit, the received flux q_{in} can be divided in three main sources (Sec. 1.1.1), $q_{in} = q_S + q_E + q_A$ [93]:

1. Solar flux q_S: The incident solar radiation depends on the solar flux G_S, the materials' absorptivity on the visible spectrum α_S and the angle between the solar rays and the satellite surface normal θ_S. All solar radiation is assumed to be parallel, since the source is much bigger than the satellite and is far away. Hence, solar flux can be given as

$$q_S = G_S \alpha_S \cos\theta_S. \tag{4.2}$$

2. Earth's infrared radiation flux q_E: Radiation emitted by Earth that reaches the satellite does not only depend on the IR radiation emitted by Earth and on the materials' absorptivity on the infrared spectrum α_{IR} (which is assumed to be equal to the materials' emissivity [112]), but also on a view factor parameter, since parallel illumination cannot be assumed due to the proximity of the source:

$$q_E = q_{IR} \alpha_{IR} F_E, \tag{4.3}$$

   where q_{IR} is the IR radiation emitted by Earth, which is assumed to have an average value of $230\,\mathrm{W/m^2}$ [93], and F_E is the Earth view factor.

   View factors allow to compute the radiation exchange between any two surfaces. It represents the fraction of total radiated energy from one surface (source) incident on another. In the case of Earth's view factor there are several methods to approximate its value. However, according to ECSS [113], the view factor can be given by

$$F_E = B_0 + B_1 \cos\theta_E + B_2 \cos^2\theta_E + B_3 \cos^4\theta_E + B_4 \cos^6\theta_E, \tag{4.4}$$

where θ_E is the angle between the surface's normal and the Earth centre and the coefficients B_i are [113]:

$$B_0 = \frac{2}{7\pi}\left(\frac{577}{105} - 7\cos\varpi + \frac{4}{3}\cos^2\varpi - \frac{2}{5}\cos^5\varpi + \frac{4}{7}\cos^7\varpi\right), \tag{4.5a}$$

$$B_1 = \frac{1}{2}\sin^2\varpi, \tag{4.5b}$$

$$B_2 = \frac{8}{7\pi}\left(\cos\varpi - 2\cos^3\varpi + 4\cos^5\varpi - 3\cos^7\varpi\right), \tag{4.5c}$$

$$B_3 = \frac{4}{7\pi}\left(-\cos\varpi + \frac{40}{3}\cos^3\varpi - \frac{91}{3}\cos^5\varpi + 18\cos^7\varpi\right), \tag{4.5d}$$

$$B_4 = \frac{8}{35\pi}\left(5\cos\varpi - 35\cos^3\varpi + 63\cos^5\varpi - 33\cos^7\varpi\right), \tag{4.5e}$$

with $\varpi = \arcsin\frac{r_E}{h+r_E}$, where r_E is the Earth's radius and h the orbital altitude.

3. Albedo radiation flux q_A: The Sun radiation reflected by Earth is defined by Earth's Albedo (a_E), which has an average value of 0.3 [93]. It also depends on a view factor parameter F_A, that is a function of Earth's view factor as follows [114]:

$$F_A = F_E\cos(0.9\theta_A), \tag{4.6}$$

where θ_A is the angle made by the satellite, Earth and Sun.

The Albedo radiation flux is then given by

$$q_A = G_S a_E \alpha_S F_A. \tag{4.7}$$

To ensure satellites can operate under such thermal conditions, several thermal requirements must be met.

4.1.2 Thermal Requirements

The requirements by the ECSS in Thermal Control General Requirements standard [115] state that the mission phases shall be represented by a coherent set of thermal design cases covering the extreme range of conditions experienced by the spacecraft. Therefore, the dimensioning environmental worst design cases, known as the hot and cold cases, shall be used. The temperatures of all electric components must remain within the allowable temperatures defined by the systems authority under such cases. Furthermore, temperature gradients must be specified and defined in accordance to the mission objectives and taking into account the spacecraft properties being analysed.

Since the objective of this thesis is to assess the use of composite materials instead of aluminium for the satellite side panels, low thermal gradients are sought in the composite panels as explained in Sec. 2.1.2. Therefore, for the present work it was established that the maximum temperature gradients of the composite panels shall be similar to the ones obtained for the aluminium ones.

Inaccuracies in environmental, physical and modelling parameters can lead to uncertainties on spacecraft temperature predictions. In order to account for such uncertainties a ± 10 K temperature margin must be applied to the maximum and minimum temperatures for preliminary design analysis [115].

Once the thermal environment and requirements are defined, the thermal behaviour of satellites must be pre-

dicted and, therefore, thermal FEM analysis performed.

4.1.3 Static Thermal Analysis

As explained in Sec. 3.1.2, several types of FEM analyses can be performed and the governing equations that hold for each case are different. For the static thermal analysis, the general equation of motion 3.2, which is analogous for any static problem, can be re-written as [111]

$$\left[K_C + H\right]\left\{T\right\} = \left[F\right], \tag{4.8}$$

where K_C is the conductivity matrix, H the boundary convection matrix, T are the unknown nodal temperatures and F the applied thermal loading vector. $[F] = F_{rad} + F_H + F_I$, where F_{rad} is the power due to the radiation flux, F_H the boundary convection vector and F_I the power due to internal heat generation. Since convection is negligible in the space environment, H and F_H are considered null. The system is then solved to find the nodal temperatures T.

To perform a steady-state heat transfer analysis, the thermal FEM model needs to be created and due to the requirements and nature of the analysis, a complex model needs to be devised.

4.2 Finite Element Model

As stated before, the creation of a FEM model is a methodic process based on the same hierarchy steps despite the analysis being performed. Hence, the steps followed in Sec. 3.2 to create the thermal FEM model are implemented in this section, namely the structure idealization, mesh creation, definition of boundary conditions and loads, as well as the mesh convergence study. Also, the sensitivity studies performed to assist in certain modelling decisions are outlined.

4.2.1 Part Idealization

Analogous to the static and modal analysis, a structure simplification must be performed. However, distinct simplifications were considered, since the thermal behaviour of the components needed to be correctly simulated, allowing for a more detailed observation of the temperatures' distributions in the satellite. The simplifications considered were:

1. All round edges, chamfers, fillets, holes and small design features were removed;
2. All electronic subsystems were converted into 2D structures, with the exception of the battery cells and magnetorquers, which were modelled as 3D structures with simplified geometries since their dimensions are of the same magnitude;
3. All structures, with the exception of bolts and endless screws, were converted into 2D surfaces;
4. The bolts and endless screws were converted into 1D structures;

5. The nanocamera was modelled with 2D and 3D structures, where its PCB was represented by its midsurface and the lens and main structure as a cylinder.

Sensitivity Study

To evaluate the validity of modelling 3D structures as 2D structures, a sensitivity study was performed. For this purpose, two FEM models were created.

In the first model, a structure with 100 mm $\times$ 100 mm and 2 mm thickness was created and modelled with 3D elements (CHEXA) with a thermal conductivity of 200 $\mathrm{W/(mK)}$. A radiation flux of 1 $\mathrm{mW/mm^2}$ was applied to the upper surface.

The second model consisted in the same structure converted into a 2D surface, represented by its mid-surface. The structure was modelled with 2D elements (CQUAD4) and the same radiation flux was applied.

Fig. 4.1 expose the static thermal analysis results, where temperature distribution can be observed for both models. On the upper surface of the 3D structure a maximum temperature of 387.3 K was reached and in the lower surface a temperature of 385.3 K was obtained. As for the 2D structure, an uniform temperature of 385.3 K was achieved. The maximum temperature difference between the two models is equal to 2 K. Therefore, it can be concluded that for structures with a small thickness, the temperature differences are also small. Hence, in the present work, this difference was considered negligible and all structures with small thickness were modelled as 2D structures.

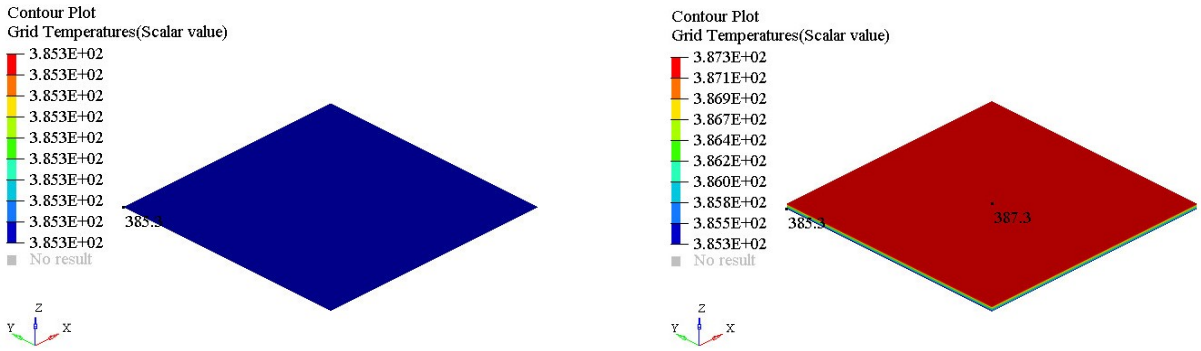

(a) Sensitivity temperature results for a 2D structure.

(b) Sensitivity temperature results for a 3D structure.

Figure 4.1: Sensitivity study comparing temperature results for 2D and 3D structures with small thickness (units in Kelvin).

4.2.2 Element Properties

Regarding the mesh generation, in thermal analysis a more complex process needs to be undertaken, since radiative elements (RADM) must be assigned to each element of the mesh to account for the radiation exchanges [111]. The thermal-optical properties of each structure and component are assigned to the corresponding RADM element of the respective mesh. 1D structures were assumed not to contribute to the radiation exchanges.

For the 3D structures mentioned in Sec. 4.2.1, 3D elements (CHEXA) are used to mesh the geometries and the PSOLID property card assigned is to the elements.

Concerning the 2D structures, surface elements (CQUAD4) are used and the PSHELL card is assigned. Note that for modelling a n-ply composite material in the previous analysis, a PCOMP card could be assigned. However, with the pre-processing software being used for steady state thermal analysis, composite materials cannot be easily modelled. Therefore, composites were modelled as equivalent single layers with their thermal conductivity properties computed using Eqs. 2.31.

According to reference [116], the PCBs thermal conductivity values can be estimated, based on experimental measurements, as follows:

$$k_{in-plane} = 385\frac{t_{Cu}}{t} + 0.87, \tag{4.9a}$$

$$k_{transverse} = \left[3.23\left(1 - \frac{t_{Cu}}{t}\right) + 0.0026\frac{t_{Cu}}{t}\right]^{-1}, \tag{4.9b}$$

where t_{Cu} is the thickness of the copper layers and t the total thickness of the PCB. It was assumed that all PCBs have four layers of copper with 35 μm each. All the subsystems material properties were assumed to be equal to those of a PCB, with the exception of the thermal-optical properties of the solar panels, which were considered to be the same as the solar cells, since these occupy more than 90% of the solar panel area.

1D structures were modelled exactly as in the structural FEM models (see Sec. 3.2).

Tab. 4.1 summarizes the structure simplifications made and the mesh properties for each component of the satellite. In Tab. 4.2, the used thermal properties of the different materials can be consulted.

Table 4.1: Thermal FEM model mesh properties.

Structure idealization	Component	Element type	Property card	Material
3D	Magnetorquers	CHEXA	PSOLID	Ferrite
	Battery cells			Properties in Tab. 4.2
	NanoCamera - Lens			Glass
	NanoCamera - Structure			Polypropylene
2D	Rails	CQUAD4	PSHELL	Aluminium 6061 T6
	System supports			Aluminium 6061 T6
	Payload support			Aluminium 6061 T6
	Side panels			Aluminium 6061 T6 or Laminated composite material
	Transceiver			FR4-TG 130-140 and copper
	Power board - PCB			FR4-TG 130-140 and copper
	Power control board			FR4-TG 130-140 and copper
	OBC			FR4-TG 130-140 and copper
	Magnetorquers board - PCB			FR4-TG 130-140 and copper
	NanoCamera - PCB			FR4-TG 130-140 and copper
	Solar panels - PCB			FR4-TG 130-140 and copper
	Solar cells			GaAs+Ge
1D	Bolts	CBAR	PBAR	Stainless steel 304
	Endless screws	CBEAM	PBEAM	Stainless steel 304
	Connections	RBE2	[−]	[−]

In Figs. 4.2 (a), (b) and (c), the thermal FEM model developed heretofore is presented, due to legibility purposes not all elements are identified and three different views are presented. Note that to allow the visualization of the internal components on the assembly, one of the side panels was made transparent.

Table 4.2: Materials' thermal properties.

Material	k [W/(mK)]		α [−]	ε [−]
Aluminium 6061 T6 (anodized) [84] [20]	167		0.14	0.84
Stainless steel 304 [117]	16.2		[−]	[−]
Ferrite [118]	83.5		0.56	0.56
Glass [39]	1.4		0.05	0.9
Polypropylene [39]	0.25		[−]	0.97
FR4-TG 130-140 and copper [39]	$k_{xx} = k_{yy}$	k_{zz}	0.8	0.89
	34.5	0.34		
GaAs+Ge [39]	[−]		0.92	0.85
Battery cells [119]	21.7		0.3	0.4

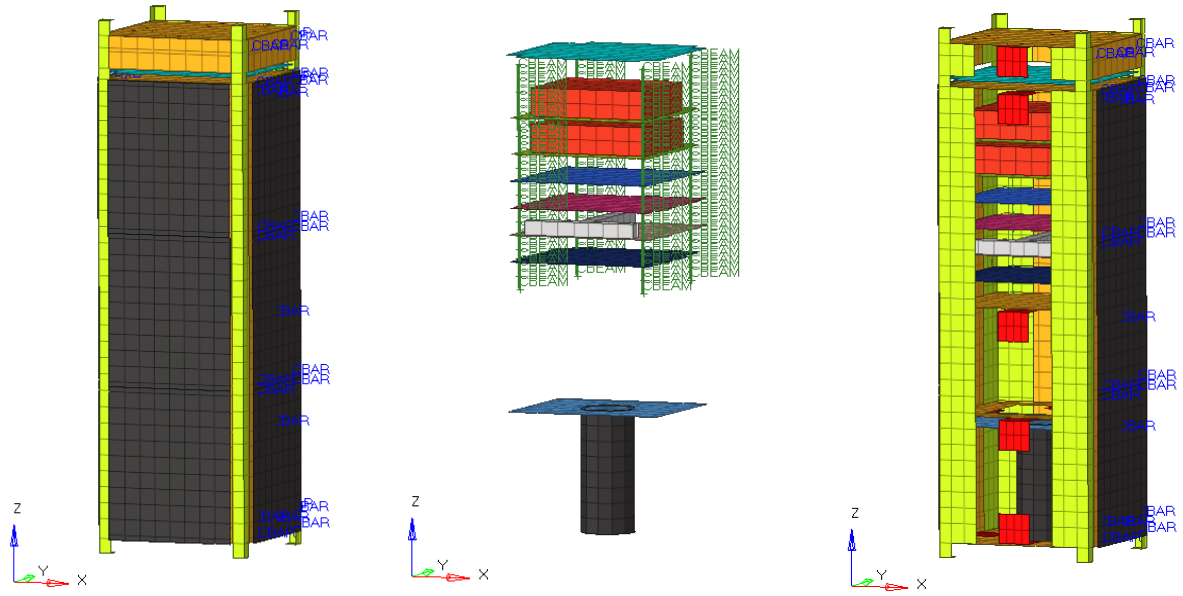

(a) External view. (b) Internal view. (c) External and internal assembly view.

Figure 4.2: External, internal and assembly views of the thermal FEM model.

4.2.3 Boundary Conditions

In this work, to comply with the ECSS standards presented in Sec. 4.1.2, two design cases are defined to be simulated individually in the steady state heat transfer analysis:

1. Hot case: It represents the conditions that causes the highest temperatures in a satellite, i.e. maximum solar flux and electronic systems operating at full power. The maximum solar flux is received by the satellite when it is closest to the Sun at perihelion, with an average value of 1412.9 W/m^2 [93];

2. Cold case: Characterized by the lowest solar flux received by the satellite, the cold case occurs during eclipse, when the satellite does not receive any solar radiation. Note that all electric components are considered to be in a non-operational state with an idle power consumption, with the exception of the power boards. Power boards have an incorporated heater that can change the amount of power it dissipates to ensure the battery cells do not reach temperatures below 0 ^{o}C. In order to define how much power should be dissipated by the heater, a sensitivity study was performed in the aluminium design model. The power dissipated by the heater was gradually increased, until the batteries reached a minimum and maximum temperature within its

operational range. Fig. 4.3 depicted the study performed. As can be seen, 0 W, 3 W, 4 W and 7 W dissipating powers were tested. Only for the 4 W power, the power boards can maintain a temperature that complies with its' operational range. Therefore, this power was established as the internal heat dissipated by each of those boards.

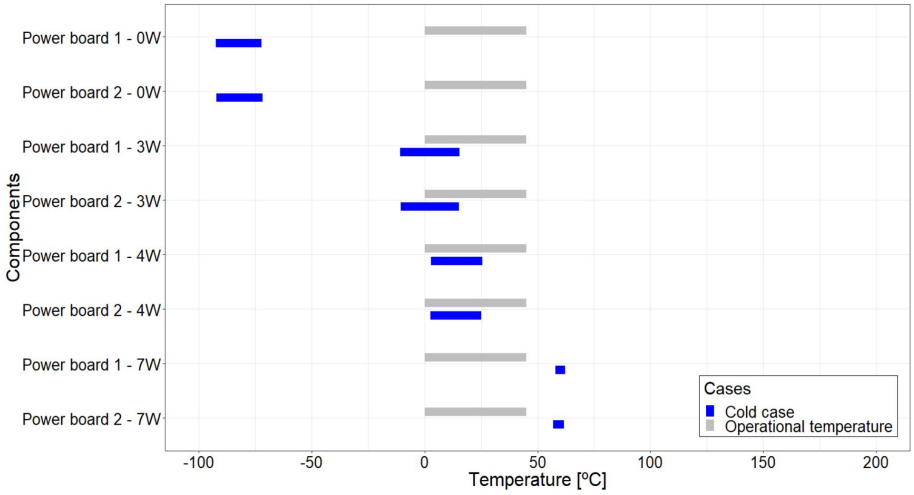

Figure 4.3: Power boards' extreme temperatures in function of the power dissipated by the boards' heaters.

These two worst conditions assure that any other possible orbits would receive a flux in-between them and, therefore, present temperatures limited by the extreme values reached in the hot and cold case.

In this work, the satellite is in a circular Sun-synchronous orbit (SSO) with an altitude of 550 km and it does not change its orientation during the orbit. Fig. 4.4 and Tab. 4.3 show the established hot and cold cases and the radiation fluxes reaching the satellite due to solar radiation G_S, albedo a_E and Earth's infrared radiation q_{IR}. In Tab. 4.4, the component's internal heat dissipation considered for each case are presented.

Table 4.3: Hot and cold case orbit and flux characteristics.

		Hot case	Cold case
Orbit type		SSO	
h	[km]	550	
e	[−]	0	
G_S [93]	[W/m^2]	1412.9	0
q_{IR} [93]	[W/m^2]	230	230
a_E [93]	[−]	0.3	0

Table 4.4: Component's internal heat dissipation.

	Internal heat dissipation [W]	
Component	Hot case	Cold case
Transceiver [56]	4	0
Power boards [57]	0.05	4
Power control board [59]	0.16	0
OBC [64]	0.65	0
Magnetorquers board [62]	1.2	0
NanoCamera [63]	0.8	0

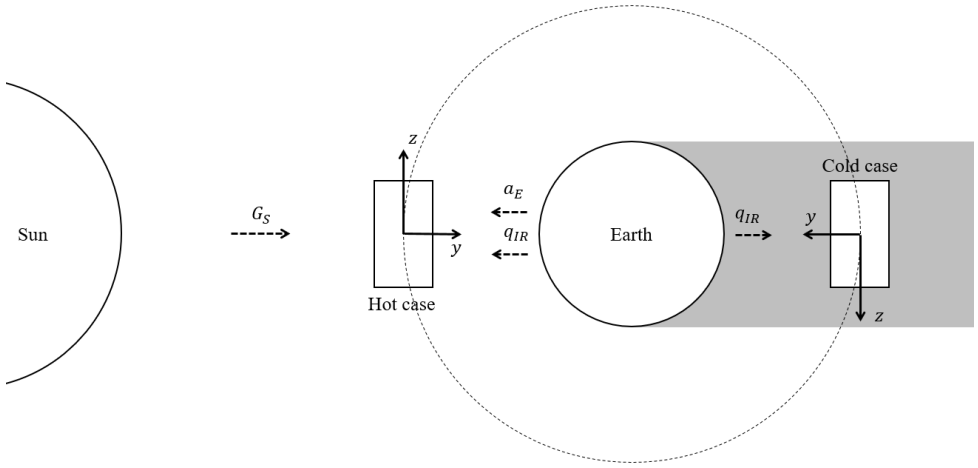

Figure 4.4: Hot and cold case configurations.

The radiation fluxes that reach the satellite surfaces, namely solar flux q_S, the Earth's infrared radiation flux q_E and the albedo radiation flux q_A, need to be computed using Eqs. 4.2, 4.3 and 4.7, respectively, and given as an input for each radiative element in the model. As explained in Sec. 4.1.1, the radiation fluxes are dependent on the position with regard to the Sun (view factors) and on the materials' thermal-optical properties. In Tab. C.2, the radiation fluxes computed are presented for each satellite surface and material.

To simulate the space environment temperature, TEMPD card is used and set to 3 K.

4.2.4 Mesh Refinement

To define the density of elements present in the mesh, a convergence study is performed. The procedure outlined in Sec. 3.2.4 was followed: initial element size was set, results from the analysis are obtained and the maximum node temperature value is registered, the position of the previous node is taken as the reference value for the following iterations, and the number of elements is increased until the value of temperature is converged. The design used for this convergence study was also the satellite with 2 mm thickness aluminium side panels.

In Fig. 4.5, the steady state heat transfer analysis mesh convergence is presented. The analyses computation times is also depicted. As can be seen, with the increase number of elements in the model a substantial increase in the computational time is obtained. Reaching a difference of 10 hours from a model with 5831 to one with 18956 elements. Therefore, since convergence is already attained in the model with 5831 elements, it was chosen as the final one.

Fig. 4.6, presents the hot and cold case temperatures results for the converged thermal FEM aluminium model. One of the satellite's side panels was made transparent to allow the visualization of the internal components.

4.3 Thermal Optimization Design Process

Once the thermal FEM model is complete, the thermal optimization design process can be conducted.

To conduct the thermal optimization design process, an analogous procedure to the one used in the structural

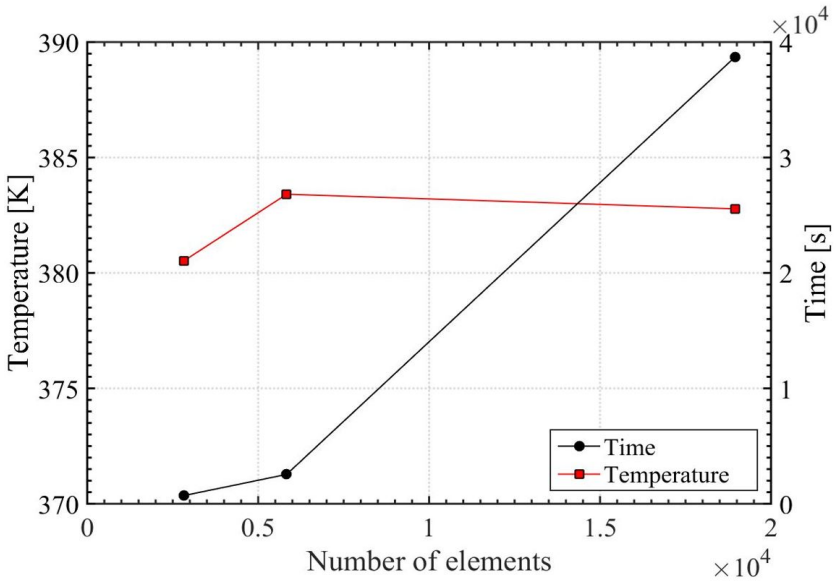

Figure 4.5: Thermal static analysis mesh convergence results.

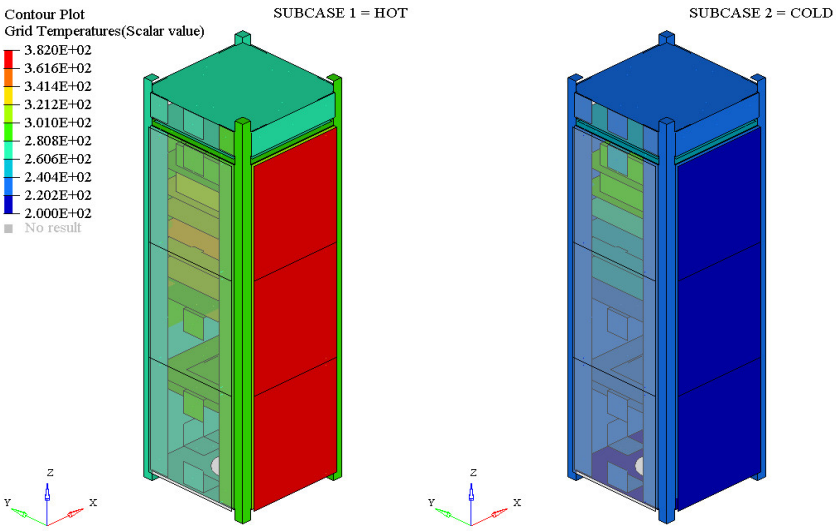

Figure 4.6: Hot and cold case temperature static thermal analysis results for the aluminium design (units in Kelvin).

optimizations was applied: the static thermal analyses were conducted for the two worst cases defined in Sec. 4.2.3 and the results obtained. If the laminated composite materials designs present at most the same number of components complying with their operational temperatures as the aluminium one, the cycle is dismissed, if not the laminates are revised and updated. Additionally, the composite material panels shall have a temperature gradient similar to that of the aluminium ones, as defined in the requirements in Sec. 4.1.2. So, two different assessments must be made:

1. The critical components, i.e. the components that do not comply with their operational temperatures, must be identified in each design, and the properties that influence their temperatures determined;

2. The thermal gradients of the side panels must be analysed.

The starting point of this process were the three updated laminated composite materials obtained from the

structural optimization design process (Sec. 3.3). As stated, the selected materials were:

- Number 3.1): CFRP with aluminium core and total thickness of 1.15 mm, each FRP lamina with 0.25 mm;
- Number 7.1): CFRP with pyrolytic graphite core and total thickness of 1.3 mm, each FRP lamina with 0.3 mm;
- Number 16.1): GFRP with pyrolytic graphite core and total thickness of 1.7 mm, each FRP lamina with 0.4 mm.

However, firstly the thermal behaviour of the aluminium design must be discovered.

In Fig. 4.7, the hot and cold cases minimum and maximum temperatures and the temperature gradients of each satellite component can be observed for the converged aluminium design. The components' operating temperature ranges are also present. If the minimum and maximum temperatures registered comply with the operational ranges, their status is assumed to be "OK", otherwise their status is "NOT OK". All structures are assumed to withstand temperatures ranging from -100 °C to 100 °C. The components identification names are in accordance with the surfaces' IDs from Fig. C.1. Detailed information on the temperatures achieved can be consulted in Tab. D.1.

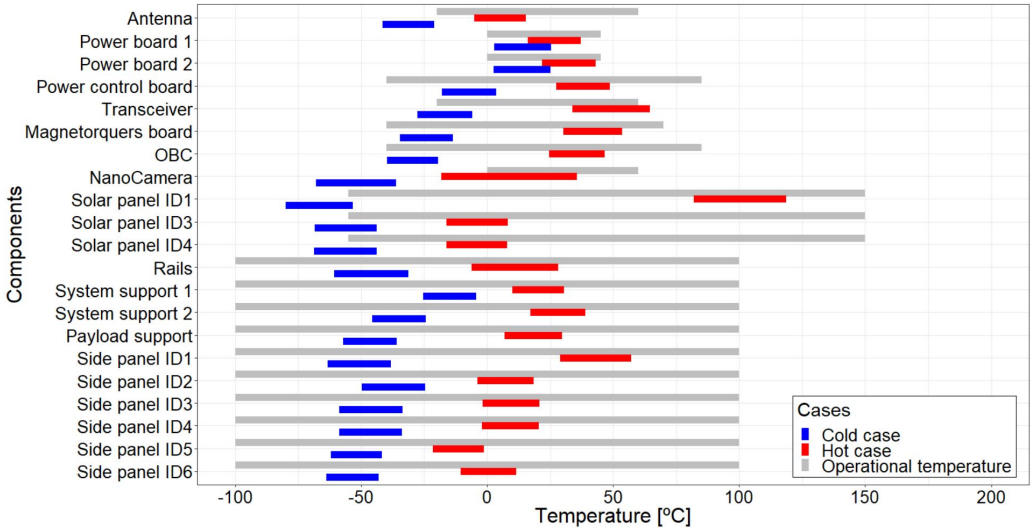

Figure 4.7: Operating ranges, minimum and maximum temperatures and temperature variation in each component for the aluminium design.

According to the results, for the hot case the transceiver exceeds its maximum operational temperature and the nanocamera its minimum operational temperature. In the cold case several components have a minimum temperature that falls below their minimum operating temperature. From the results, it can also be verified that in the hot case the hottest temperature is achieved by the solar panel ID1, which reaches a maximum temperature of 118.65 °C. In the cold case, the minimum temperature achieved is -79.85 °C by the same component.

One of the reasons that can explain the extreme temperatures reached is the nature of the analysis itself, i.e. steady state analysis, which does not represent a real orbiting satellite, that is constantly being heated and cooled down during its orbit and, therefore, the satellite may not reach temperatures as high and/or as low as the ones obtained in the steady state analysis. Furthermore, it should be noted that the maximum and minimum temperatures presented include an uncertainty margin of ± 10 °C to account for inaccuracies in the FEM model (Sec. 4.1.2).

Regarding, the composite laminate designs 3.1), 7.1) and 16.1), two distinct analyses were performed: in the first analysis the laminates composite materials were considered to have an equal absorptivity and emissivity as the aluminium, $\alpha = 0.14$ and $\varepsilon = 0.84$. Whereas, in the second analysis, the respective FRP absorptivity and emissivity mean values were used (Tab. 2.2): for CFRP $\alpha = 0.8$ and $\varepsilon = 0.7$; for GFRP $\alpha = 0.3$ and $\varepsilon = 0.85$.

In Fig. 4.8, the components' extreme temperatures of each satellite component can be observed for the laminates nº 3.1), 7.1) and 16.1), with $\alpha = 0.14$ and $\varepsilon = 0.84$. As can be seen, the components that exceed their operational temperatures are the same as in the aluminium design for both extreme cases, hot and cold. For detailed information consult Tabs. D.2, D.3 and D.4.

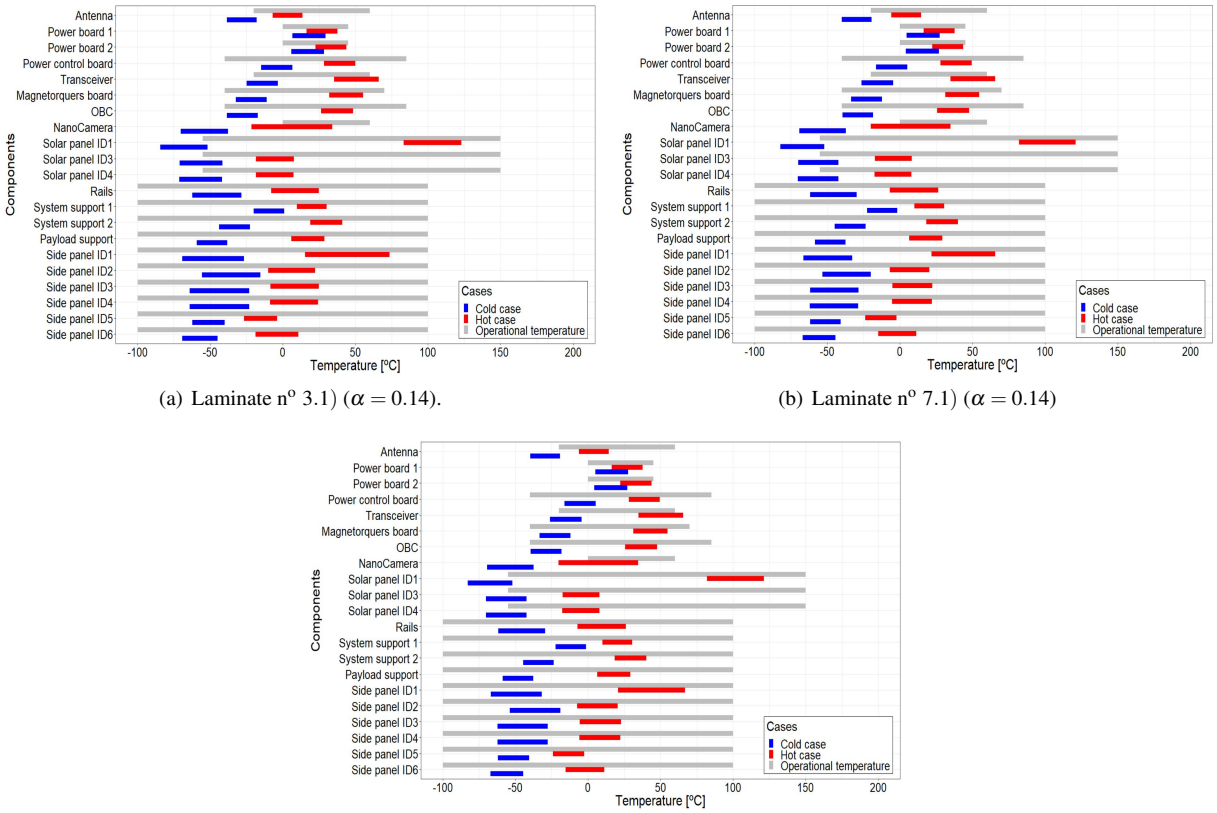

(a) Laminate nº 3.1) ($\alpha = 0.14$).

(b) Laminate nº 7.1) ($\alpha = 0.14$)

(c) Laminate nº 16.1) ($\alpha = 0.14$)

Figure 4.8: Operating ranges, minimum and maximum temperatures and temperature variation in each component for the laminate design nº 3.1), 7.1) and 16.1) ($\alpha = 0.14$).

Fig. 4.9 shows the results obtained for the laminates nº 3.1), 7.1) and 16.1) with the respective FRP absorptivity and emissivity values.

In this analysis, the components' temperature of laminates designs nº 3.1) and 7.1) suffers drastic changes when compared with the aluminium design, specially in the hot case. In the hot case, a temperature mean increase of 20 ºC is obtained and the majority of the electronic components work near their maximum operating temperature and not only two, as in the aluminium design, but four components do not comply with their operational temperature ranges. Regarding, the laminate nº 16.1) an increase in its temperature is also observed and even though the increase is smaller, three components do not comply with their operational requirements. As for the cold case, similar temperatures are achieved in all laminate designs. Tabs. D.5, D.6 and D.7 show detailed information on the temperatures results of each design.

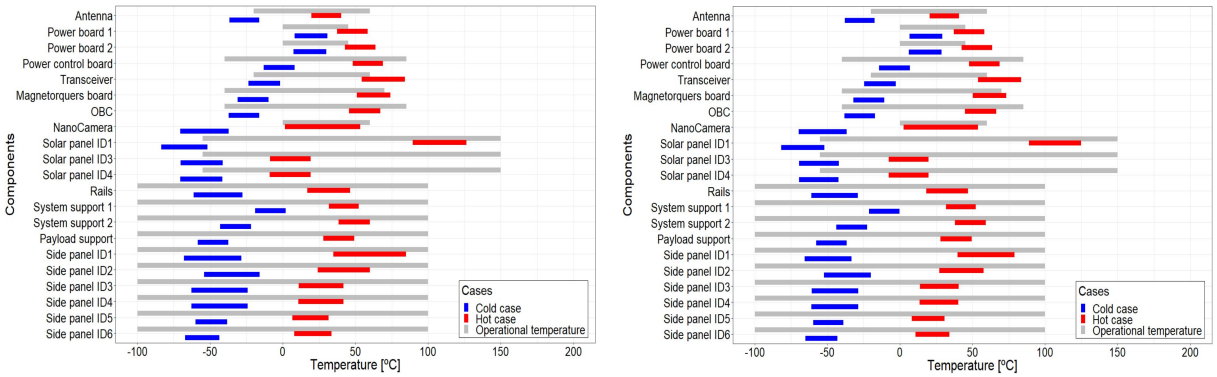

(a) Laminate nº 3.1) ($\alpha = 0.8$).

(b) Laminate nº 7.1) ($\alpha = 0.8$)

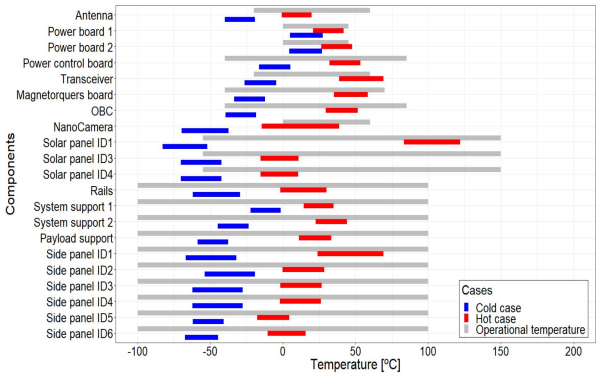

(c) Laminate nº 16.1) ($\alpha = 0.3$)

Figure 4.9: Operating ranges, minimum and maximum temperatures and temperature variation in each component for the laminate design nº 3.1), 7.1) and 16.1), with the respective FRP absorptivity.

To better assess the effect of the side panels thermo-optical properties on the components temperatures Figs. 4.10, 4.11 and 4.12 were created. In these figures, the minimum and maximum temperatures achieved by the structure side panel ID1 and by the antenna in function of the absorptivity of the panels for the laminates nº 3.1), 7.1) and 16.1) are presented. The minimum and maximum temperature for the aluminium design are also presented. Due to legibility reasons, only the temperatures of the side panel with ID1 and the antenna temperatures are depicted. However, it must be noted that the same behaviour in function of the absorptivity is achieved for all the other electronic components and structures.

From the figures, it can be clearly concluded that the absorptivity of the panels dictate the temperatures achieved by the components. The increase in the materials' absorptivity leads to an increase in the components temperature, therefore the temperatures achieved by the laminates with $\alpha = 0.8$ (nº 3.1) and 7.1)) are higher, than the laminate with $\alpha = 0.3$ (nº 16.1)).

Regarding the laminates nº 3.1) and 7.1) the increase in temperatures is higher for the hot case, reaching a mean value of 15.3 ºC for the side panels and 26.8 ºC for the antenna. For the cold case, the increase in temperature, approximately 1.95 ºC, can be neglected. The same behaviour is observed for laminate nº 16.1), however since the absorptivity is lower than the previous laminates the increase in temperatures is also lower: in the hot case it reaches a mean value of 2.8 ºC for the side panels and 5.2 ºC for the antenna, and in the cold case the increase is approximately 0 ºC. The differences between the hot and cold cases were expected, since the fluxes received by the satellite during the cold case are only due to the Earth's infrared, and, therefore, the increase in the flux

received is much smaller than in the hot case (Tab. C.2).

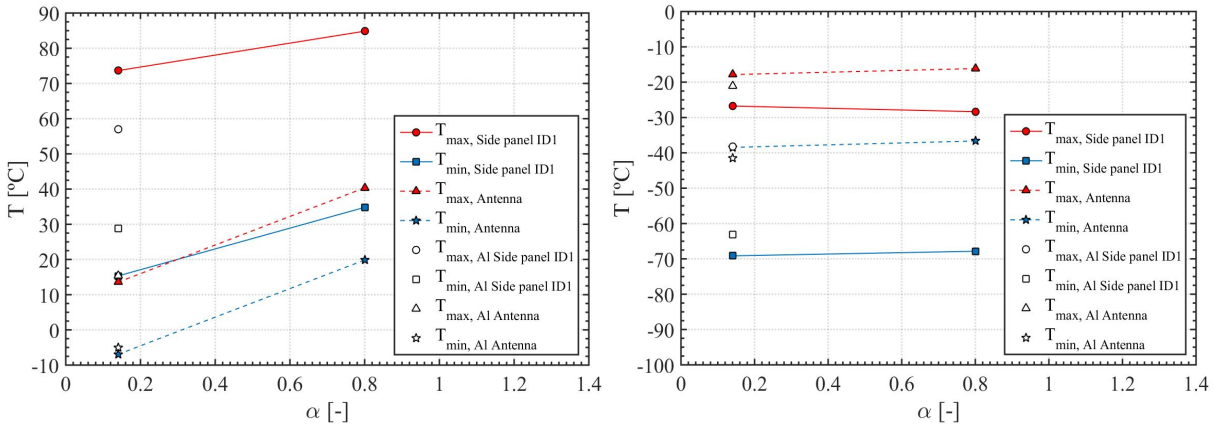

(a) Hot case. (b) Cold case.

Figure 4.10: Maximum and minimum temperatures in function of the panels' absorptivity for laminate nº 3.1) design.

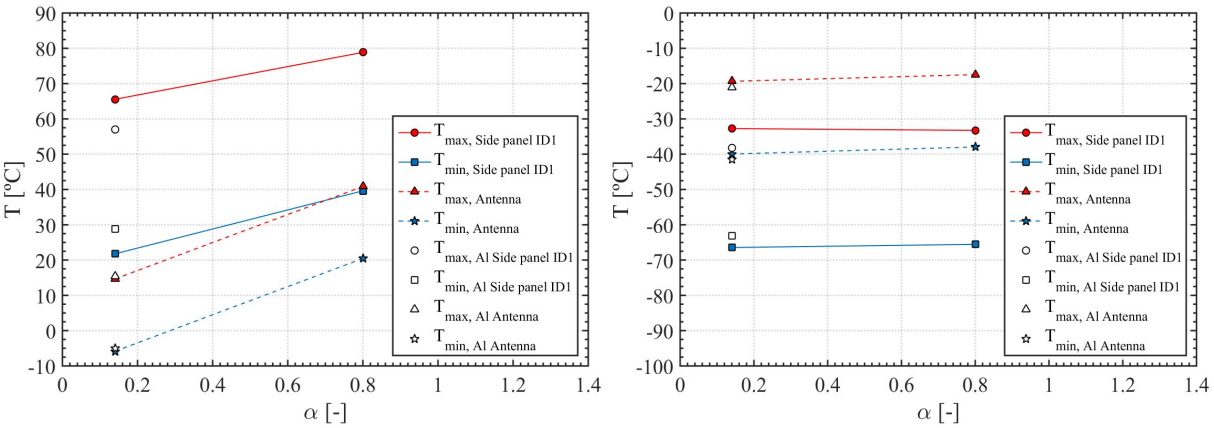

(a) Hot case. (b) Cold case.

Figure 4.11: Maximum and minimum temperatures in function of the panels' absorptivity for laminate nº 7.1) design.

Since the influence of the thermo-optical properties on the satellite temperatures is already known, the respective FRP absorptivity values will be considered for the following analysis (CFRP $\alpha = 0.8$, GFRP $\alpha = 0.3$).

Regarding the thermal gradients of the composite laminate panels, from Tabs. D.5, D.6 and D.7 it can be observed that these three laminates present higher thermal gradients than the aluminium design (Tab. D.1), which do not meet the requirement of equal thermal gradient as the aluminium panels. In an attempt to decrease the thermal gradients, higher conductivity materials must be used and, therefore, the laminates designs need to be revised. Hence, the thickness of the high thermal conductivity laminae, i.e. pyrolytic graphite layer in composites number 3.1) and 7.1) and the aluminium layer in composite nº 16.1), were gradually increased, until they reached a thermal gradient similar to the aluminium design.

Tab. 4.5 presents these three laminates and some of the new laminates equivalent single layer thermal conductivities created and the respective side panel ID1 thermal gradients for the hot and cold cases achieved. To

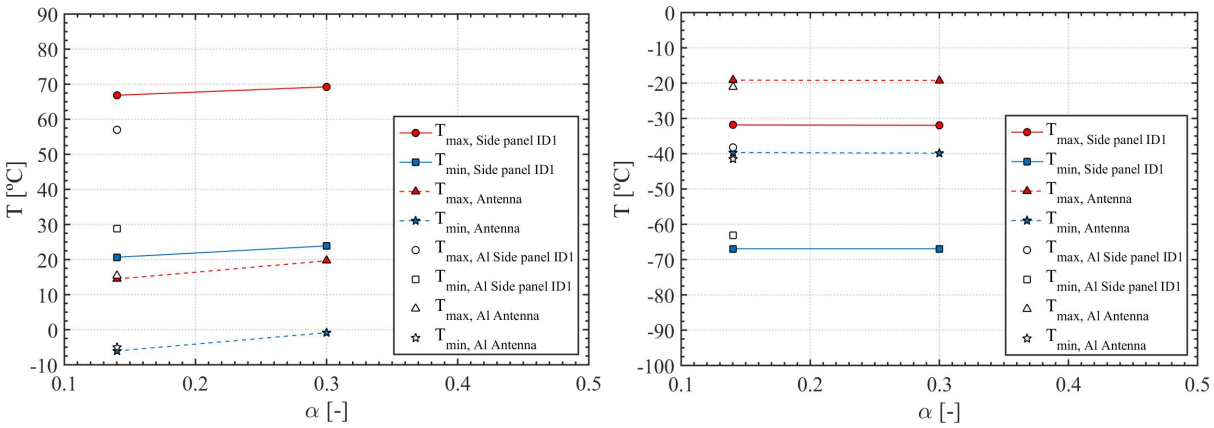

(a) Hot case.

(b) Cold case.

Figure 4.12: Maximum and minimum temperatures in function of the panels' absorptivity for laminate nº 16.1) design.

ease the visualization of the gradients evolution, Fig. 4.13 depicts the maximum thermal gradients obtained for the satellite's side panel ID1 of the previous composite laminate designs. It can be clearly seen that with the increase of the panels thermal conductivities, the thermal gradients decreased.

Table 4.5: Laminates' equivalent thermal conductivity and respective side panel (ID1) thermal gradient for the hot and cold cases.

Material	Laminate #	t*K [mW/K]	Hot case ΔT [ºC]	Cold case ΔT [ºC]
Aluminium design		334.0	28.20	24.90
CFRP	3.1	45.40	50.00	39.50
Aluminium core	3.2	62.10	45.00	36.00
	3.3	304.3	28.50	25.40
CFRP	7.1	94.40	39.20	32.30
Pyrolytic graphite core	7.2	164.4	32.90	28.40
	7.3	304.4	28.00	25.10
GFRP	16.1	71.10	45.40	35.00
Pyrolytic graphite core	16.2	141.2	35.90	29.60
	16.3	351.2	27.80	24.80

The laminates which meet the thermal gradient requirements were the following hybrid structures:

- Number 3.3): CFRP with aluminium core of 1.7 mm thickness and total thickness of 2.7 mm. Each FRP lamina with 0.25 mm;
- Number 7.3): CFRP with pyrolytic graphite core of 0.4 mm thickness and total thickness of 1.6 mm. Each FRP lamina with 0.3 mm;
- Number 16.3): GFRP with pyrolytic graphite core of 0.5 mm thickness and total thickness of 2.1 mm. Each FRP lamina with 0.4 mm.

Tab. 4.6 shows the updated designs structural mass reduction.

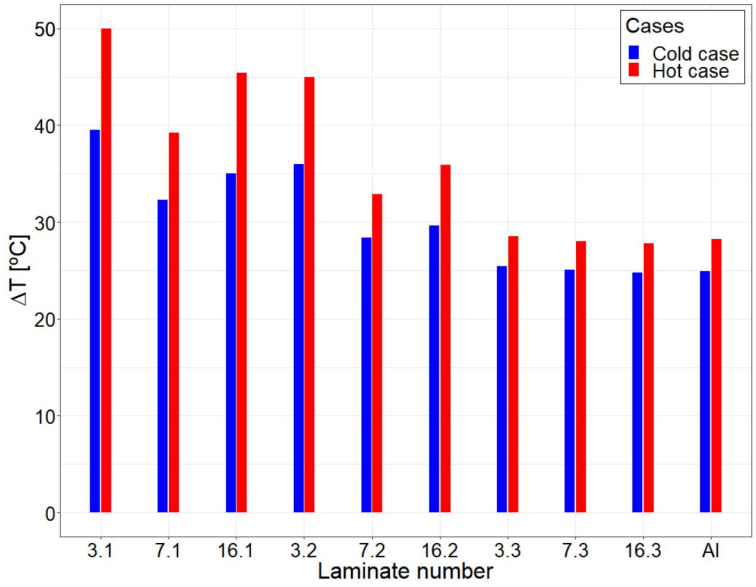

Figure 4.13: Thermal gradients of updated composite laminate designs.

Although, the thermal gradient requirement is met by all three, a 14.5% increase in each panel mass is obtained for laminate nº 3.3). Therefore, only laminates nº 7.3) and 16.3) are valid candidates.

Table 4.6: Thermal optimized laminates' structural mass reduction for each side panel.

Designs	Structural mass reduction [%]
Laminate nº 3.3)	-14.6
Laminate nº 7.3)	58.1
Laminate nº 16.3)	35.8

Up until this point, the influence of the thermal-optical properties on the satellite components was assessed and the thermal gradient requirement was met by the valid candidates. However, with these new laminates, it is necessary to evaluate the effect of the increase of thermal conductivity on the structure side panels and components temperature.

In Figs. 4.14 and 4.15, the maximum and minimum temperature achieved by the side panels and components in function of the laminates thermal conductivity are presented. Due to legibility reasons, only the temperatures of the side panel with ID1 and the antenna temperatures are depicted, which are, nonetheless, representative of the behaviour of all other structures and components.

It can be concluded that the antenna temperature changes slightly with the increase of the panels' thermal conductivity for the hot and cold cases, with a maximum of 2 ºC. In contrast, on the side panels a change up to approximately 10 ºC is reached and, in accordance with Fig. 4.13, the maximum and minimum structure temperatures tend to decrease their difference in both cases, i.e. decreasing the thermal gradient.

From the figures it can also be clearly seen the difference between the aluminium design temperatures and the laminates designs. As previously observed, in the hot case the laminates present higher mean values than the aluminium, due their higher absorptivity value, whereas in the cold case the difference between the designs is almost null. In the hot case, an average temperature difference of 20 ºC and 5 ºC is observed for the CFRP and GFRP laminate designs, respectively, when compared with the aluminium design temperatures. The temperature

difference between the CFRP and GFRP was also expected since GFRP presents a smaller absorptivity than CFRP.

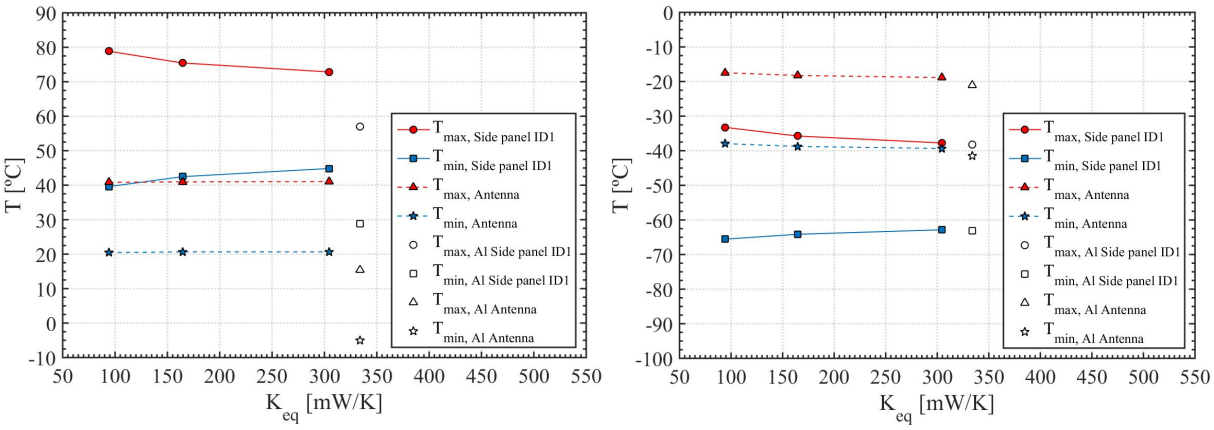

(a) Hot case. (b) Cold case.

Figure 4.14: Maximum and minimum temperatures in function of the panels' thermal conductivity for laminates with CFRP and pyrolytic graphite core design.

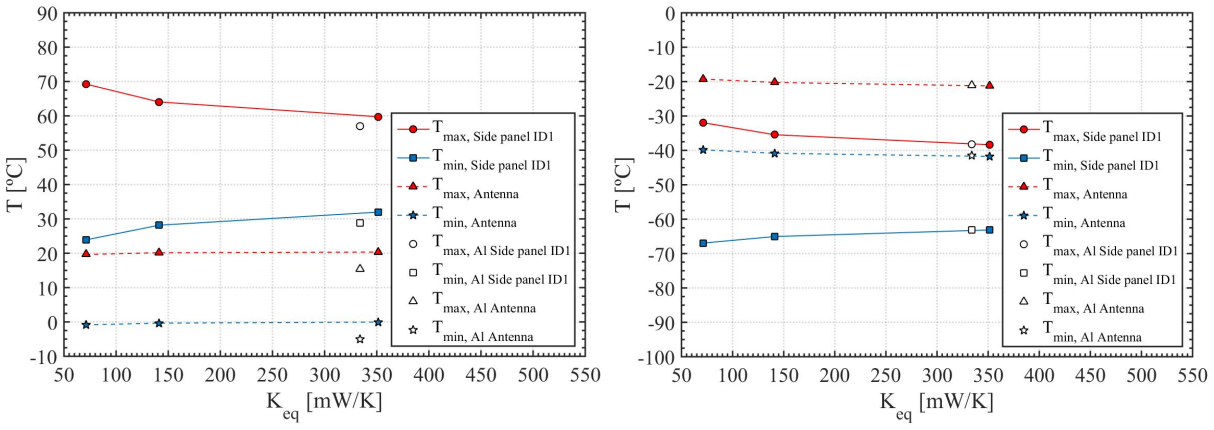

(a) Hot case. (b) Cold case.

Figure 4.15: Maximum and minimum temperatures in function of the panels' thermal conductivity for laminates with GFRP and pyrolytic graphite core design.

Taken into account all the analyses performed, it can be said that, for the satellite being studied, the thermal conductivity of the side panels does not influence the temperature of its components. The main responsible for the components' temperature is the panels absorptivity, as evidenced in Figs. 4.11 and 4.12. Therefore, in order to meet the thermal requirements, a coat of paint with a similar absorptivity as the aluminium can be added to the laminate.

Figs. 4.16 (a) and (b) present the maximum and minimum temperatures and the temperature gradients of each satellite component for the optimized composite laminate designs nº 7.3) and 16.3), respectively. See Tabs. D.8 and D.9 for detailed information.

Following the thermal analysis, the linear static and normal mode analysis must be conducted for the updated laminates, to ensure the laminates meet the structural requirements as well. In the following chapter the thermo-structural results are presented.

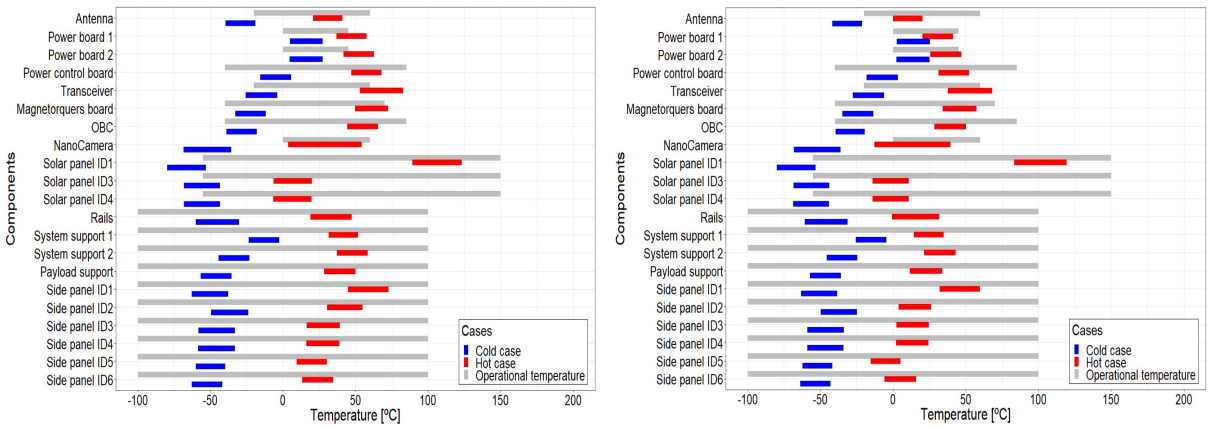

(a) Laminate nº 7.3) ($\alpha = 0.8$)

(b) Laminate nº 16.3) ($\alpha = 0.3$)

Figure 4.16: Operating ranges, minimum and maximum temperatures and temperature variation in each component for the thermal optimized laminate designs nº 7.3) and 16.3).

Chapter 5

Thermo-Structural Analysis, Results and Discussion

In the current chapter the optimization design cycle is finalized: the static linear and normal mode analysis are performed for the updated composite laminates from the thermal optimization design cycle made in Sec. 4.3 and the thermal results obtained are recalled.

A discussion on the final results is performed.

5.1 Thermo-Structural Optimization Final Design

In Sec. 4.3, two optimized composite laminates were obtained from the thermal optimization design cycle. However the new materials must be analysed from a structural point of view, to ensure the structural requirements are met. Therefore, the same analyses performed in Sec. 3.3 are now presented for the new materials. Recalling the optimized materials:

- Number 7.3): CFRP with pyrolytic graphite core of 0.4 mm thickness and total thickness of 1.6 mm. Each FRP lamina with 0.3 mm;
- Number 16.3): GFRP with pyrolytic graphite core of 0.5 mm thickness and total thickness of 2.1 mm. Each FRP lamina with 0.4 mm.

In Tab. 5.1 the computed MOS for the critical components in each load case are presented, for these two composite laminate designs. Once more, the critical components are the systems supports for all designs and the worst case scenario the load case B. However, for all cases the structural requirement MOS$\geq$ 0 (Eq. 3.1) is met and, therefore, the components do not fail, presenting a similar behaviour as the satellite with the aluminium panels.

Regarding the side panels, the extreme failure indexes computed for each of the new materials are presented in Tab. 5.2. The composite materials requirement, i.e. failure index smaller than 1 (Eq. 3.10), is attained for all load cases.

One last assessment must be made concerning the linear static analysis results: the bolts' MOS. Tab. 5.3 shows the bolts' minimum MOS_A, MOS_S and MOS_I computed for each load case and side panel material, using the

Table 5.1: Updated critical components' MOS.

Cases	Aluminium	Laminate nº 7.3)	Laminate nº 16.3)
A	3.00	3.29	3.19
B	1.93	2.10	2.03
C	14.19	15.05	14.58
D	14.18	15.04	14.57
E	29.18	23.60	22.62
F	29.00	23.56	22.62
Component		System support	

Table 5.2: Updated maximum failure index of the satellite's side panels.

	Failure index	
Cases	Laminate nº 7.3)	Laminate nº 16.3)
A	2.39E-01	1.88E-01
B	3.29E-01	2.58E-01
C	6.90E-02	5.44E-02
D	6.92E-02	5.45E-02
E	6.32E-02	4.41E-02
F	6.30E-02	4.41E-02

equations presented in Sec. 3.3. The full extension of designs meet the requirement MOS≥ 0.

All the requirements, regarding the linear static analysis are met, hence normal mode analysis is subsequently conducted for these two laminates.

Tab. 5.4 show the updated laminates fundamental frequencies, and, as can be seen, all designs also meet the 115 Hz goal.

Since, the structural requirements are met and, as the new laminates present an identical structural behaviour as the aluminium panel, the laminates do not need to be revised. Hence, the thermal analysis does not need to be conducted again, being the results obtained in Sec. 4.3 maintained for these laminates.

Regarding the laminated composite materials thermal properties, one should note that both laminates present similar thermal conductivities and, therefore, both meet the thermal gradient requirements. However, these laminates have different absorptivity values than the aluminium design and, remembering the thermal analysis results from Sec. 4.3, it was concluded that the absorptivity is the main thermal property that defines the temperature of the satellite's components. Higher absorptivity values are linked with higher temperatures in the hot case, as could be seen in Figs. 4.16 (a) and (b) and complemented by Tabs. D.1, D.8 and D.9. Due to that laminates nº 7.3) and 16.3) present more components that do not comply with their operational temperature than the aluminium design. As for the cold case, since temperatures change slightly with the absorptivity of the side panels, similar temperatures were achieved for all designs.

Taking the previous information into account, for an operating mode, neither of the materials comply with the requirements, i.e. presenting an identical response as the aluminium design. Therefore, a coat of paint with an identical absorptivity as the aluminium can be added to the laminates so that similar temperatures could be attained.

Nevertheless, although the manufacturers did not present the components' survival temperature ranges, from

Table 5.3: Updated minimum bolts' MOS of the linear static analysis.

Cases	MOS	Aluminium	Laminate n^o 7.3)	Laminate n^o 16.3)
A	MOS_A	21.40	15.52	14.89
	MOS_S	4.05	4.81	4.67
	MOS_I	4.05	4.77	4.62
B	MOS_A	15.10	10.96	10.51
	MOS_S	2.64	3.21	3.11
	MOS_I	2.64	3.18	3.06
C	MOS_A	85.47	34.31	33.42
	MOS_S	16.78	19.45	18.92
	MOS_I	16.78	19.33	18.74
D	MOS_A	85.17	35.10	34.15
	MOS_S	17.42	19.88	19.32
	MOS_I	17.42	19.70	19.06
E	MOS_A	103.11	88.87	90.19
	MOS_S	47.89	51.49	52.35
	MOS_I	47.71	51.49	52.35
F	MOS_A	103.28	89.06	90.43
	MOS_S	49.17	51.57	52.44
	MOS_I	48.40	51.57	52.44

Table 5.4: First natural frequencies of the thermal optimized laminates.

Mode	Natural frequency [Hz]	Aluminium	Laminate n^o 7.3)	Laminate n^o 16.3)
1	f_1	9.24E-04	8.61E-04	9.59E-04
2	f_2	7.35E-04	6.95E-04	5.23E-04
3	f_3	5.22E-04	4.95E-04	2.11E-04
4	f_4	3.96E-04	5.01E-04	8.29E-05
5	f_5	1.85E-04	6.16E-04	5.63E-04
6	f_6	5.65E-04	8.61E-04	6.05E-04
7	f_7	182.28	185.77	167.80
8	f_8	182.47	186.74	169.38
9	f_9	190.71	189.00	171.52
10	f_{10}	208.11	198.72	181.34

state of the art evaluations performed it could be concluded that most components present a survival temperature range of -55 ^{o}C to 120 ^{o}C. Therefore, in all designs previously presented, for a non operating mode, all components would survive in the hot case and, only the solar panels and nanocamera would not in the cold case.

Since this work purpose was to assess composite materials as alternatives for the aluminium side panels and not to validate the satellite's TCS, only some suggestions to implement in its TCS are made, to ensure that all components would remain in their operational temperature ranges. Since the thermal design is driven by a limited mass and power budget, passive methods should be implemented. Thus, to increase the temperature of the satellite in the cold case, some components could be linked through thermal straps to the battery heater. Additionally, an isolating material on those components could be added, as aerogel, which is characterized by its low mass and low conductivity. Regarding, the hot case thermal straps could also be used, linking the components with high temperature to the surfaces or components that present lower temperatures.

So far both laminates present a similar structural and thermal behaviour. However, laminate n^o 7.3) allows a

further 22.3% and 58.1% reduction of each panel mass, when compared with the laminate n^{o}16.3) and with the aluminium design, respectively. Therefore, since the reduction of the structural mass of the satellite is aimed, the CFRP with pyrolytic graphite core of 0.4 mm thickness and total thickness of 1.6 mm is the laminated composite material selected between the two.

Event though, a coat of paint must be added to this laminate, a 58.1% structural mass reduction of each panel is an improvement comparing to the aluminium design. Considering a coat of paint with a density of 1.5 g/cm^3 and 1 mm thickness, the side panels mass would increase approximately 10%, which for the laminate selected a mass reduction of 48% would still be attained. The panel's mass reduction would then be translates in approximately 300 g that could be used in additional/different payloads or components. It can be concluded that laminates can offer big reductions of the structural mass without compromising the structural and thermal performance of the satellite. However, it must be noted that only by inserting a high thermal conductivity core within the FRP it is possible to achieve all the thermal conductivity requirements.

In Figs. 5.1, 5.2 and 5.3, the MOS and failure indexes, the normal modes and the thermal results for the final optimized laminate can be observed, respectively.

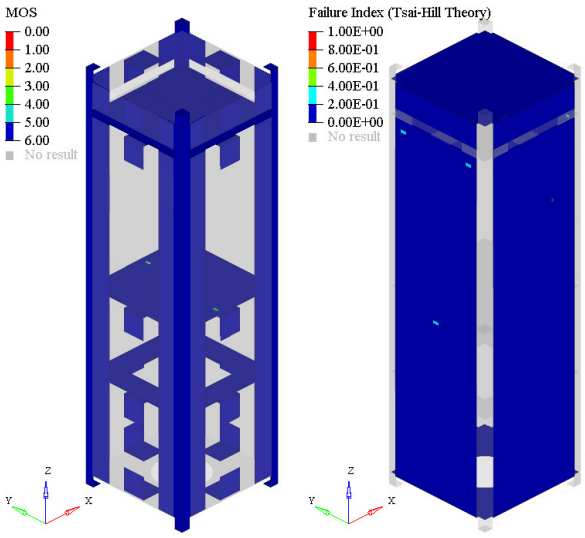

Figure 5.1: MOS and failure index FEM results of laminate nº 7.3) design for load case B.

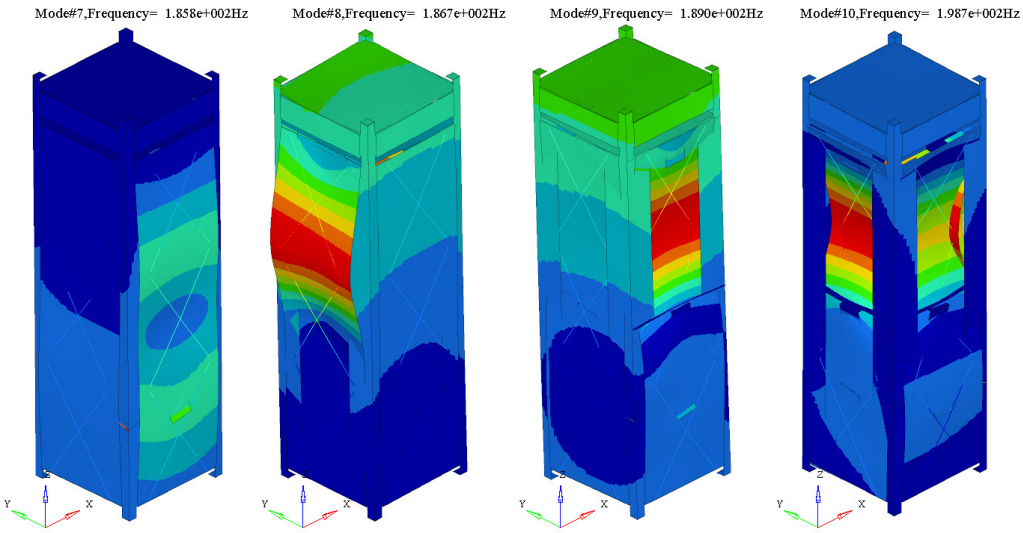

Figure 5.2: First four vibration modes of laminate nº 7.3) design.

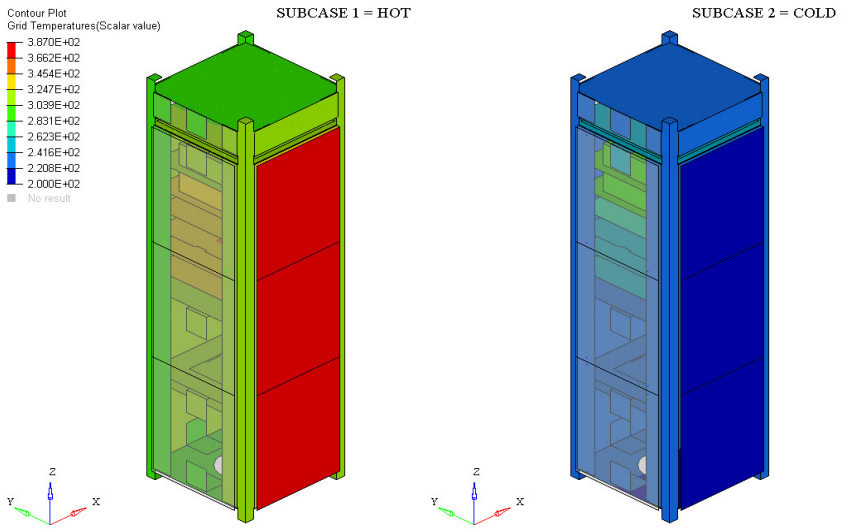

Figure 5.3: Hot and cold case temperature thermal analysis results for laminate nº 7.3) design (units in Kelvin).

Chapter 6

Conclusions and Future Work

This concluding chapter gives an overview of the main lessons of this thesis and what has been learnt in the process. A brief discussion of future work is also presented.

6.1 Conclusions

The main goal of this thesis was to assess if laminated composite materials could be a viable alternative to the typical aluminium side panels of a CEiiA's 3U CubeSat, with the purpose to reduce the structural mass of the satellite, without loss of structural and thermal performance.

In order to accomplished that goal, 18 hybrid structures with laminae of CFRP and GFRP intercalated with laminae with high thermal conductivity (aluminium, pyrolytic graphite or copper mesh) with distinct stacking schemes were designed. Among these laminates, three were selected as the baseline for the present work. The composites with lightweight, good mechanical properties and high thermal conductivity were preferred and a matrix decision was devised. The composite laminates to be further analysed were:

- Number 3): CFRP with aluminium core and total thickness of 0.75 mm;
- Number 7): CFRP with pyrolytic graphite core and total thickness of 0.7 mm;
- Number 16): GFRP with pyrolytic graphite core and total thickness of 0.7 mm,

which represented a structural mass reduction of 74.7%, 80.6% and 77.3% on each panel, respectively.

Once selected the composite laminates, linear static analysis and normal mode analysis were carried out. The respective FEM models were created to enable the simulation and analysis of the linear static and dynamic behaviour of the satellite, with the previous composite laminates as their side panels. The initially proposed laminates did not attained the required dynamic behaviour, and structural optimized composite laminates had to be created until the requirements were meet. The three new proposed designs were:

- Number 3.1): CFRP with aluminium core and total thickness of 1.15 mm, each FRP lamina with 0.25 mm;
- Number 7.1): CFRP with pyrolytic graphite core and total thickness of 1.3 mm, each FRP lamina with 0.3 mm;

- Number 16.1): GFRP with pyrolytic graphite core and total thickness of 1.7 mm, each FRP lamina with 0.4 mm.

With these structural optimized laminates, to evaluate the thermal performance of the satellite, the thermal FEM model was created and the components' temperature and panels' thermal conductivity compared with the aluminium design ones'. However, none of these laminates meet the requirements, thus thermal optimizations were also performed. Among the laminates that meet the thermal requirements, one of them was excluded as a valid candidate, since it represented a 14.6% increase in each side panel structural mass. The new optimized laminates were:

- Number 7.3): CFRP with pyrolytic graphite core of 0.4 mm thickness and total thickness of 1.6 mm. Each FRP lamina with 0.3 mm;
- Number 16.3): GFRP with pyrolytic graphite core of 0.5 mm thickness and total thickness of 2.1 mm. Each FRP lamina with 0.4 mm.

From these laminates a distinction between the effect of the thermal conductivity of the panels and its absorptivity values on the component's temperature was identified. The results show that the absorptivity of the panels dictates the components' temperature, whereas the thermal conductivity determines the thermal gradients of the panels. Therefore, only by adding a coat of paint with a proper absorptivity to the previous laminates, the components temperatures of the satellite studied can be adjusted.

The structural behaviour of these laminates was finally assessed and meet all the requirements. Taking all this into account, it was concluded that hybrid laminates can offer a viable alternative to the usual aluminium design, with major advantages as structural mass is concerned. However, since the main goal of this thesis is to reduce the satellites structural mass, the hybrid composite laminate that presented the higher structural mass reduction was selected as the final optimized solution. This laminate was the CFRP with pyrolytic graphite core of 0.4 mm thickness and total thickness of 1.6 mm, allowing a 58.1% of structural mass reduction on each panel.

6.2 Future Work

The next step in this work would be to perform structural and thermal transient analyses, so that the behaviour of laminated composite materials to transient loads could be analysed. Still regarding the FEM models, more detailed models could be created, so that the error associated with the simplifications made could be assessed and, if possible, minimized further.

Since this thesis was a preliminary study on composite materials, their thermal expansion was not taken into account, therefore, in future analysis it must be a property that should be analysed and their effect on the structural behaviour of the satellite analysed. Another aspect that was not included in the preliminary analysis was the conductive links between the components, which were considered as perfect. Experimental studies must be performed so that the conductance behaviour between components could be determined.

The properties of the laminated composite materials should also be experimentally assessed, since some of its properties were computed using mathematical methods and other based on information available on literature. Additionally, other composite materials could be studied as possible solutions.

Bibliography

[1] M. N. Sweeting. Modern small satellites-changing the economics of space. *Proceedings of the IEEE*, 106 (3):343–361, 2018.

[2] O. Acker, F. Potscher, and T. Lefort. Why satellites matter: The relevance of commercial satellites in the 21st century - a perpective 2012-2020. *Booz & Company*, 2019.

[3] B. Battrick et al. The impact of space activities upon society. *The European Space Agency, The International Academy of Astronautics, no. 237, ESA Publications Division - ESTEC*, 2015.

[4] A. Poghosyan and A. Golkar. CubeSat evolution: Analyzing CubeSat capabilities for conducting science missions. *Progress in Aerospace Sciences*, 88:59–83, Jan. 2017. doi: 10.1016/j.paerosci.2016.11.002.

[5] R. Sandau, K. Brieß, and M. D'Errico. Small satellites for global coverage: Potential and limits. *ISPRS Journal of Photogrammetry and Remote Sensing*, 65(6):492–504, nov 2010. doi: 10.1016/j.isprsjprs.2010.09.003.

[6] E. Kulu. Nanosatellite & cubesat database, 2019. URL https://www.nanosats.eu. Accessed on 1/04/2019.

[7] R. Nugent et al. The cubesat: The picosatellite standard for research and education, california polytechnic state university. Technical report, 2008.

[8] D. Selva and D. Krejci. A survey and assessment of the capabilities of cubesats for earth observation. *Acta Astronautica*, 74:50–68, 2012.

[9] S. Lee, A. Hutputanasin, A. Toorian, W. Lan, R. Munakata, J. Carnahan, D. Pignatelli, and A. Mehrparvar. Cubesat design specification, rev. 13: The cubesat program. Technical report, San Luis Obispo, California Polytechnic State University, 2014.

[10] Cubesat concept and the provision of deployer services. URL https://eoportal.org/web/eoportal/satellite-missions/content/-/article/cubesat-concept-1. Acessed on 22/04/2019.

[11] Applicable cubesat sizes, 2019. URL https://www.ecm-space.de/index.php/launch-adapters-h/cubesat-sizes. Accessed on 13/04/2019.

[12] W. J. Larson and J. R. Wertz. *Space mission analysis and design*. Kluwer Academic Publisher, 1992.

[13] G. F. Abdelal, N. Abuelfoutouh, and A. H. Gad. *Finite element analysis for satellite structures: applications to their design, manufacture and testing*. Springer Science & Business Media, 2012.

[14] Space enginerering: Spacecraft mechanical loads analysis handbook. ECSS Secretariat, 2013. Document version ECSS-E-HB-32-26A.

[15] J. R. Wertz, D. F. Everett, and J. J. Puschell. *Space mission engineering: the new SMAD*, volume 1. Microcosm Press Hawthorne, CA, 2011.

[16] R. Lagier. Ariane 5: User's manual. *Arianespace, Issue 5 Revision 2*, 2016.

[17] J. J. Wijker. *Spacecraft structures*. Springer Science & Business Media, 2008.

[18] A. Calvin. Spacecraft loads analysis - an overview. ESA/ESTEC, Noordwijk, The Netherlands, 2011.

[19] R. D. Karam. Satellite thermal control for systems engineers. Technical report, American Institute of Aeronautics and Astronautics, Inc., 1998.

[20] T. L. Bergman, F. P. Incropera, D. P. DeWitt, and A. S. Lavine. *Fundamentals of heat and mass transfer*. John Wiley & Sons, 2011.

[21] J. Meseguer, I. Pérez-Grande, and A. Sanz-Andrés. *Spacecraft thermal control*. Elsevier, 2012.

[22] N. R. Council et al. *Technology for small spacecraft*. National Academies Press, 1994.

[23] R. N. Miyake. Spacecraft design thermal control subsystem. 2008.

[24] E. Agasid, R. Burton, R. Carlino, G. Defouw, A. Dono Perez, A. Karacahoglu, B. Klamm, A. Rademacher, J. Schalkwyck, R. Shimmin, et al. Small spacecraft technology state of the art. *NASA, Ames Research Center, Mission Design Division Rept. NASA/TP-2015-216648/REV1, Moffett Field, CA*, 2015.

[25] M. Meftah, A. Irbah, A. Hauchecorne, and J.-F. Hochedez. Picard payload thermal control system and general impact of the space environment on astronomical observations. In *Sensors and Systems for Space Applications VI*, volume 8739, page 87390B. International Society for Optics and Photonics, 2013.

[26] L. Simões. Study of low earth orbit impact on orca2sat subsystems. Master's thesis, Universidade da Beira Interior, University of Victoria, 2018.

[27] V. K. Thakur, M. K. Thakur, and A. Pappu. *Hybrid Polymer Composite Materials: Properties and Characterisation*. Woodhead Publishing, 2017.

[28] R. F. Gibson. A review of recent research on mechanics of multifunctional composite materials and structures. *Composite structures*, 92(12):2793–2810, 2010.

[29] P. K. Mallick. *Fiber-reinforced composites: materials, manufacturing, and design*. CRC press, 2007.

[30] A. P. Mouritz. *Introduction to aerospace materials*. Elsevier, 2012.

[31] Space engineering: Structural materials handbook part 1: Overview and material properties and applications. ECSS Secretariat, 2011. Document version ECSS-E-HB-32-20 Part 1A.

[32] H. Altenbach, J. Altenbach, and W. Kissing. *Mechanics of Composite Structural Elements*. Springer, 2004.

[33] V. L. Pisacane. *Fundamentals of space systems*. Johns Hopkins University/Appli, 2005.

[34] R. D. Jamison, O. H. Griffin, J. A. Ecker, and W. E. Skullney. Use of graphite/epoxy composites in spacecraft structures: A case study. *Johns Hopkins APL Technical Digest, Volume 7, Number 3*, 1986.

[35] V. F. Mazzio and C. H. Bixler. Optimized design and fabrication process for advanced composite spacecraft structures. *American Institute of Aeronautics and Astronautics, Paper No. A79-19616, New York*, 1979.

[36] I. M. Industries. A carbon-fibre satellite. *FLIGHT International*, 1969.

[37] R. Lukez. The use of graphite/epoxy composite structures in space applications. *Morton Thiokol, Inc, Aerospace Group*.

[38] K. Dismukes and J. I. Petty. Payload bay doors. NASA, 2002. URL https://spaceflight.nasa.gov/shuttle/reference/shutref/structure/baydoors.html. Accessed on 5/24/2019.

[39] D. G. Gilmore. *Spacecraft Thermal Control Handbook, Fundamental Technologies, vol. I The Aerospace Press/American Institute of Aeronautics and Astronautics*. Inc, 2002.

[40] E. M. Silverman. Product development of engineered thermal composites for cooling spacecraft electronics. *Northrop Grumman Technology Review Journal*, 13(2):1–19, 2005.

[41] J. Calder and E. Silverman. Development of an aluminium clad carbon composite doubler for spacecraft thermal management. *Society for Advancement of Materials and Process Engineering*, 2004.

[42] J. J. Banisaukas, M. A. Shioleno, C. D. Levan, S. P. Rawal, E. M. Silverman, and R. J. Watts. Carbon fiber composites for spacecraft thermal management opportunities. In *AIP Conference Proceedings*, volume 746, pages 10–21. AIP, 2005.

[43] J. Marcos, M. Segura, J. Antolin, A. Landaberea, F. Lamela, and G. Atxaga. Multifunctional equipment design by using high thermal conductivity fibres. In *Spacecraft Structures, Materials and Mechanical Testing 2005*, volume 581, 2005.

[44] N. M. Teti et al. Eo-1 technology validation report for the carbon-carbon radiators. *Swales Aerospace*, 27, 2001.

[45] M. Montesano. Spacecraft thermal management solutions using annealed pyrolytic graphite. In *49th AIAA/ASME/ASCE/AHS/ASC Structures, Structural Dynamics, and Materials Conference, 16th AIAA/ASME/AHS Adaptive Structures Conference, 10th AIAA Non-Deterministic Approaches Conference, 9th AIAA Gossamer Spacecraft Forum, 4th AIAA Multidisciplinary Design Optimization Specialists Conference*, page 1958, 2008.

[46] I. M. McKinley, C. H. Smith, P. G. Ramsey, and J. I. Rodriguez. Pyrolytic graphite film thermal straps: Characterization testing. *Cryogenics*, 80:174–180, 2016.

[47] R. Birkeland, T. A. Stein, M. Tømmer, M. Beermann, J. Petrasch, and A. Gjersvik. The nuts cubesat project: Spin-offs and technology development. In *Proceedings of the 22nd ESA Symposium on European Rocket and Balloon Programmes and Related Research, ESA Special Publication. ESA*, 2015.

[48] Upsat structural. URL https://upsat.gr/?page_id=34. Accessed on 24/04/2019.

[49] A. Ampatzoglou, A. Baltopoulos, A. Kotzakolios, and V. Kostopoulos. Qualification of composite structure for cubesat picosatellites as a demonstration for small satellite elements. *International Journal of Aeronautical Science & Aerospace Research*, 7(1):1–10, 2014.

[50] T. Sinmazcelik, E. Avcu, M. Ö. Bora, and O. Çoban. A review: Fibre metal laminates, background, bonding types and applied test methods. *Materials & Design*, 32(7):3671–3685, 2011.

[51] M. Thirukumaran, I. Siva, J. W. Jappes, and V. Manikandan. Forming and drilling of fiber metal laminates–a review. *Journal of Reinforced Plastics and Composites*, 37(14):981–990, 2018.

[52] P.-Y. Chang, P.-C. Yeh, and J.-M. Yang. Fatigue crack initiation in hybrid boron/glass/aluminum fiber metal laminates. *Materials Science and Engineering: A*, 496(1-2):273–280, 2008.

[53] J. Hale. Boeing 787 from the ground up 06. *Aeromagazine: Quarter*, 4, 2006.

[54] Space engineering: Structural general requirements. ECSS Secretariat, 2008. Document version ECSS-E-ST-32C Rev.1.

[55] Antenna systems. Technical report, Innovative Solutions In Space B.V., 2019.

[56] Communication systems UHF and VHF band. Technical report, Innovative Solutions in Space B.V., 2019.

[57] NanoPower BP4 datasheet. Technical report, GOMSpace, 2018.

[58] NanoPower battery datasheet. Technical report, GOMSpace, 2018.

[59] NanoPower P31u datasheet. Technical report, GOMSpace, 2019.

[60] User manual: 1U solar panel. Technical report, ENDUROSAT, 2018.

[61] P. S. Systems. Pumpkin CubeSat kit bus compatible OBC. Technical report, 2019.

[62] Magnetorquer board (iMTQ). Technical report, Innovative Solutions in Space B.V, 2019.

[63] NanoCam C1U datasheet. Technical report, GOMSpace, 2017.

[64] Gauss OBC. Technical report, Group of Astrodynamics for the Use of Space Systems, 2017.

[65] MSC Nastran Getting started with MSC Nastran user's guide. MSC Software, 2001.

[66] J. N. Reddy. *Mechanics of Laminated Composite Plates and Shells: Theory and Analysis*. Second edition, 2004.

[67] A. K. Kaw. *Mechanics of Composite Materials*. Second edition, 2006.

[68] J. Reddy and R. Averill. Advances in the modeling of laminated plates. *Computing Systems in Engineering*, 2(5-6):541–555, 1991.

[69] R. Rolfes and U. Hammerschmidt. Transverse thermal conductivity of cfrp laminates: a numerical and experimental validation of approximation formulae. *Composites Science and Technology*, 54(1):45–54, 1995.

[70] I. Tavman. Effective thermal conductivity of isotropic polymer composites. *International communications in heat and mass transfer*, 25(5):723–732, 1998.

[71] D. Hasselman, K. Donaldson, and J. Thomas Jr. Effective thermal conductivity of uniaxial composite with cylindrically orthotropic carbon fibers and interfacial thermal barrier. *Journal of composite materials*, 27 (6):637–644, 1993.

[72] J. A. Charles and D. W. Wilson. A model of passive thermal nondestructive evaluation of composite laminates. *Polymer Composites*, 2(3):105–111, 1981.

[73] M. Villière, D. Lecointe, V. Sobotka, N. Boyard, and D. Delaunay. Experimental determination and modeling of thermal conductivity tensor of carbon/epoxy composite. *Composites Part A: Applied Science and Manufacturing*, 46:60–68, 2013.

[74] M. Kulkarni and R. Brady. A model of global thermal conductivity in laminated carbon/carbon composites. *Composites science and Technology*, 57(3):277–285, 1997.

[75] A. C. Ugural. *Stresses in plates and shells*. McGraw-Hill, 1999.

[76] R. Szilard. *Theory and analysis of plates: Classical and numerical methods*. 1974.

[77] S. Lee, A. Hutputanasin, A. Toorian, W. Lan, R. Munakata, J. Carnahan, D. Pignatelli, and A. Mehrparvar. Cubesat design specification, rev. 13: The cubesat program. *San Luis Obispo, California Polytechnic State University*, 2014.

[78] ISO 9044 industrial woven wire cloth: Technical requirements and testing. *International Organization for Standardization*, 1999.

[79] C. Li and G. Peterson. The effective thermal conductivity of wire screen. *International Journal of Heat and Mass Transfer*, 49(21-22):4095–4105, oct 2006. doi: 10.1016/j.ijheatmasstransfer.2006.03.031.

[80] J. Xu and R. A. Wirtz. In-plane effective thermal conductivity of plain-weave screen laminates. *IEEE Transactions on components and packaging technologies*, 25(4):615–620, 2002.

[81] J. Koh and A. Fortini. Prediction of thermal conductivity and electrical resistivity of porous metallic materials. *International Journal of Heat and Mass Transfer*, 16(11):2013–2022, 1973.

[82] F. Moleiro, C. M. Soares, and E. Carrera. Three-dimensional exact hygro-thermo-elastic solutions for multilayered plates: Composite laminates, fibre metal laminates and sandwich plates. *Composite Structures*, 216:260–278, may 2019. doi: 10.1016/j.compstruct.2019.02.071.

[83] H. A. Rasheed. *Strengthening design of reinforced concrete with FRP*. CRC Press, 2014.

[84] Aluminium 6061 T6. MatWeb - Material Property Data, 2019. URL http://www.matweb.com/search/DataSheet.aspx?MatGUID=b8d536e0b9b54bd7b69e4124d8f1d20a&ckck=1. Accessed on 15/06/2019.

[85] Standard price list for all meshes. Goodfellow Corporation. Accessed on 15/06/2019.

[86] PGS graphite sheets. Technical report, Panasonic, 2017.

[87] G. Neuer, G. Busso, and G. Carlomagno. Emissivity measurements on graphite and composite materials in the visible and infrared spectral range. In *1st Conference on Quantitative InfraRed Thermography (QIRT 1992), Seminar*, volume 27, pages 359–364, 1992.

[88] M. Redmond and A. Mastropietro. Thermophysical and optical properties of materials considered for use on the ldsd test vehicle. 45th International Conference on Environmental Systems, 2015.

[89] T. L. Bergman, F. P. Incropera, A. S. Lavine, and D. P. DeWitt. *Introduction to heat transfer*. John Wiley & Sons, 2011.

[90] C. Freitag, R. Weber, and T. Graf. Polarization dependence of laser interaction with carbon fibers and cfrp. *Optics express*, 22(2):1474–1479, 2014.

[91] E. R. Johnston, F. Beer, and E. Eisenberg. *Vector Mechanics for Engineers: Statics and Dynamics*. McGraw-Hill, 2009.

[92] C. Tofallis. Add or multiply? A tutorial on ranking and choosing with multiple criteria. *INFORMS Transactions on Education*, 14(3):109–119, may 2014. doi: 10.1287/ited.2013.0124.

[93] Space engineering: Space environment. ECSS Secretariat, 2008. Document version ECSS-E-ST-10-04C.

[94] Space engineering: Structural factors of safety for spaceflight hardware. ECSS Secretariat, 2009. Document version ECSS-E-ST-32-10C.

[95] Space engineering: Threaded fasteners handbook. ECSS Secreatariat, 2010. Document version ECSS-E-HB-32-23A.

[96] J. N. Reddy. *An introduction to the finite element method*. American Society of Mechanical Engineers Digital Collection, 1989.

[97] D. V. Hutton and J. Wu. *Fundamentals of finite element analysis*, volume 1. McGraw-hill New York, 2004.

[98] P. S. Heckbert. *Introduction to finite element methods*, volume 42. Springer, 1993.

[99] User manual for small spacecraft mission service proof of concept flight on vega. *Arianespace, ESA, Issue 1 Revision 0*, 2017.

[100] MSC Nastran Linear static analysis user's guide. MSC Software, 2012.

[101] A. O. Cifuentes. *Using MSC/NASTRAN: statics and dynamics*. Springer Science & Business Media, 2012.

[102] N. M. M. Maia. Apontamentos de vibrações e ruído. IST, 1996.

[103] MSC Nastran Dynamic analysis user's guide. MSC Software, 2012.

[104] W. F. Smith and M. E. Rosa. *Princípios de ciência e engenharia de materiais*. 1998.

[105] J. E. Shigley. *Shigley's mechanical engineering design*. Tata McGraw-Hill Education, 2011.

[106] A. F. M. Barros. Apontamentos de mecânica dos sólidos. IST, 2017.

[107] MSC Nastran Quick reference guide. MSC Software, 2012.

[108] A. Mehrparvar, D. Pignatelli, J. Carnahan, R. Munakar, W. Lan, A. Toorian, A. Hurputanasin, and S. Lee. Nanoracks cubesat deployer (NRCSD) interface control document. Technical report, 2015.

[109] Y. Flom. Strength and margins of brazed joints. In *Advances in Brazing*, pages 31–54. Elsevier, 2013. doi: 10.1533/9780857096500.1.31.

[110] Space engineering: Thermal analysis handbook. ECSS Secretariat, 2016. Document version ECSS-E-HB-31-03A.

[111] MSC Nastran Thermal analysis user's guide. MSC Software, 2012.

[112] J. P. Holman et al. *Heat transfer*, volume 2. McGraw-hill New York, 1986.

[113] Space engineering: Thermal design handbook part 1: View factors. ECSS Secretariat, 2015. Document version ECSS-E-HB-31-01 Part 1A.

[114] T. C. Bannister. Radiation geometry factor between the earth and a satellite. Technical report, National Aeronautics and Space Administration, 1965.

[115] Space engineering: Thermal control general requirements. ECSS Secretariat, 2015. Document version ECSS-E-ST-31C.

[116] J. Graebner. Thermal conductivity of printed wiring boards. *Electronics Cooling*, 1995.

[117] Stainless Steel 334. MatWeb - Material Property Data, 2019. URL http://www.matweb.com/search/DataSheet.aspx?MatGUID=abc4415b0f8b490387e3c922237098da&ckck=1. Accessed on 15/06/2019.

[118] Ferrite. MatWeb - Material Property Data, 2019. URL http://www.matweb.com/search/DataSheet.aspx?MatGUID=e4a772c6c0b04fe3ad826a7e430ad3b5. Accessed on 15/06/2019.

[119] S. Chen, C. Wan, and Y. Wang. Thermal analysis of lithium-ion batteries. *Journal of Power Sources*, 2005.

Appendix A

3U CubeSat Configuration

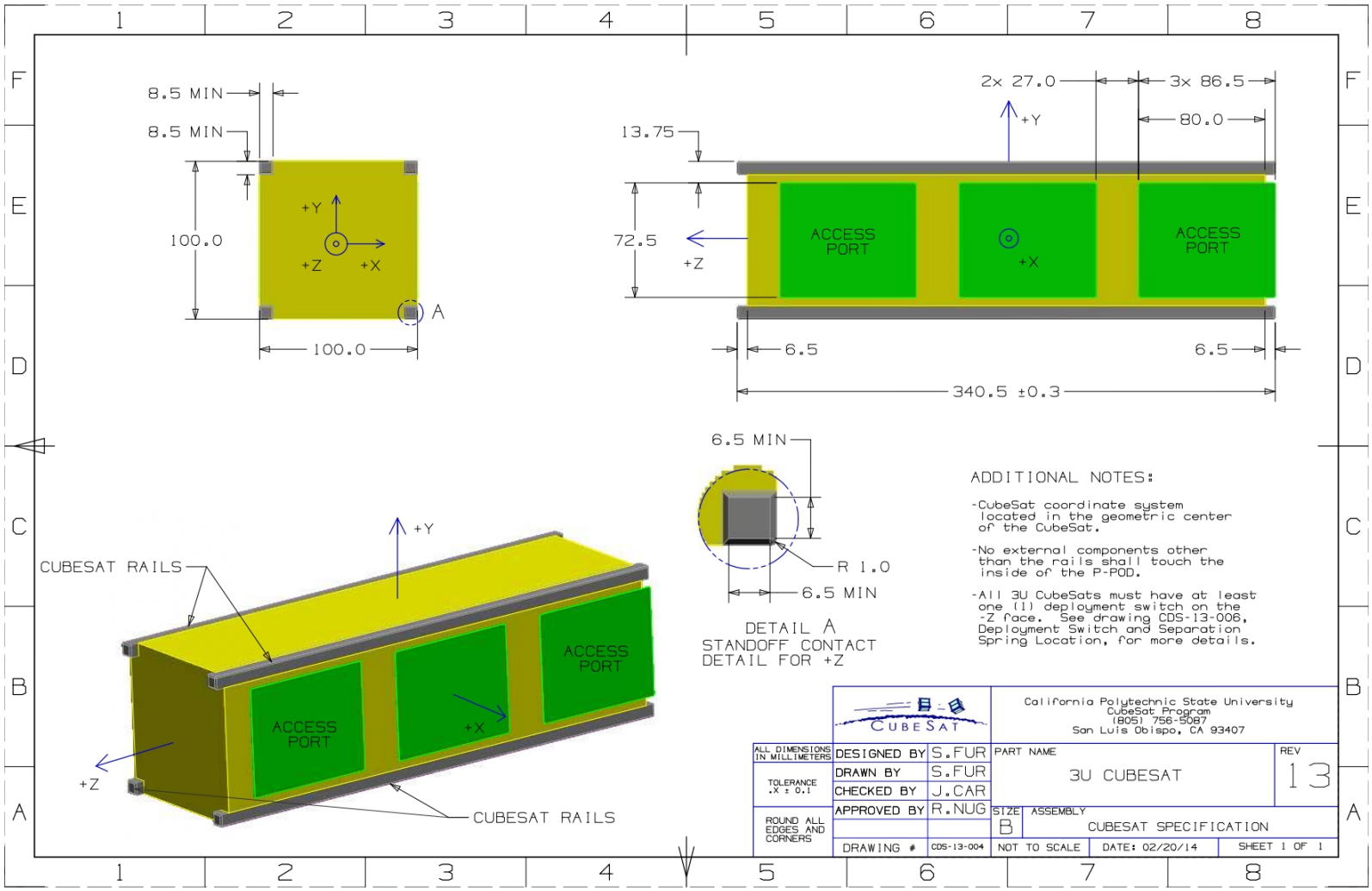

Figure A.1: 3U CubeSat design specification drawing [9].

Appendix B

Materials' Properties

Table B.1: Laminated composite materials' properties.

Laminate n^o	Thickness [mm]	Mass per unit area [kgmm^{-2}]	Structural properties [Nmm^2]			Material strength [Nmm^{-1}]					Thermal properties [mWK^{-1}]		
	t	m_A	$E_{xx}I$	$E_{yy}I$	$G_{xy}J$	X_Tt	X_Ct	Y_Tt	Y_Ct	St	K_{xx}t	K_{yy}t	K_{zz}t
Aluminium design	2	5.40E-06	3.812E+06	3.812E+06	5.667E+06	5.792E+02	5.792E+02	5.792E+02	5.792E+02	4.140E+02	3.340E+02	3.340E+02	3.340E+02
1	2	3.20E-06	8.537E+06	1.552E+06	7.629E+05	1.520E+03	1.380E+03	5.600E+01	3.400E+02	1.400E+02	4.070E+01	4.070E+01	1.400E+00
2	2	3.37E-06	8.257E+06	1.832E+06	7.650E+05	5.792E+02	5.792E+02	5.600E+01	3.400E+02	1.400E+02	6.270E+01	6.270E+01	1.513E+00
3	0.75	1.37E-06	4.072E+05	1.243E+05	4.271E+04	2.172E+02	2.172E+02	2.100E+01	1.275E+02	5.250E+01	3.726E+01	3.726E+01	6.556E-01
4	2	3.55E-06	8.044E+06	2.027E+06	7.614E+05	1.520E+03	1.380E+03	5.600E+01	3.400E+02	1.400E+02	5.266E+01	5.266E+01	1.591E+00
5	0.85	1.71E-06	5.504E+05	2.046E+05	5.758E+04	6.460E+02	5.865E+02	2.380E+01	1.445E+02	5.950E+01	2.926E+01	2.926E+01	8.285E-01
6	2	3.13E-06	8.354E+06	1.734E+06	7.628E+05	4.000E+01	4.000E+01	4.000E+01	4.000E+01	4.000E+01	1.087E+02	1.087E+02	1.473E+00
7	0.7	1.05E-06	3.414E+05	8.994E+04	3.294E+04	1.400E+01	1.400E+01	1.400E+01	1.400E+01	1.400E+01	8.221E+01	8.221E+01	5.708E-01
8	1.05	2.18E-06	7.654E+05	4.949E+05	5.676E+05	3.041E+02	3.041E+02	2.940E+01	1.785E+02	7.350E+01	8.736E+01	8.736E+01	1.282E+00
9	0.9	1.77E-06	4.776E+05	2.991E+05	3.873E+05	2.606E+02	2.606E+02	2.520E+01	1.530E+02	6.300E+01	6.231E+01	6.231E+01	9.430E-01
10	2	3.80E-06	2.419E+06	6.078E+05	5.449E+05	2.040E+03	1.240E+03	8.000E+01	2.800E+02	1.400E+02	1.473E+00	1.473E+00	1.088E+00
11	2	3.92E-06	2.348E+06	6.819E+05	5.471E+05	5.792E+02	5.792E+02	8.000E+01	2.800E+02	1.400E+02	2.641E+01	2.641E+01	1.176E+00
12	0.75	1.55E-06	1.177E+05	4.430E+04	3.120E+04	2.172E+02	2.172E+02	3.000E+01	1.050E+02	5.250E+01	2.549E+01	2.549E+01	5.096E-01
13	2	4.08E-06	2.292E+06	7.310E+05	5.439E+05	2.040E+03	1.240E+03	8.000E+01	2.800E+02	1.400E+02	1.833E+01	1.833E+01	1.238E+00
14	0.85	1.89E-06	1.583E+05	6.850E+04	4.113E+04	8.670E+02	5.270E+02	3.400E+01	1.190E+02	5.950E+01	1.749E+01	1.749E+01	6.463E-01
15	2	3.70E-06	2.372E+06	6.552E+05	5.449E+05	4.000E+01	4.000E+01	4.000E+01	4.000E+01	4.000E+01	7.140E+01	7.140E+01	1.145E+00
16	0.7	1.23E-06	9.738E+04	3.212E+04	2.353E+04	1.400E+01	1.400E+01	1.400E+01	1.400E+01	1.400E+01	7.044E+01	7.044E+01	4.438E-01
17	1.05	2.36E-06	4.698E+05	4.021E+05	5.562E+05	3.041E+02	3.041E+02	4.200E+01	1.470E+02	7.350E+01	7.559E+01	7.559E+01	9.972E-01
18	0.9	1.95E-06	3.102E+05	2.653E+05	3.813E+05	2.606E+02	2.606E+02	3.600E+01	1.260E+02	6.300E+01	5.054E+01	5.054E+01	7.332E-01

Appendix C

FEM Models Supplemental Information

Table C.1: Electronic subsystems and payload centres of gravity and mass moments of inertia.

		Centre of gravity [mm]			Moment of inertia [$10^3 \times$ kgm^2]					
Subsystem	Component	CG_x	CG_y	CG_z	I_{xx}	I_{yy}	I_{zz}	I_{yx}	I_{zx}	I_{zy}
TTC	Antenna	0	0	135.54	8.476E-02	8.555E-02	1.699E-01	-2.315E-02	9.077E-08	2.048E-09
	Transceiver	-1.394	0.586	44.05	5.291E-02	3.760E-02	8.958E-02	-3.230E-03	2.345E-04	-5.167E-04
EPS	Power board - 1	-0.098	4.037	107.31	1.441E-01	1.565E-01	2.825E-01	1.3E-03	1.571E-04	-1.140E-03
	Power board - 2	-0.098	4.037	84.71	1.441E-01	1.565E-01	2.825E-01	1.3E-03	1.571E-04	-1.140E-03
	Power control board	-1.258	0.586	44.05	7.576E-02	6.821E-02	1.422E-01	-6.118E-03	3.943E-04	-1.991E-03
	Solar Panel - 1	-0.313	-55.266	-111.24	3.439E-02	5.853E-02	2.417E-02	2.623E-05	-4.586E-04	8.083E-05
	Solar Panel - 2	-0.313	-55.266	-13.24	3.439E-02	5.853E-02	2.417E-02	2.623E-05	-4.586E-04	8.083E-05
	Solar Panel - 3	-0.313	-55.266	84.76	3.439E-02	5.853E-02	2.417E-02	2.623E-05	-4.586E-04	8.083E-05
	Solar Panel - 4	-55.266	-0.313	-111.24	5.853E-02	3.439E-02	2.417E-02	2.623E-05	-8.083E-05	4.586E-04
	Solar Panel - 5	-55.266	-0.313	-13.24	5.853E-02	3.439E-02	2.417E-02	2.623E-05	-8.083E-05	4.586E-04
	Solar Panel - 6	-55.266	-0.313	84.76	5.853E-02	3.439E-02	2.417E-02	2.623E-05	-8.083E-05	4.586E-04
	Solar Panel - 4	55.266	0.313	-111.24	5.853E-02	3.439E-02	2.417E-02	2.623E-05	8.083E-05	-4.586E-04
	Solar Panel - 5	55.266	0.313	-13.24	5.853E-02	3.439E-02	2.417E-02	2.623E-05	8.083E-05	-4.586E-04
	Solar Panel - 6	55.266	0.313	84.76	5.853E-02	3.439E-02	2.417E-02	2.623E-05	8.083E-05	-4.586E-04
CDH	OBC	2.22	7.942	10.713	5.506E-02	5.036E-02	1.033E-01	6.148E-03	-1.654E-03	-2.331E-03
AOCS	Magnetorquers board	-0.285	-4.015	26.613	1.699E-01	9.601E-02	2.62E-01	-3.472E-04	-1.634E-04	6.549E-03
Payload	NanoCamera	0	0	-111.84	2.909E-01	2.940E-01	1.163E-01	-2.960E-04	-1.299E-03	-2.752E-05

Table C.2: Hot and cold case thermal loads applied to each surface material.

Material		Aluminium 6061 T6 (hard anodized)		CFRP		GFRP		GaAs+Ge		Glass	
Surfaces ID (see figure C.1)	Thermal fluxes [W/m^2]	Hot	Cold	Hot	Cold	Hot	Cold	Hot	Cold	Hot	Cold
1	q_S	197.81	0	1130.32	0	423.87	0	1299.87	0	70.65	0
2	q_A	50.37	0	287.80	0	107.93	0	330.97	0	17.99	0
3		15.31	0	87.50	0	32.81	0	100.62	0	5.47	0
4		15.31	0	87.50	0	32.81	0	100.62	0	5.47	0
5		15.31	0	87.50	0	32.81	0	100.62	0	5.47	0
6		15.31	0	87.50	0	32.81	0	100.62	0	5.47	0
2	q_E	163.97	163.97	136.65	136.65	165.93	165.93	165.93	165.93	175.69	175.69
3		49.85	49.85	41.54	41.54	50.45	50.45	50.45	50.45	53.41	53.41
4		49.85	49.85	41.54	41.54	50.45	50.45	50.45	50.45	53.41	53.41
5		49.85	49.85	41.54	41.54	50.45	50.45	50.45	50.45	53.41	53.41
6		49.85	49.85	41.54	41.54	50.45	50.45	50.45	50.45	53.41	53.41
1	Total Flux	197.81	0	1130.32	0	423.87	0	1299.87	0	70.65	0
2		214.34	163.97	424.45	136.65	273.85	165.93	496.90	165.93	193.67	175.69
3		65.16	49.85	129.04	41.54	83.26	50.45	151.07	50.45	58.88	53.41
4		65.16	49.85	129.04	41.54	83.26	50.45	151.07	50.45	58.88	53.41
5		65.16	49.85	129.04	41.54	83.26	50.45	151.07	50.45	58.88	53.41
6		65.16	49.85	129.04	41.54	83.26	50.45	151.07	50.45	58.88	53.41

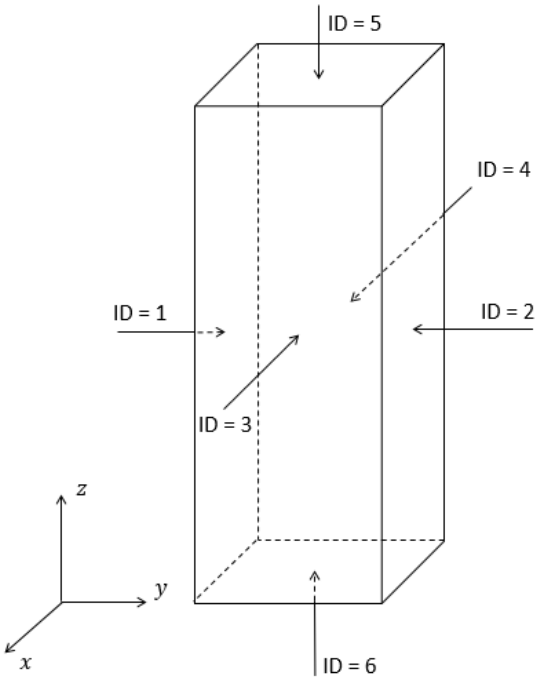

Figure C.1: Surfaces' identification number (ID).

Appendix D

Thermal Finite Element Analysis Results

Table D.1: Operating ranges, minimum and maximum temperatures and temperature variation in each component for the aluminium design.

	Operating range		Hot case				Cold case			
Component	T_{min} [°C]	T_{max} [°C]	T_{min} [°C]	T_{max} [°C]	Status	ΔT [°C]	T_{min} [°C]	T_{max} [°C]	Status	ΔT [°C]
Antenna	-20	60	-5.05	15.35	OK	20.4	-41.55	-21.05	NOT OK	20.5
Power board 1	0	45	16.15	37.25	OK	21.1	2.85	25.45	OK	22.6
Power board 2	0	45	21.75	43.05	OK	21.3	2.55	25.15	OK	22.6
Power control board	-40	85	27.35	48.65	OK	21.3	-17.85	3.55	OK	21.4
Transceiver	-20	60	33.95	64.65	NOT OK	30.7	-27.65	-5.95	NOT OK	21.7
Magnetorquers board	-40	70	30.35	53.65	OK	23.3	-34.65	-13.45	OK	21.2
OBC	-40	85	24.65	46.55	OK	21.9	-39.73	-19.35	OK	20.3
NanoCamera	0	60	-18.25	35.65	NOT OK	53.9	-67.75	-36.05	NOT OK	31.7
Solar panel ID1	-55	150	82.05	118.65	OK	36.6	-79.85	-53.25	NOT OK	26.6
Solar panel ID3	-55	150	-16.15	8.25	OK	24.4	-68.45	-43.75	NOT OK	24.7
Solar panel ID4	-55	150	-16.25	8.05	OK	24.3	-68.55	-43.85	NOT OK	24.7
Rails	-100	100	-6.15	28.25	OK	34.4	-60.75	-31.15	OK	29.6
System support 1	-100	100	9.95	30.45	OK	20.5	-25.35	-4.45	OK	20.9
System support 2	-100	100	17.25	39.05	OK	21.8	-45.55	-24.35	OK	21.2
Payload support	-100	100	6.85	29.75	OK	22.9	-57.05	-35.95	OK	21.1
Side panel ID1	-100	100	28.84	57.05	OK	28.2	-63.15	-38.25	OK	24.9
Side panel ID2	-100	100	-3.71	18.45	OK	22.1	-49.80	-24.55	OK	25.2
Side panel ID3	-100	100	-1.74	20.65	OK	22.3	-58.75	-33.65	OK	25.1
Side panel ID4	-100	100	-2.02	20.45	OK	22.4	-58.74	-33.75	OK	25.0
Side panel ID5	-100	100	-21.55	-1.15	OK	20.4	-62.05	-41.75	OK	20.3
Side panel ID6	-100	100	-10.55	11.45	OK	22.0	-63.65	-42.95	OK	20.7

Table D.2: Operating ranges, minimum and maximum temperatures and temperature variation in each component for the laminate design nº 3.1) ($\alpha = 0.14$).

	Operating range		Hot case				Cold case			
Component	T_{min} [ºC]	T_{max} [ºC]	T_{min} [ºC]	T_{max} [ºC]	Status	ΔT [ºC]	T_{min} [ºC]	T_{max} [ºC]	Status	ΔT [ºC]
Antenna	-20	60	-6.95	13.55	OK	20.5	-38.45	-17.85	NOT OK	20.6
Power board 1	0	45	16.45	37.65	OK	21.2	6.75	29.35	OK	22.6
Power board 2	0	45	22.55	43.95	OK	21.4	5.85	28.45	OK	22.6
Power control board	-40	85	28.45	49.95	OK	21.5	-14.85	6.65	OK	21.5
Transceiver	-20	60	35.35	66.15	NOT OK	30.8	-24.95	-3.25	NOT OK	21.7
Magnetorquers board	-40	70	31.95	55.45	OK	23.5	-32.25	-11.05	OK	21.2
OBC	-40	85	26.35	48.45	OK	22.1	-38.35	-17.25	OK	21.1
NanoCamera	0	60	-21.55	34.05	NOT OK	55.6	-70.05	-37.75	NOT OK	32.3
Solar panel ID1	-55	150	83.25	122.95	OK	39.7	-84.35	-51.75	NOT OK	32.6
Solar panel ID3	-55	150	-18.35	7.65	OK	26.0	-70.95	-41.55	NOT OK	29.4
Solar panel ID4	-55	150	-18.55	7.45	OK	26.0	-71.15	-41.65	NOT OK	29.5
Rails	-100	100	-7.85	24.95	OK	32.8	-62.25	-28.35	OK	33.9
System support 1	-100	100	9.75	30.35	OK	20.6	-19.85	0.95	OK	20.8
System support 2	-100	100	19.05	40.95	OK	21.9	-43.75	-22.55	OK	21.2
Payload support	-100	100	5.95	28.65	OK	22.7	-59.25	-38.15	OK	21.1
Side panel ID1	-100	100	15.32	73.65	OK	58.3	-69.15	-26.75	OK	42.4
Side panel ID2	-100	100	-10.07	22.35	OK	32.4	-55.55	-15.35	OK	40.2
Side panel ID3	-100	100	-8.32	24.85	OK	33.1	-63.95	-22.95	OK	41.0
Side panel ID4	-100	100	-8.57	24.45	OK	33.0	-64.15	-23.05	OK	41.1
Side panel ID5	-100	100	-26.55	-3.75	OK	22.8	-62.25	-39.85	OK	22.4
Side panel ID6	-100	100	-18.75	10.85	OK	29.6	-69.05	-44.85	OK	24.2

Table D.3: Operating ranges, minimum and maximum temperatures and temperature variation in each component for the laminate design nº 7.1) ($\alpha = 0.14$).

	Operating range		Hot case				Cold case			
Component	T_{min} [ºC]	T_{max} [ºC]	T_{min} [ºC]	T_{max} [ºC]	Status	ΔT [ºC]	T_{min} [ºC]	T_{max} [ºC]	Status	ΔT [ºC]
Antenna	-20	60	-5.85	14.65	OK	20.5	-39.95	-19.35	NOT OK	20.6
Power board 1	0	45	16.45	37.65	OK	21.2	4.75	27.45	OK	22.7
Power board 2	0	45	22.25	43.65	OK	21.4	4.15	26.85	OK	22.7
Power control board	-40	85	28.05	49.45	OK	21.4	-16.45	5.05	OK	21.5
Transceiver	-20	60	34.75	65.55	NOT OK	30.8	-26.35	-4.65	NOT OK	21.7
Magnetorquers board	-40	70	31.25	54.65	OK	23.4	-33.55	-12.35	OK	21.2
OBC	-40	85	25.55	47.65	OK	22.1	-39.45	-18.45	OK	21.0
NanoCamera	0	60	-19.95	34.85	NOT OK	54.8	-69.25	-37.25	NOT OK	32.0
Solar panel ID1	-55	150	81.95	120.85	OK	38.9	-82.25	-52.05	NOT OK	30.2
Solar panel ID3	-55	150	-17.15	8.15	OK	25.3	-69.85	-42.25	NOT OK	27.6
Solar panel ID4	-55	150	-17.35	8.05	OK	25.4	-70.05	-42.35	NOT OK	27.7
Rails	-100	100	-6.95	26.45	OK	33.4	-61.75	-29.65	OK	32.1
System support 1	-100	100	10.05	30.55	OK	20.5	-22.55	-1.75	OK	20.8
System support 2	-100	100	18.25	40.05	OK	21.8	-44.85	-23.65	OK	21.2
Payload support	-100	100	6.35	29.25	OK	22.9	-58.45	-37.35	OK	21.1
Side panel ID1	-100	100	21.76	65.55	OK	43.7	-66.45	-32.75	OK	33.7
Side panel ID2	-100	100	-6.74	20.15	OK	26.9	-53.26	-19.85	OK	33.4
Side panel ID3	-100	100	-5.11	22.35	OK	27.4	-61.75	-28.45	OK	33.3
Side panel ID4	-100	100	-5.37	21.95	OK	27.3	-61.95	-28.55	OK	33.4
Side panel ID5	-100	100	-23.75	-2.25	OK	21.5	-61.85	-40.65	OK	21.2
Side panel ID6	-100	100	-14.75	11.25	OK	26.0	-66.75	-44.35	OK	22.4

Table D.4: Operating ranges, minimum and maximum temperatures and temperature variation in each component for the laminate design nº 16.1) ($\alpha = 0.14$).

	Operating range		Hot case				Cold case			
Component	T_{min} [ºC]	T_{max} [ºC]	T_{min} [ºC]	T_{max} [ºC]	Status	ΔT [ºC]	T_{min} [ºC]	T_{max} [ºC]	Status	ΔT [ºC]
Antenna	-20	60	-6.05	14.45	OK	20.5	-39.65	-19.15	NOT OK	20.5
Power board 1	0	45	16.45	37.65	OK	21.2	5.15	27.75	OK	22.6
Power board 2	0	45	22.35	43.75	OK	21.4	4.45	27.05	OK	22.6
Power control board	-40	85	28.15	49.55	OK	21.4	-16.15	5.35	OK	21.5
Transceiver	-20	60	34.85	65.65	NOT OK	30.8	-26.15	-4.35	NOT OK	21.8
Magnetorquers board	-40	70	31.35	54.75	OK	23.4	-33.35	-12.15	OK	21.2
OBC	-40	85	25.65	47.75	OK	22.1	-39.35	-18.25	OK	21.1
NanoCamera	0	60	-20.25	34.65	NOT OK	54.9	-69.45	-37.35	NOT OK	32.1
Solar panel ID1	-55	150	82.05	121.15	OK	39.1	-82.65	-51.95	NOT OK	30.7
Solar panel ID3	-55	150	-17.35	8.05	OK	25.4	-70.05	-42.15	NOT OK	27.9
Solar panel ID4	-55	150	-17.55	7.95	OK	25.5	-70.25	-42.15	NOT OK	28.1
Rails	-100	100	-7.05	26.15	OK	33.2	-61.85	-29.35	OK	32.5
System support 1	-100	100	10.05	30.55	OK	20.5	-22.15	-1.35	OK	20.8
System support 2	-100	100	18.35	40.25	OK	21.9	-44.65	-23.45	OK	21.2
Payload support	-100	100	6.35	29.15	OK	22.8	-58.65	-37.55	OK	21.1
Side panel ID1	-100	100	20.65	66.85	OK	46.2	-66.95	-31.85	OK	35.1
Side panel ID2	-100	100	-7.32	20.45	OK	27.7	-53.75	-19.05	OK	34.7
Side panel ID3	-100	100	-5.66	22.75	OK	28.4	-62.25	-27.55	OK	34.7
Side panel ID4	-100	100	-5.92	22.35	OK	28.2	-62.35	-27.65	OK	34.7
Side panel ID5	-100	100	-24.15	-2.45	OK	21.7	-61.95	-40.55	OK	21.4
Side panel ID6	-100	100	-15.45	11.25	OK	26.7	-67.15	-44.45	OK	22.7

Table D.5: Operating ranges, minimum and maximum temperatures and temperature variation in each component for the laminate design nº 3.1) ($\alpha = 0.8$).

	Operating range		Hot case				Cold case			
Component	T_{min} [ºC]	T_{max} [ºC]	T_{min} [ºC]	T_{max} [ºC]	Status	ΔT [ºC]	T_{min} [ºC]	T_{max} [ºC]	Status	ΔT [ºC]
Antenna	-20	60	19.85	40.35	OK	20.5	-36.65	-16.15	NOT OK	20.5
Power board 1	0	45	37.45	58.35	NOT OK	20.9	8.15	30.75	OK	22.6
Power board 2	0	45	42.75	63.75	NOT OK	21.0	7.35	30.05	OK	22.7
Power control board	-40	85	48.15	69.05	OK	20.9	-13.15	8.15	OK	21.3
Transceiver	-20	60	54.35	84.15	NOT OK	29.8	-23.45	-1.75	NOT OK	21.7
Magnetorquers board	-40	70	50.95	73.95	NOT OK	23.0	-30.95	-9.75	OK	21.2
OBC	-40	85	45.55	67.15	OK	21.6	-37.25	-16.15	OK	21.1
NanoCamera	0	60	1.45	53.25	OK	51.8	-70.35	-37.05	NOT OK	33.3
Solar panel ID1	-55	150	89.55	126.25	OK	36.7	-83.45	-51.65	NOT OK	31.8
Solar panel ID3	-55	150	-8.75	19.25	OK	28.0	-70.25	-41.35	NOT OK	28.9
Solar panel ID4	-55	150	-8.95	19.15	OK	28.1	-70.45	-41.45	NOT OK	29.0
Rails	-100	100	16.95	46.35	OK	29.4	-61.25	-27.65	OK	33.6
System support 1	-100	100	31.75	52.15	OK	20.4	-18.85	1.95	OK	20.8
System support 2	-100	100	38.55	59.95	OK	21.4	-42.95	-21.75	OK	21.2
Payload support	-100	100	27.85	49.15	OK	21.3	-58.45	-37.35	OK	21.1
Side panel ID1	-100	100	34.80	84.85	OK	50.0	-67.85	-28.35	OK	39.5
Side panel ID2	-100	100	24.11	60.05	OK	35.9	-54.15	-15.85	OK	38.3
Side panel ID3	-100	100	11.05	41.85	OK	30.8	-62.65	-24.05	OK	38.6
Side panel ID4	-100	100	10.75	41.65	OK	30.9	-62.75	-24.15	OK	38.6
Side panel ID5	-100	100	6.55	31.65	OK	25.1	-59.85	-38.05	OK	21.8
Side panel ID6	-100	100	8.05	33.45	OK	25.4	-67.15	-43.45	OK	23.7

Table D.6: Operating ranges, minimum and maximum temperatures and temperature variation in each component for the laminate design nº 7.1) ($\alpha = 0.8$).

	Operating range		Hot case				Cold case			
Component	T_{min} [ºC]	T_{max} [ºC]	T_{min} [ºC]	T_{max} [ºC]	Status	ΔT [ºC]	T_{min} [ºC]	T_{max} [ºC]	Status	ΔT [ºC]
Antenna	-20	60	20.45	40.85	OK	20.4	-37.95	-17.45	NOT OK	20.5
Power board 1	0	45	37.25	58.15	NOT OK	20.9	6.55	29.15	OK	22.6
Power board 2	0	45	42.45	63.45	NOT OK	21.0	6.05	28.65	OK	22.6
Power control board	-40	85	47.65	68.55	OK	20.9	-14.45	6.95	OK	21.4
Transceiver	-20	60	53.85	83.55	NOT OK	29.7	-24.55	-2.85	NOT OK	21.7
Magnetorquers board	-40	70	50.35	73.35	NOT OK	23.0	-31.95	-10.75	OK	21.2
OBC	-40	85	44.95	66.45	OK	21.5	-38.15	-17.05	OK	21.1
NanoCamera	0	60	2.55	53.85	OK	51.3	-69.65	-36.55	NOT OK	33.1
Solar panel ID1	-55	150	88.95	124.75	OK	35.8	-81.65	-51.95	NOT OK	29.7
Solar panel ID3	-55	150	-7.55	19.85	OK	27.4	-69.35	-42.05	NOT OK	27.3
Solar panel ID4	-55	150	-7.65	19.75	OK	27.4	-69.45	-42.15	NOT OK	27.3
Rails	-100	100	18.15	46.95	OK	28.8	-60.85	-28.85	OK	32.0
System support 1	-100	100	31.75	52.15	OK	20.4	-21.25	-0.35	OK	20.9
System support 2	-100	100	37.85	59.25	OK	21.4	-43.75	-22.55	OK	21.2
Payload support	-100	100	28.05	49.55	OK	21.5	-57.75	-36.65	OK	21.1
Side panel ID1	-100	100	39.61	78.85	OK	39.2	-65.55	-33.25	OK	32.3
Side panel ID2	-100	100	27.13	57.55	OK	30.4	-52.35	-19.85	OK	32.5
Side panel ID3	-100	100	13.75	40.55	OK	26.8	-60.75	-28.65	OK	32.1
Side panel ID4	-100	100	13.55	40.35	OK	26.8	-60.85	-28.75	OK	32.1
Side panel ID5	-100	100	8.15	30.85	OK	22.7	-59.75	-38.85	OK	20.9
Side panel ID6	-100	100	10.65	34.05	OK	23.4	-65.15	-42.95	OK	22.2

Table D.7: Operating ranges, minimum and maximum temperatures and temperature variation in each component for the laminate design nº 16.1) ($\alpha = 0.3$).

	Operating range		Hot case				Cold case			
Component	T_{min} [ºC]	T_{max} [ºC]	T_{min} [ºC]	T_{max} [ºC]	Status	ΔT [ºC]	T_{min} [ºC]	T_{max} [ºC]	Status	ΔT [ºC]
Antenna	-20	60	-0.85	19.65	OK	20.5	-39.85	-19.25	NOT OK	20.6
Power board 1	0	45	20.75	41.85	OK	21.1	4.95	27.55	OK	22.6
Power board 2	0	45	26.35	47.65	NOT OK	21.3	4.25	26.95	OK	22.7
Power control board	-40	85	32.05	53.35	OK	21.3	-16.35	5.15	OK	21.5
Transceiver	-20	60	38.65	69.15	NOT OK	30.5	-26.25	-4.55	NOT OK	21.7
Magnetorquers board	-40	70	35.15	58.45	OK	23.3	-33.45	-12.25	OK	21.2
OBC	-40	85	29.55	51.55	OK	22.0	-39.45	-18.35	OK	21.1
NanoCamera	0	60	-14.65	38.65	NOT OK	53.3	-69.75	-37.45	NOT OK	32.3
Solar panel ID1	-55	150	83.35	121.85	OK	38.5	-82.65	-51.95	NOT OK	30.7
Solar panel ID3	-55	150	-15.25	10.75	OK	26.0	-70.15	-42.15	NOT OK	28.0
Solar panel ID4	-55	150	-15.45	10.55	OK	26.0	-70.25	-42.25	NOT OK	28.0
Rails	-100	100	-1.75	29.95	OK	31.7	-61.95	-29.45	OK	32.5
System support 1	-100	100	14.45	34.95	OK	20.5	-22.25	-1.45	OK	20.8
System support 2	-100	100	22.45	44.15	OK	21.7	-44.75	-23.55	OK	21.2
Payload support	-100	100	10.95	33.35	OK	22.4	-58.65	-37.55	OK	21.1
Side panel ID1	-100	100	23.89	69.25	OK	45.3	-66.95	-31.95	OK	35.0
Side panel ID2	-100	100	-0.16	28.45	OK	28.6	-53.75	-19.15	OK	34.6
Side panel ID3	-100	100	-1.66	26.55	OK	28.2	-62.25	-27.65	OK	34.6
Side panel ID4	-100	100	-1.93	26.15	OK	28.1	-62.35	-27.75	OK	34.6
Side panel ID5	-100	100	-17.75	4.35	OK	22.1	-62.05	-40.65	OK	21.4
Side panel ID6	-100	100	-10.45	15.55	OK	26.0	-67.25	-44.55	OK	22.7

Table D.8: Operating ranges, minimum and maximum temperatures and temperature variation in each component for the laminate design nº 7.3) ($\alpha = 0.8$).

	Operating range		Hot case				Cold case			
Component	T_{min} [ºC]	T_{max} [ºC]	T_{min} [ºC]	T_{max} [ºC]	Status	ΔT [ºC]	T_{min} [ºC]	T_{max} [ºC]	Status	ΔT [ºC]
Antenna	-20	60	20.65	41.05	OK	20.4	-39.35	-18.85	NOT OK	20.5
Power board 1	0	45	36.85	57.75	NOT OK	20.9	4.95	27.55	OK	22.6
Power board 2	0	45	41.85	62.85	NOT OK	21.0	4.75	27.45	OK	22.7
Power control board	-40	85	47.05	67.95	OK	20.9	-15.65	5.75	OK	21.4
Transceiver	-20	60	53.15	82.85	NOT OK	29.7	-25.55	-3.95	NOT OK	21.6
Magnetorquers board	-40	70	49.65	72.55	NOT OK	22.9	-32.75	-11.65	OK	21.1
OBC	-40	85	44.25	65.65	OK	21.4	-38.85	-17.85	OK	21.0
NanoCamera	0	60	3.65	54.45	OK	50.8	-68.45	-35.65	NOT OK	32.8
Solar panel ID1	-55	150	89.25	123.25	OK	34.0	-79.65	-52.95	NOT OK	26.7
Solar panel ID3	-55	150	-6.45	20.05	OK	26.5	-68.15	-43.35	NOT OK	24.8
Solar panel ID4	-55	150	-6.55	19.85	OK	26.4	-68.25	-43.35	NOT OK	24.9
Rails	-100	100	19.05	47.35	OK	28.3	-60.05	-30.15	OK	29.9
System support 1	-100	100	31.45	51.85	OK	20.4	-23.55	-2.65	OK	20.9
System support 2	-100	100	37.15	58.55	OK	21.4	-44.35	-23.15	OK	21.2
Payload support	-100	100	28.45	49.95	OK	21.5	-56.55	-35.45	OK	21.1
Side panel ID1	-100	100	44.84	72.85	OK	28.0	-62.85	-37.75	OK	25.1
Side panel ID2	-100	100	30.41	54.85	OK	24.4	-49.35	-23.85	OK	25.5
Side panel ID3	-100	100	16.38	39.15	OK	22.7	-58.15	-32.95	OK	25.2
Side panel ID4	-100	100	16.09	38.85	OK	22.7	-58.35	-33.05	OK	25.3
Side panel ID5	-100	100	9.45	30.35	OK	20.9	-60.05	-39.75	OK	20.3
Side panel ID6	-100	100	13.35	34.65	OK	21.3	-62.65	-41.85	OK	20.8

Table D.9: Operating ranges, minimum and maximum temperatures and temperature variation in each component for the laminate design nº 16.3) ($\alpha = 0.3$).

	Operating range		Hot case				Cold case			
Component	T_{min} [ºC]	T_{max} [ºC]	T_{min} [ºC]	T_{max} [ºC]	Status	ΔT [ºC]	T_{min} [ºC]	T_{max} [ºC]	Status	ΔT [ºC]
Antenna	-20	60	-0.05	20.35	OK	20.4	-41.75	-21.25	NOT OK	20.5
Power board 1	0	45	20.25	41.35	OK	21.1	2.65	25.25	OK	22.6
Power board 2	0	45	25.65	46.95	NOT OK	21.3	2.35	25.05	OK	22.7
Power control board	-40	85	31.15	52.35	OK	21.2	-18.05	3.45	OK	21.5
Transceiver	-20	60	37.65	68.15	NOT OK	30.5	-27.75	-6.05	NOT OK	21.7
Magnetorquers board	-40	70	34.15	57.35	OK	23.2	-34.75	-13.55	OK	21.2
OBC	-40	85	28.45	50.25	OK	21.8	-39.55	-19.45	OK	20.1
NanoCamera	0	60	-12.75	39.55	NOT OK	52.3	-68.05	-36.05	NOT OK	32.0
Solar panel ID1	-55	150	83.35	119.45	OK	36.1	-79.85	-53.25	NOT OK	26.6
Solar panel ID3	-55	150	-13.95	10.85	OK	24.8	-68.45	-43.85	NOT OK	24.6
Solar panel ID4	-55	150	-14.15	10.65	OK	24.8	-68.55	-43.95	NOT OK	24.6
Rails	-100	100	-0.85	31.85	OK	32.7	-60.75	-31.25	OK	29.5
System support 1	-100	100	14.25	34.75	OK	20.5	-25.55	-4.65	OK	20.9
System support 2	-100	100	21.25	42.95	OK	21.7	-45.65	-24.45	OK	21.2
Payload support	-100	100	11.45	33.95	OK	22.5	-57.05	-35.95	OK	21.1
Side panel ID1	-100	100	31.97	59.75	OK	27.7	-63.15	-38.35	OK	24.8
Side panel ID2	-100	100	3.76	26.25	OK	22.4	-49.74	-24.75	OK	24.9
Side panel ID3	-100	100	2.25	24.65	OK	22.4	-58.85	-33.85	OK	25
Side panel ID4	-100	100	1.96	24.35	OK	22.3	-58.95	-33.95	OK	25.0
Side panel ID5	-100	100	-15.45	5.05	OK	20.5	-62.15	-41.85	OK	20.3
Side panel ID6	-100	100	-5.75	15.95	OK	21.7	-63.75	-42.95	OK	20.8